FORWARD CHARGE FLOW IN HADRONIC J/PSI PRODUCTION

BY

WEI-GUO LI

M.S., University of Illinois, 1980

THESIS

Submitted in partial fulfillment of the requirements
for the degree of Doctor of Philosophy in Physics
in the Graduate College of the
University of Illinois at Urbana-Champaign, 1985

Urbana, Illinois

FORWARD CHARGE FLOW IN HADRONIC J/PSI PRODUCTION

Wei-guo Li, Ph.D.
Department of Physics
University of Illinois at Urbana-Champaign, 1985

We have examined the properties of the forward charge of J/psi production. The rapidity distribution of the forward charge, the dependence of the forward charge as a function of J/psi Xf and as a function of the effective energy of the forward hadron system are presented. The forward charge of J/psi production is compared with those of omega production and in the inclusive interactions. The forward charge is consistent with the prediction from simple parton fusion model.

ACKNOWLEDGEMENTS

I would like to thank all the people involved in experiments E610 and E673. I have learned a great deal from the people I worked with on these two experiments. Their enthusiasm in high energy physics and their determination for excellence have been the constant inspiration for me. Without them this thesis would not be possible.

First of all, I would like to thank professor Lee Holloway, my advisor. His love for physics, his insight into solving the problems and the constant encouragement he has been giving me have made his guidence essential in my graduate study.

I would like to thank the other professors at the University of Illinois, Robert Sard, Lou Koester, Lorella Jones and Ulrich Kruce for patiently answering my silly questions and giving valuable advice to my research. Their kindness and care for me are unforgettable. I would like to thank George Alverson, Inga Karliner and Selcuk Cihangir for their help and advice.

My fellow graduate students Tom Graff, Pat Lukens and James Bellinger deserve my special thanks for their friendship and the significant contributions each made to this experiment. I am greatly indebted to Howard Budd, Steve Hahn and Paul Schoessow, graduate students involved in E610, who helped me a great deal with programming. All of them have made my life as a graduate student a pleasant one.

I would like to thank the other collaborators on E673 and E610, Tom Kirk, Stephen Pordes, R. Raja, Alan Wehmann, Dan Bauer, John Cooper, Virgil Barnes, Chris Davis, Art Garfinkel, Alvin Laasanen, Jim Simmons, Jeff Wilson, Bill Oliver and Ron Thornton. Each did his share in making the experiment possible and I benefited greatly from their contributions. John Cooper and Dan Bauer, as the organizers, played leading roles in various stages of the experiment.

I would like to thank the supporting group of Fermilab, especially the people in the Neutrino Department and the people who kept the superconducting magnet working smoothly.

I am grateful for the help given by the computer staff at the University of Illinois, Jerry Wray, Dave Lesny and others, I have benefited greatly from their endless effort to make the computing easy and reliable. Jim Kohlmeier helped me a lot in understanding the chamber readout system. I thank the secretaries of the high energy group, Dorothy Schoeps, Wynemia Woods and Jeannine Adomaitis for providing office help and for arranging trips to Fermilab.

This research was funded in part by the U.S. Department of Energy Contract No. DE-AC02-76ER01195.

TABLE OF CONTENTS

CHAPTER 1 INTRODUCTION

The data used for this thesis were obtained during experiment E673 at Fermilab, which ran from January to April in 1982 in the Muon Lab. The E673 collaborator consisted of about thirty physicists from University of Illinois, Fermilab, University of Pennsylvania, Purdue University and Tufts University. The spokesman was Dr. John W. Cooper.

The main purpose of the experiment was to study the charmonium production mechanism in hadronic interaction through the detection of the chi states. Beams of 185 GeV/c π^-, 200 GeV/c or 250 GeV/c protons were used to hit a beryllium target. The trigger selected high mass dimuon pairs, a J/psi signal was extracted from the collected data. Charged particles and photons were detected along with the muon pairs. We have reconstructed the chi states by combining the J/psi with the photons in the same event. The physics related with the chi states is already published[ref. 1].

This thesis deals with the charged particles associated with the J/psi events, the differences of the forward-going charge flow in the J/psi events from these in the inclusive interactions and Drell-Yan process are compared with different production models in the hope that we can understand more about charmonium production in the framework of QCD.

CHAPTER 2 THEORETICAL AND EXPERIMENTAL BACKGROUND

The discovery of the J/psi particle in 1974 opened a new era in high energy physics. Since then, a lot of exciting new discoveries have been made, the discoveries of the bottom(b) and top(t) quarks, the finding of the w and z particles, to name a few. But the J/psi particle and the other $c\bar{c}$ bound states are still very valuable subjects to study. We call these $c\bar{c}$ bound states charmonium states.

One of the interpretations of the J/psi particle upon its discovery was that it was a bound state of the charmed quark(c) and the charmed antiquark($\bar{c}$). The charm quark was proposed in some theoretical models but had not been observed before. The heavy mass and the narrow decay width made it a very interesting and special subject to study. Since then, extensive work has been done on finding out the spectrum of the charmonium states and their properties, mostly on electron-positron machines. Subsequent discoveries confirmed the charm quark interpretation and uncovered the rich spectrum of the charmonium states shown in Figure 2.1. Because the charm quark is much heavier than the previously known quarks, namely up(u), down(d) and strange(s) quarks, the charmonium can be studied by non-relativistic method. Or in the terms of the strong interaction theory QCD, quantum chromodynamics, because the coupling constant of the force between the c and $\bar{c}$ quarks in the charmonium states is small, the charmonium can be treated perturbatively. The calculated masses of the charmonium states and the decay rates are in very good agreement with the experimental

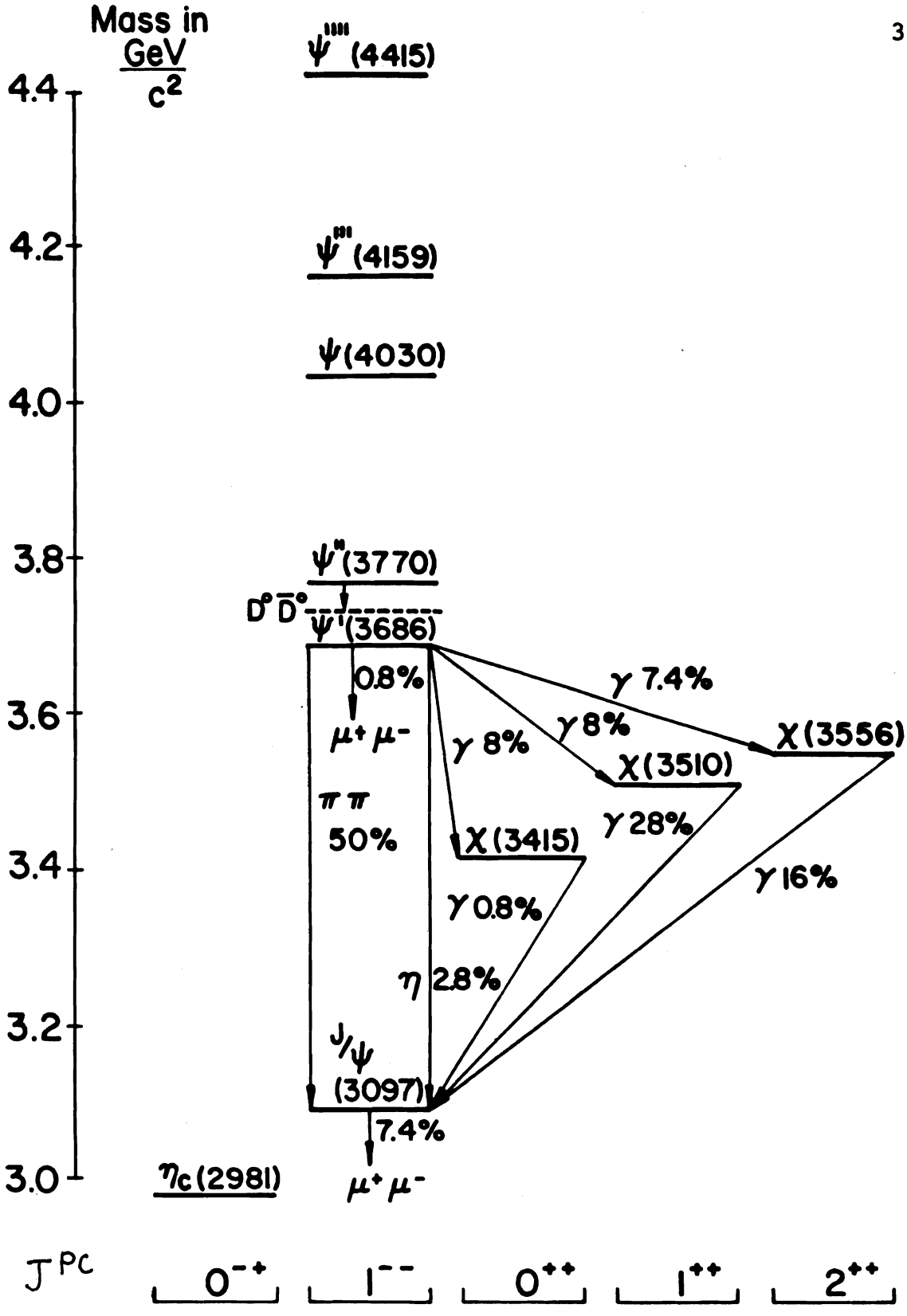

Figure 2.1
Charmonium spectrum

measurements[ref. 2-4].

The production of charmonium states in electron-positron interactions is well understood and the calculated cross-sections of charmonium states are verified by experiments beautifully. The annihilation of electron and positron creates a virtual photon and which then turns into charmonium states with the photon quantum numbers, $J^{PC}=1^{--}$.

The picture of charmonium production in hadronic interactions is not as clear as in electron-positron interactions. Hadrons are composed of quarks and gluons. There are three generations of quarks in nature according to the current knowledge, they are (u,d), (c,s) and (b,t). Their quantum numbers are shown in table 2.1. Each quark has three colours, the colour quantum number only appears in strong interactions. The mediums of the strong force between quarks are gluons, they are spin one and massless particles, because the colour degree of freedom, the gluons can interact with each other. According to QCD, the coupling is weak when the distance between partons in the hadrons is small, the coupling becomes stronger as the distance becomes larger. When the constituents in a hadron become too far apart, the colour flux between them will break and the original hadron will break up into several hadrons. The hadrons only show up in colour singlet states. This phenomena is called colour confinement. We would like to study the hadronic production mechanism of charmonium states in the framework of QCD.

Flavor	I	I_z	S	C	B	T	Q/e
u	1/2	1/2	Ø	Ø	Ø	Ø	2/3
d	1/2	-1/2	Ø	Ø	Ø	Ø	-1/3
c	Ø	Ø	Ø	1	Ø	Ø	2/3
s	Ø	Ø	-1	Ø	Ø	Ø	-1/3
t	Ø	Ø	Ø	Ø	Ø	1	2/3
b	Ø	Ø	Ø	Ø	-1	Ø	-1/3

Table 2-1

Quark quantum numbers

I - total isospin

I_z - z component of isospin

S - strangeness quantum number

C - charm quantum number

B - bottom quantum number

T - top quantum number

Q/e - electric charge

The models proposed so far are all based on the Drell-Yan mechanism[ref. 5]. It states that one quark from one hadron and one antiquark from the other hadron annihilate into a virtual photon, this virtual photon then turns into a lepton pair. This mechanism can explain high mass, non resonance lepton pair production in hadronic interactions quite well. To extend this notion to the charmonium production, the models proposed that one parton from one of the interacting hadrons and one parton from the other hadron would interact to create the charmonium states, the partons could be quarks or gluons. An early model[ref. 6] proposed that J/psi might be produced by intrinsic charm quark fusion. But this model also predicted associate production of charmed particles with the J/psi. The experimental results[ref. 7-9] showed that no more than a few percent of the J/psi were produced in this way, so we will not discuss this mechanism further. Most other models use the light quark fusion or gluon fusion mechanism. The following is the discussion of different models and their predictions of experimentally measurable quantities.

The main theoretical approach to this subject may be separated into two classes of models. One is called "semi-local duality model", or SLDM, another is called "charmonium-based model",or CBM. In SLDM models, the charm anti-charm quark pair is produced by $G+G \rightarrow c+\bar{c}$ and $q+q \rightarrow c+\bar{c}$, the produced $c\bar{c}$ with invariant mass below open charm threshold is postulated to result in one of the charmonium bound states with some fraction F_ψ being J/psi product. According to the lowest diagram, there are three possible ways to create charmonium states,

namely quark fusion (Figure 2.3(b) and 2.3(c)), gluon fusion (Figure 2.2(a) and 2.2(b)) and color evaporation (Figure 2.2(c) and 2.3(a)). We can use the following formulas to calculate the cross-section of the charmonium states.

For quark fusion

$$\frac{d\sigma^{\pi p}_{q\bar{q}}}{dx_f} = \sum_{f=u,d,s} \int_{4m_c^2}^{4m'^2} dQ^2\, \sigma^{q\bar{q}\to c\bar{c}}(Q^2)\cdot\frac{x_\pi x_p}{x_\pi + x_p}\cdot\frac{1}{Q^2}\cdot$$
$$\left[q_\pi(x_\pi,Q^2)\,\bar{q}_p(x_p,Q^2) + \bar{q}_\pi(x_\pi,Q^2)\,q_p(x_p,Q^2)\right]$$

For gluon fusion

$$\frac{d\sigma^{\pi p}_{gg}}{dx_f} = \int_{4m_c^2}^{4m'^2} dQ^2\, \sigma^{gg\to c\bar{c}}(Q^2)\cdot\frac{1}{Q^2}\cdot\frac{x_\pi x_p}{x_\pi + x_p}\, G_\pi(x_\pi,Q^2)\, G_p(x_p,Q^2)$$

Here

1. m_c=1.55 GeV/c, the charm quark mass.
2. m'=1.853 GeV/c, $2m'$ is the open charm production threshold.
3. $x_{\pi,p}=0.5*(\pm x_f+\sqrt{x_f^2+4Q^2/s})$.
4. q_π and q_p are quark structure functions for π^- and p.
5. G_π and G_p are gluon structure functions for π^- and p.
6. $\sigma^{q\bar{q}\to c\bar{c}}(Q^2)$ and $\sigma^{gg\to c\bar{c}}(Q^2)$ can be calculated explicitly.
7. x_f is the Feynman x of a particle, it is the longitudinal momentum of a particle in the CM divided by its maximum possible longitudinal momentum.

The formulas used here do not care about quantum number conservation. As the J/psi has the quantum number $J^{PC}=1^{--}$, it can not be created by the interaction mediated by two gluons as in Figure 2.2(a) and 2.2(b) unless the final $c\bar{c}$ is in coloured state and emits

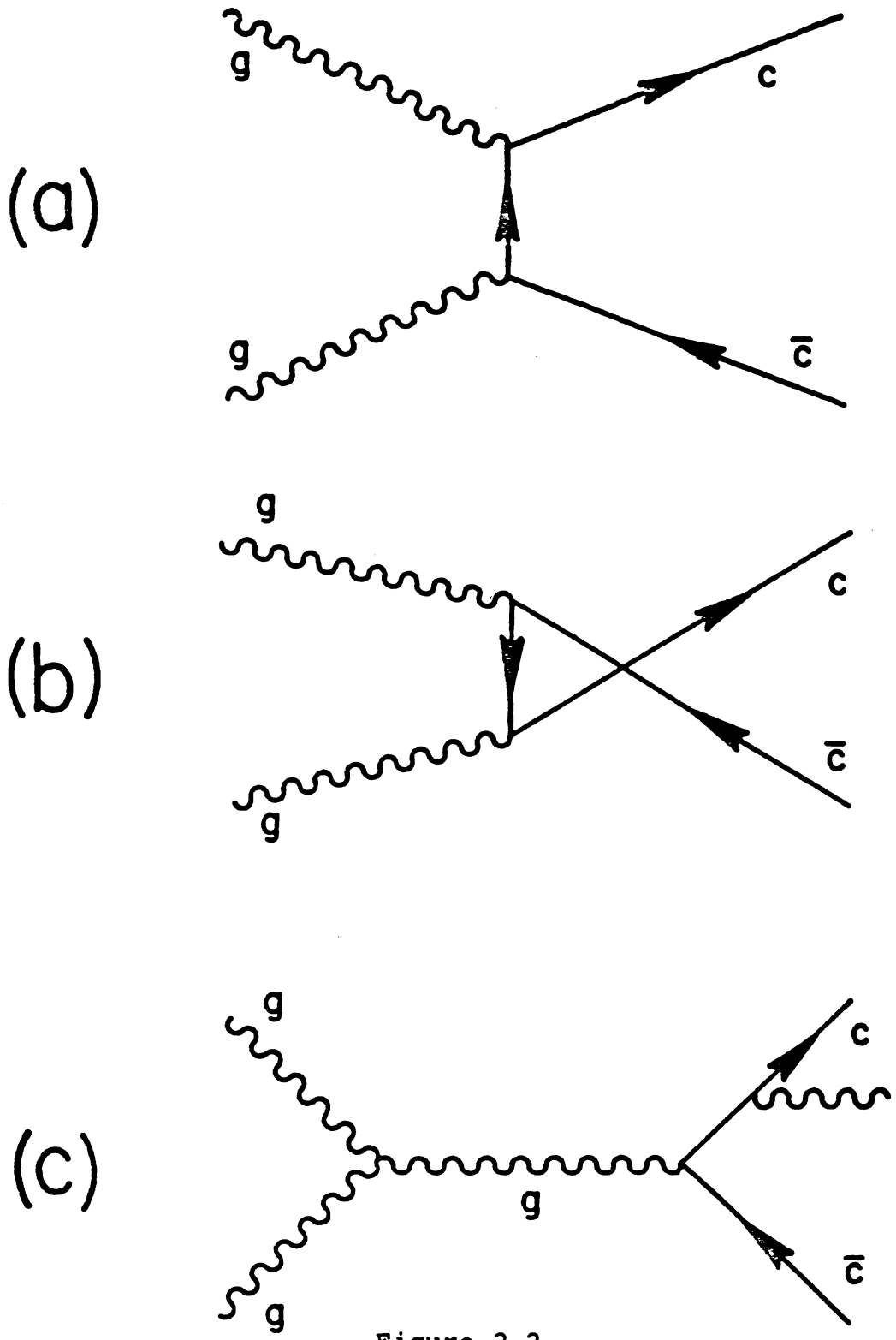

Figure 2-2

Charmonium production by gluons.

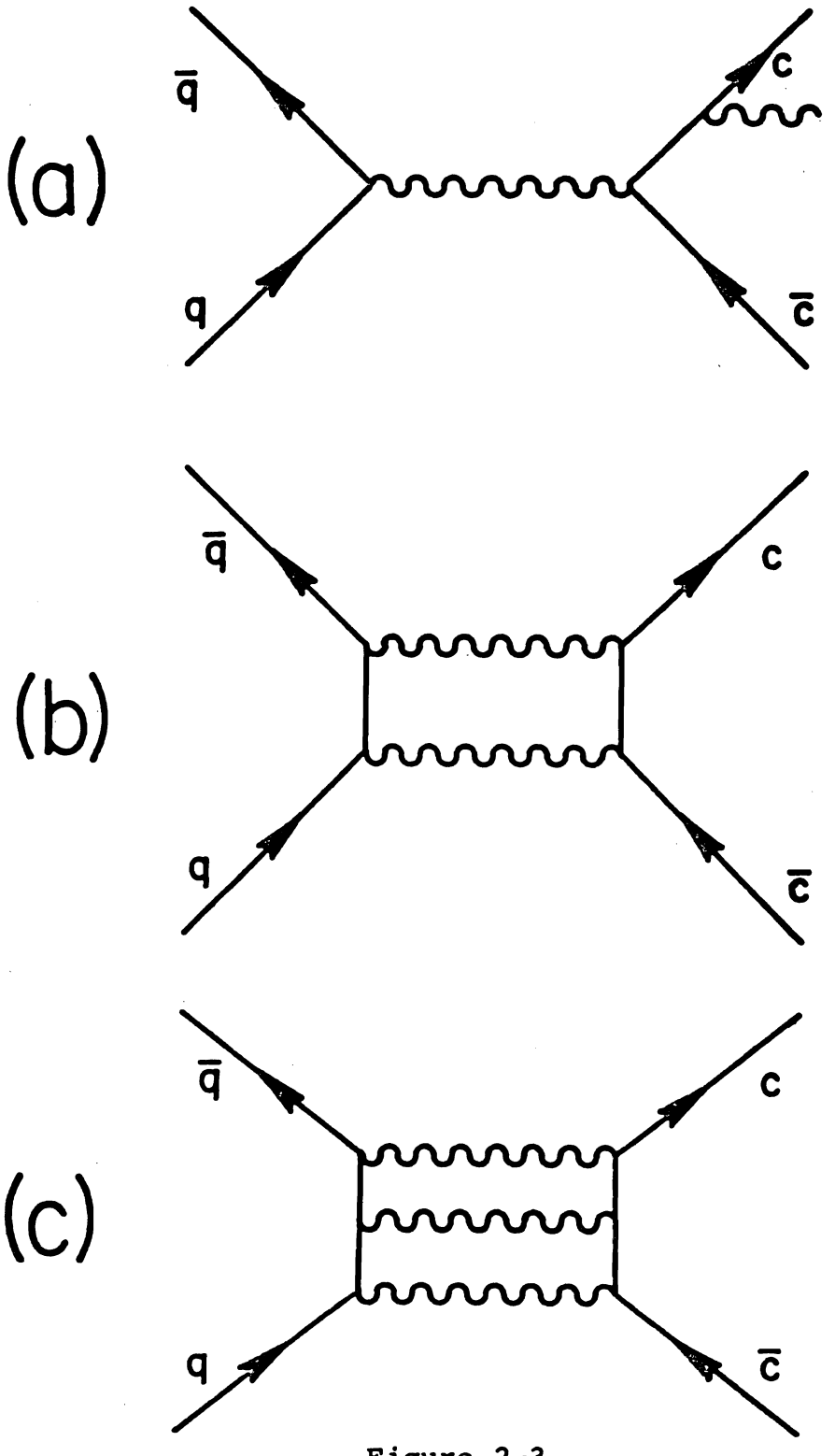

Figure 2-3

Charmonuim production by quarks.

another soft gluon. The allowed two gluons process will produce the P wave charmonium states, their quantum numbers are 0^{++}, 1^{++} and 2^{++}, so a substantial portion of the J/psi would be produced through p wave charmonium states, the χ particles. To calculate the cross-section, the structure functions of the partons in the hadrons must be known. The quark structure functions in the nucleon can be derived from the deep lepton-nucleon inelastic scattering data. The Drell-Yan process is another way to subtract quark structure functions[ref. 10]. The results in these two methods are similar, this fact convinces us that the drell-Yan process is a good way to learn the quark structure function. This method was used to subtract the quark structure functions in pions and other mesons in the meson-nucleon interactions. The obtained quark structure functions in the mesons are consistent with the results from other methods, for example, the inclusive meson productions in meson-nucleon interactions[ref. 11-12]. The gluon structure functions are on a less firm base, there were several attempts to get these functions. Some derived the gluon structure function in photon J/psi production by assuming that the J/psi was produced by the interaction between incident photon and gluons in the nucleon[ref. 13], some fitted the J/psi cross-section as the function of Xf to get the gluon structure functions in the pion and the proton simultaneously[ref. 14], also there was some gluon structure function derived from neutrino deep inelastic data[ref. 15]. All the resulting structure functions are consistent with the structure functions obtained from the simple "counting rules" considerations. Using some

of these structure functions, people[ref. 16-23] have successfully derived the cross-section of J/psi as the function of center of mass (CM) energy and the differential cross-section as the function of Xf. Because the gluon structure function is softer than the quark structure function, quark fusion contribution will become more important as the Xf of the produced J/psi become large, most models predict that around Xf=Ø.6 the quark fusion contribution exceeds the gluon fusion contribution(Figure 2.4). But the absolute cross-sections for J/psi production are not calculated well.

In the CBM models[ref. 24-26] the J/psi is produced explicitly, so the spin parity and colour conservation are taken into account and the cross-sections are fixed in normalization by the J/psi wave function at the origin. The reactions are through the following processes.

$G+G \rightarrow J/\psi G$	at the order of α_s^3
$q+\bar{q} \rightarrow J/\psi GG$	at the order of α_s^4
$q+G \rightarrow J/\psi+q+G$	at the order of α_s^4
$q+q \rightarrow J/\psi+q+q+g$	at the order of α_s^5

Here α_s is the strong coupling constant. The lowest order production amplitudes are related by crossing to the charmonium decay amplitude. The prediction of the cross-section in these models depends on the coupling constant crucially. The author in reference 26 predicted that 23% of the J/psi was produced through G+G and 24% was through q+G in proton nucleon interactions if they chose the coupling constant α_s=Ø.312. If about 40%-50% of the J/psi production from χ and

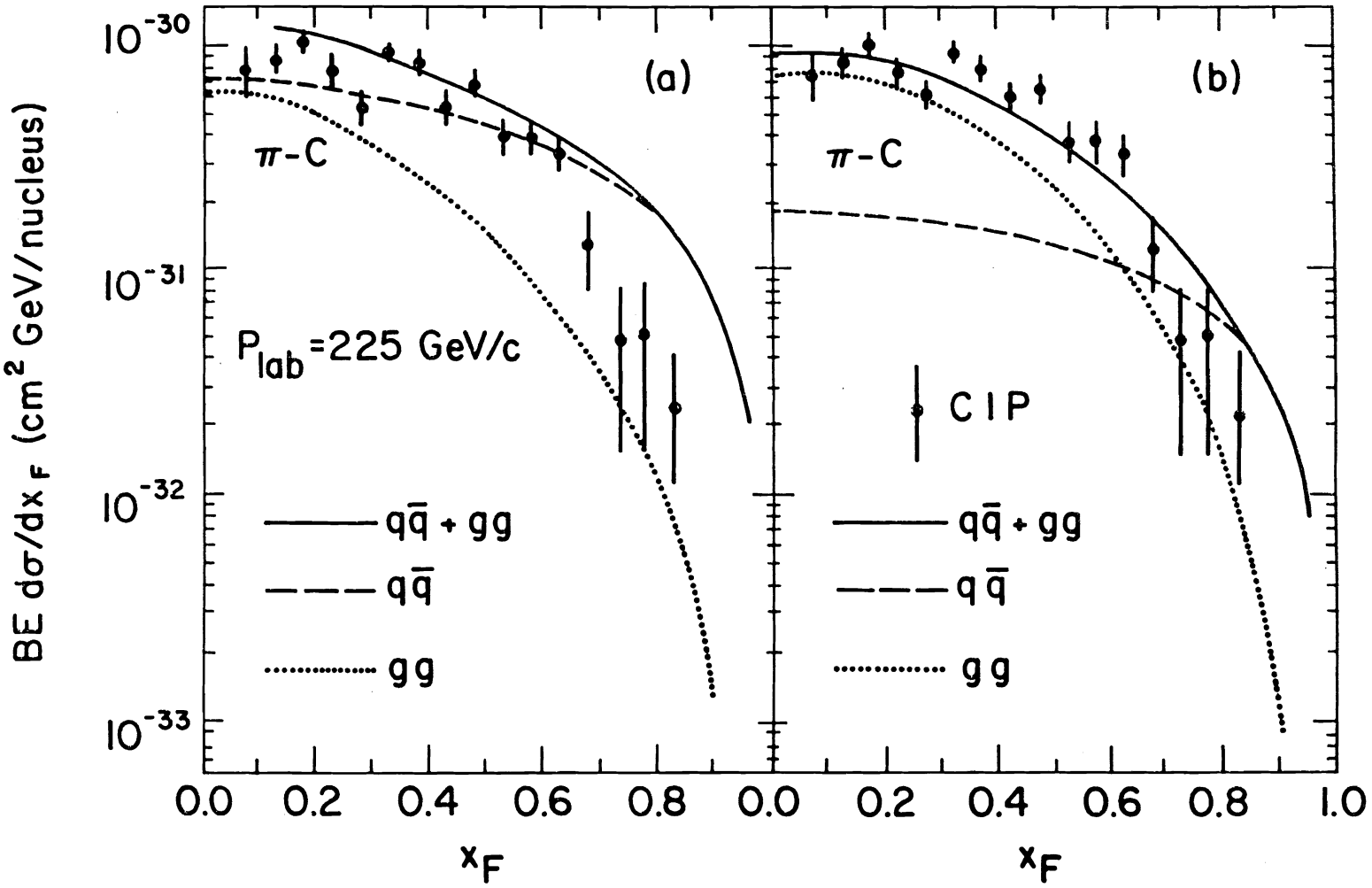

Figure 2.4 (taken from reference 21)
calculation of BE d /dx vs x
(a) uses dynamical QCD structure functions
(b) uses counting rule structure functions

ψ'(3685) were included, this model explained the J/psi cross-section reasonably well. According to this model, In π^-p interactions the quark fusion contributed substantially. This model could predict the cross-section as the function of Xf as well as the previous models. The authors claimed that they could predict the differential cross-section as the function of transverse momentum better.

Besides the cross-sections as a function of the CM energy and Xf as mentioned above, a lot of experimental data concerning the production mechanism exist. One class of experiments was the comparison of the J/psi cross-sections from different incident particles. NA3 Collaboration [ref. 14] got the following ratios of J/psi production cross sections for various particles, with respect to π^- induced cross section at the same incident momentum.

incident particle	Momentum GeV/c	H_2 target	Pt target
K^-	150	0.89+0.05	0.98+0.05
$\bar{P}$	150	1.02+0.1	0.90+0.06
π^+	150	0.95+0.03	1.010+0.013
K^+	150	-	1.02+0.10
P	150	-	0.42+0.04
K^+	200	-	1.09+0.12
$\bar{P}$	200	-	0.76+0.09
π^+	200	0.92+0.03	1.016+0.006
K^+	200	0.81+0.10	0.83+0.10
P	200	0.58+0.07	0.53+0.05

From the above results, we can say that at lower CM energy, both quark fusion and gluon fusion contribute if valence antiquarks are present as in π^-p and $\bar{P}P$ interactions. At higher energy the gluon fusion appears to contribute more. From our experiment and other experiments[ref. 1, 27-28], about 30% of J/psi are decay products of the χ states in π^-N interactions, The ratio of produced $\chi 1$ and $\chi 2$ states reveals that in the π^-N interactions the χ production can be explained by a combination of quark fusion and gluon fusion, but in the pN interation, the χ production can be accounted for by gluon fusion only.

Another way to explore the production mechanism is to study the associated charged particles in the J/psi events. So far there are only a few experiments[ref. 29-30] presenting such data. The following is a discussion of the simple model about the forward charge flow in the J/psi events and the related data so far.

Naively, if the J/psi is produced by quark fusion, then for π^- beam, the $\bar{u}$ quark will annihilate with the u quark in the nucleon to form the J/psi leaving the d valence quark in the forward direction as shown in Figure 2.5. The d quark continues its trajectory in the forward direction and fragments into hadrons. In the similar way a diquark from the nucleon fragments into hadrons in the backward direction. Because our acceptance in backward hemisphere was low, we were not able to study the target fragmentation region. Our target is not an hydrogen target, one may worry about the complication from the

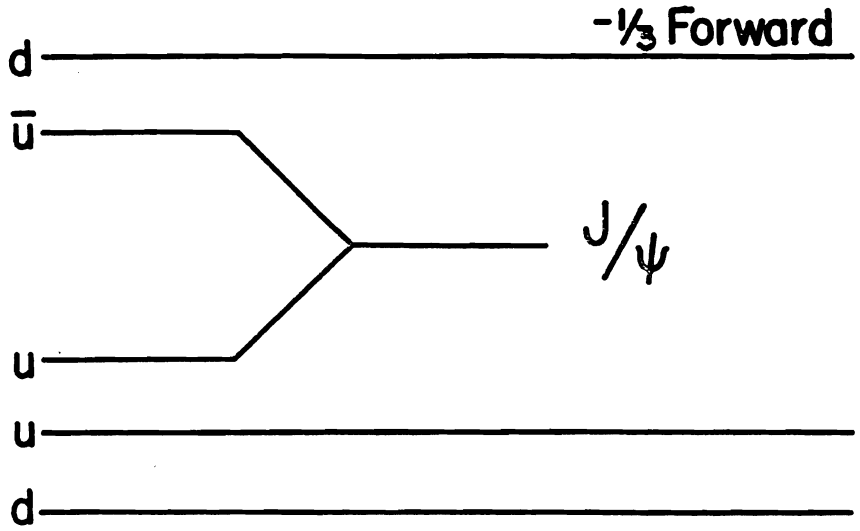

Figure 2.5

Forward charge for quark fusion

nuclear effect. Experimental results[ref. 31] showed that while in the backward direction one saw the nuclear effect, in the forward direction, the fragmentation could still be treated like in the elementary process. In recent years, people have learned the fragmentation more than before, especially through the jets study in e^+e^- colliding experiments. P. Söding in a summary talk[ref. 32] pointed out that, as the colour string between quarks or diquarks breaks, a quark anti-quark pair or diquark anti-diquark pair will be created from the vacuum, the ratio of the probabilities of diquark pair creation over quark pair creation is about 10%. Among the quark pair creation, if we assume the chances of $u\bar{u}$ creation and $d\bar{d}$ creation are the same, the ratio of $s\bar{s}$ creation over $u\bar{u}$ or $d\bar{d}$ is about 0.3-0.4. This value is somewhat smaller than the value in the standard Field-Feynman fragmentation model. In that model, it is assumed that the production of $u\bar{u}$, $d\bar{d}$ and $s\bar{s}$ pairs is with the probability of 0.4, 0.4 and 0.2. From this assumption, the net charge of d quark fragmentation will be -0.4. There is good evidence that this is correct from neutrino experiment[ref. 33]. The reason is the following, when the d quark from π^- and diquark from proton go apart, the colour string, or flux, will break into quark anti-quark or diquark and anti-diquark pair. For simplicity, we neglect the diquark anti-diquark pair creation here. Because the net charge of the quark antiquark pair created in the middle of the string is zero, in the forward hemisphere, only the original d quark and the last antiquark will contribute to the net charge. From the probability of different

quark antiquark pair creation mentioned above, the net charge of the d quark fragmentation will be -Ø.4, This value equals to $q(d)+Ø.4q(\bar{u})+Ø.4q(\bar{d})+Ø.2q(\bar{s})$. If we use the ratio of $u\bar{u}$, $d\bar{d}$ and $s\bar{s}$ pair creations as 1.Ø to 1.Ø to Ø.3-Ø.4, the net charge of d quark fragmentation will be somewhat more negative than -Ø.4. If the J/psi is produced by gluon fusion, then both $\bar{u}$ and d valence quarks will fragment into hadrons having the net charge -1 in the forward direction(figure 2.6). But in our experimental energy region, the forward fragmentation from beam particle is not separated from the backward fragmentation perfectly, the overlap of the charges between forward hemisphere and backward hemisphere or leakage of the charge through y=Ø plane depends on the CM energy. The experimental results[ref. 34-35] and some model predictions are in figure 2.7. For normal $\pi^- p$ interaction, the average forward charge should be -1 if the separation between forward hemisphere and backward hemisphere is perfect. From this figure, we can say that although at infinite CM energy, the forward charge is consistent with -1, but at our energy, the forward charge is only about -Ø.7. The beam fragmentation and the target fragmentation are far from separating one from the other completely. We will use this dependence of the forward charge as a function of the available energy in our analysis.

As mentioned in the first part of this chapter, the J/psi could be produced through quark fusion and/or gluon fusion, also the quark structure function is harder than the gluon structure function. So we expect to see more quark fusion contribution in higher Xf region of

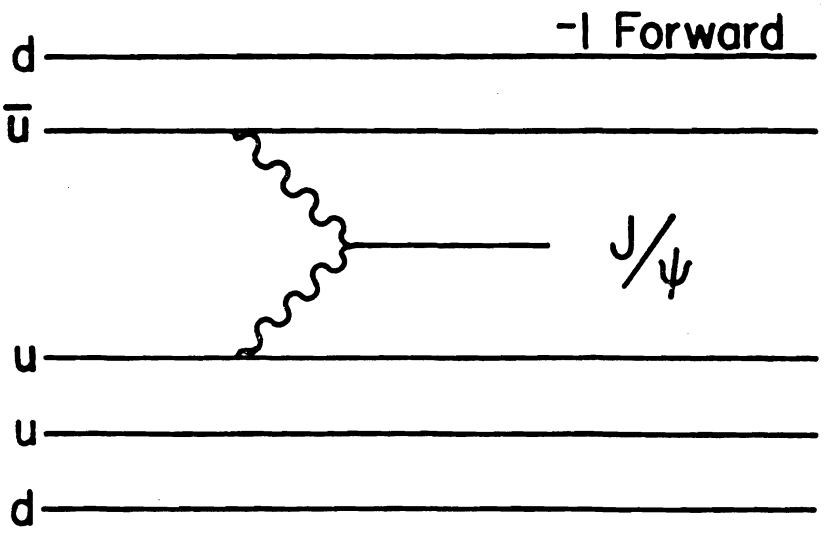

Figure 2.6

Forward charge for gluon fusion

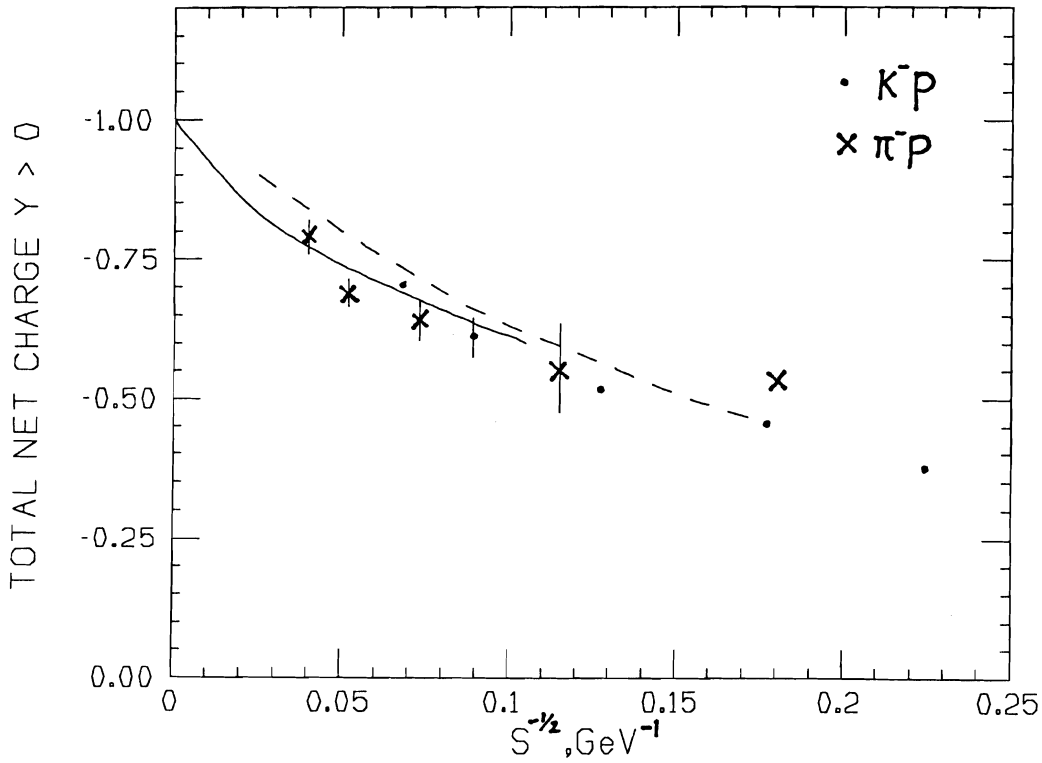

Figure 2.7

Net forward charge in k^-p and π^-p collisions as a function of $s^{-1/2}$, compared to DTU (solid line) and Lund model (dashed line)

J/psi particle than lower Xf region, therefore we expect that the net forward charge will become less negative in higher Xf region than lower Xf region in π^- p interactions.

Another way to learn the quark fragmentation is the study of charged particle multiplicity. The charged multiplicity is a function of CM energy, roughly $\bar{N}$ =A+B ln s. Here $\bar{N}$ is the average multiplicity and s is the squared CM energy. As the study[ref. 36] showed, if we subtract the leading particle effect, or if the effective energy available for particle production is used, the multiplicity as the function of energy is the same in hadronic interactions and in the e^+e^- interactions(Figure 2.8). So it is better to study the charged multiplicity using the available energy of the hadron system under study. But the charged multiplicity distributions in pp interactions are wider than those in e^+e^- interactions. The dispersion of the charged multiplicity in e^+e^- interactions is about 0.3-0.35 and the dispersion of the charged multiplicty in hadronic interactions is more than 0.4[ref. 37].

The forward net charge in the Drell-Yan process should have -0.4 net charge in forward direction, this is verified by one experiment[ref. 29]. This experiment collected J/psi events and high mass muon pairs. Its measured forward net charges for the Drell-Yan, the J/psi events and the normal interaction events are -0.36 +/- 0.05, -0.60 +/- 0.08 and -0.76 +/- 0.1 respectively. The authors in ref. 29 concluded from the forward charge flow study that the J/psi production

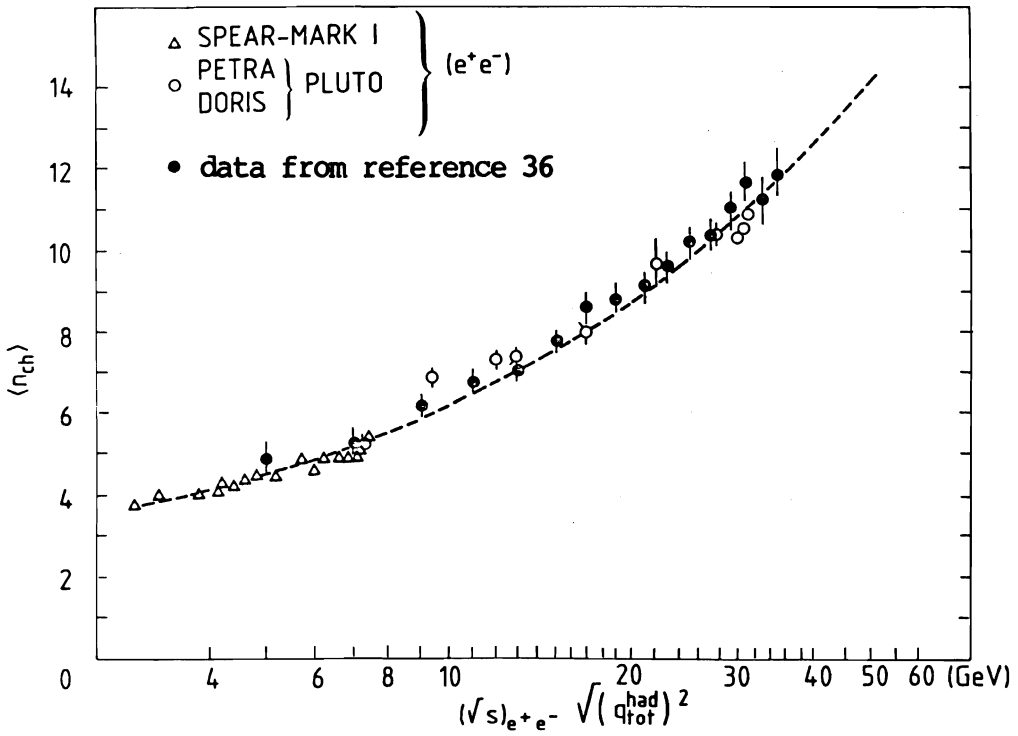

Figure 2.8

Charged multiplicity as a function of CM energy in e^+e^- interaction and as a function of effective energy in hadron interaction

in their experiment(190 GeV/c π^- beam particles hitting on a beryllium target) is through the quark fusion 40% of the time. By studying the forward charge in J/psi events as the function of Xf, H. Budd et al.[ref. 30] showed that their data were not consistent with the quark fusion plus gluon fusion model.

From the above, the study of the forward charge flow in the J/psi events can help us to understand the production mechanism. We want to know what we can learn from the data collected in E673.

CHAPTER 3 APPARATUS

experiment E673 was run at Fermilab in the muon lab from January to April in 1982. Its setup is similar to the preceding experiment E610. A lot of detailed apparatus descriptions have been given by other students in their theses (Schoessow, Hahn, Budd, Graff, Lukens), I will refer to them accordingly.

Figure 3.1 is a top view of the equipment in the muon lab. The laboratory coordinate system was referenced with respect to the Chicago Cyclotron Magnet (CCM). The origin of the coordinate system was at the center of the CCM, the z-axis was along the beam line, the y-axis pointed up, the x-axis was from right to left as viewed from upstream. The magnet has a gap of 129 cm and a pole radius of 216 cm. After E610, its old coil was replaced by a superconducting one to save electricity. During E673 a central field of 1.22 tesla was chosen giving a charged particle a momentum kick of 1.84 GeV/c in the x direction.

The magnetic field was mapped using a Fermilab ziptrak system. A magnetic sensor moved on an aluminium track that was assembled along the beam direction, this track was put at several different x y positions to cover various regions in the magnet. Every 3 cm along the track the x y z components of the field were read simultaneously by the sensor into a computer. The sensor read the relative field strength and the scale of the field was fixed by a nuclear magnetic resonance device. Figure 3.2 shows the vertical component of the field strength

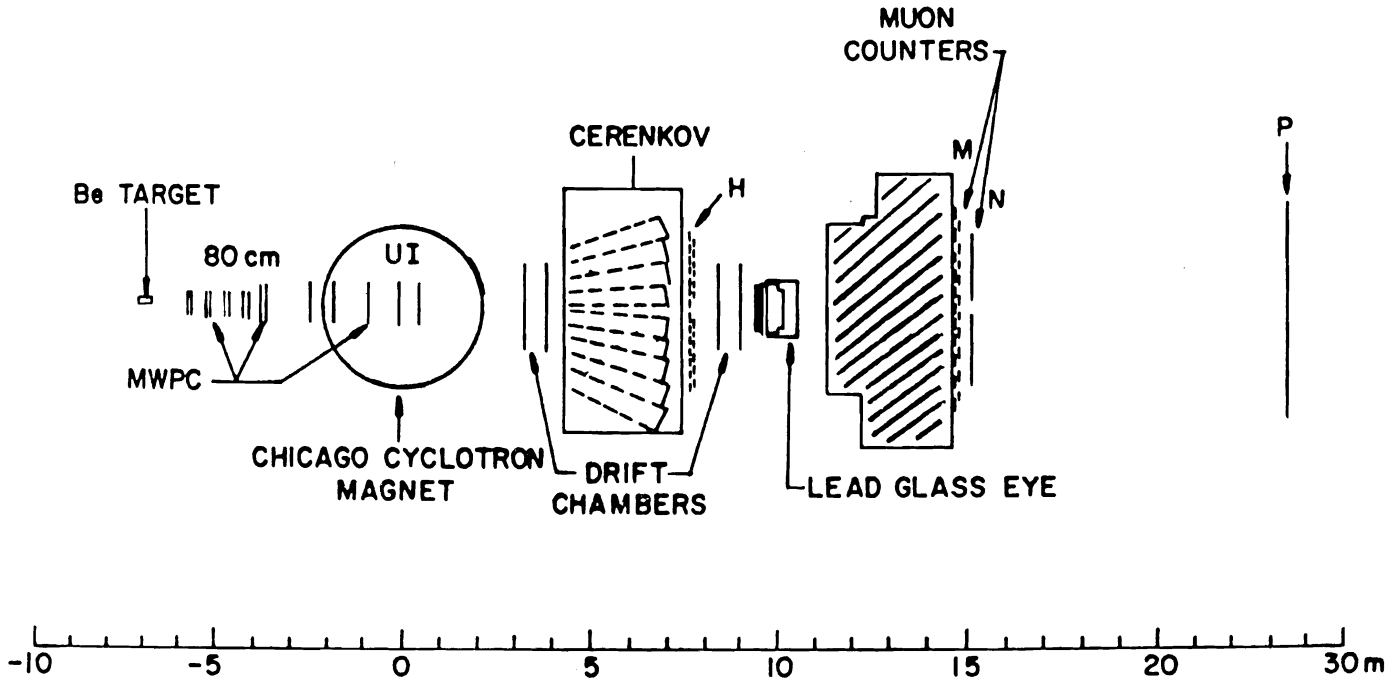

Figure 3.1

The top view of E673 apparatus

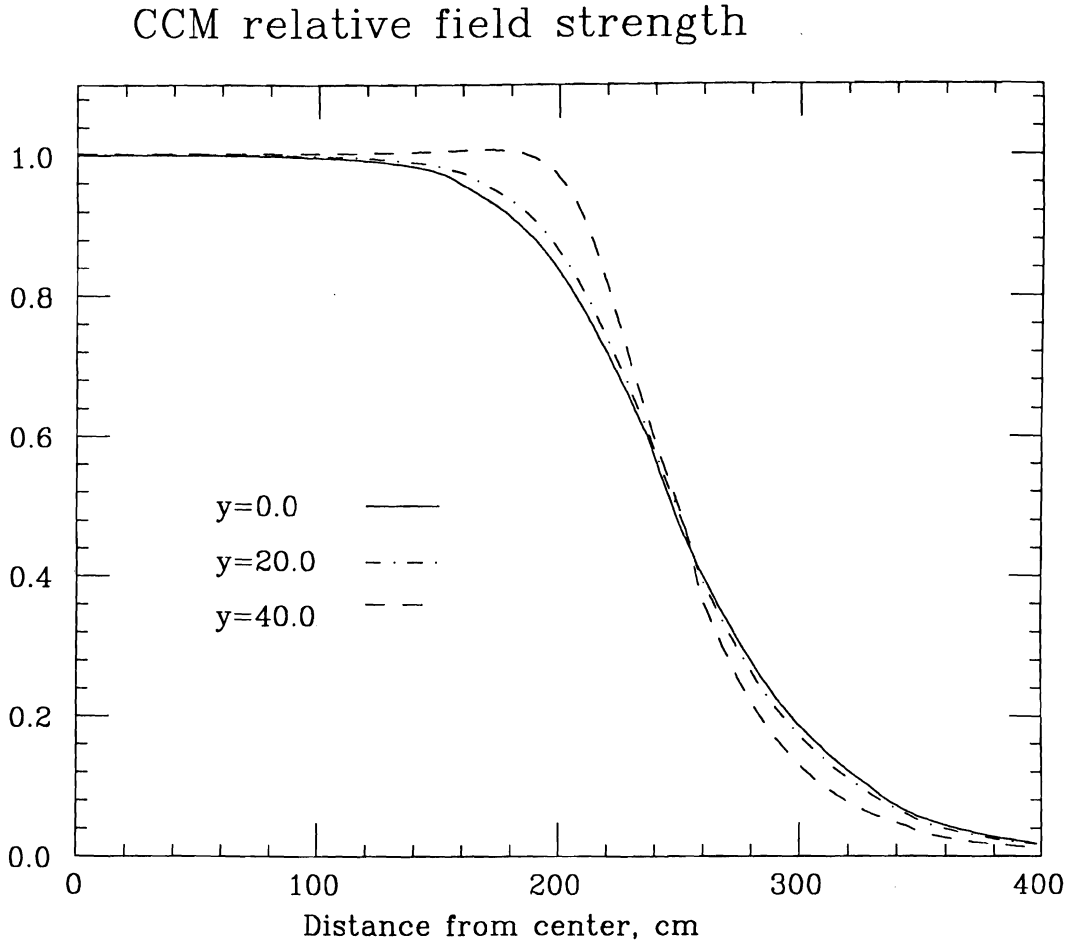

Figure 3.2

The relative y component of the CCM magnetic field

at different y positions

along three central lines (x=0, along z-axis) at different y positions. The current in the magnet was monitored throughout the experiment and it fluctuated no more than 0.2 percent, in the analysis we treated the magnet field to be invariant in this experiment.

In the following, I am giving a brief description of the apparatus from upstream to downstream. The exact geometric parameters used in the analysis were listed in Appendix B of Lukens' thesis[ref. 38].

3.1 Beam line

A slow spill proton beam of 400 GeV was extracted from the main ring of Fermilab accelerator. This beam hit a thick steel target and generated secondary particles of all kinds. Then a series of bending and focusing magnets selected charged particles of certain momentum and transported them to the muon lab. The beam momentum was centered at 185 GeV for the negative pion beam. For proton beams we set the momentum at 200 GeV for about one week and at 250 GeV for about two weeks. The average beam intensity was about three million particles per 0.7 second spill.

Figure 3.3 shows the beam line in x view. BH1 to BH6 are six scintillation counter arrays, each array consists of eight 1.8 cm wide (2.5 cm for BH1), 20.3 cm long and 0.6 cm thick elements. BC1 to BC6 are six beam chambers each having 20 cm by 20 cm active area and an effective wire spacing of 0.2 cm. BH1, BH2, BH3, BH5, BC1, BC2, BC4 and BC5 measured x-coordinates and the others measured y-coordinates as

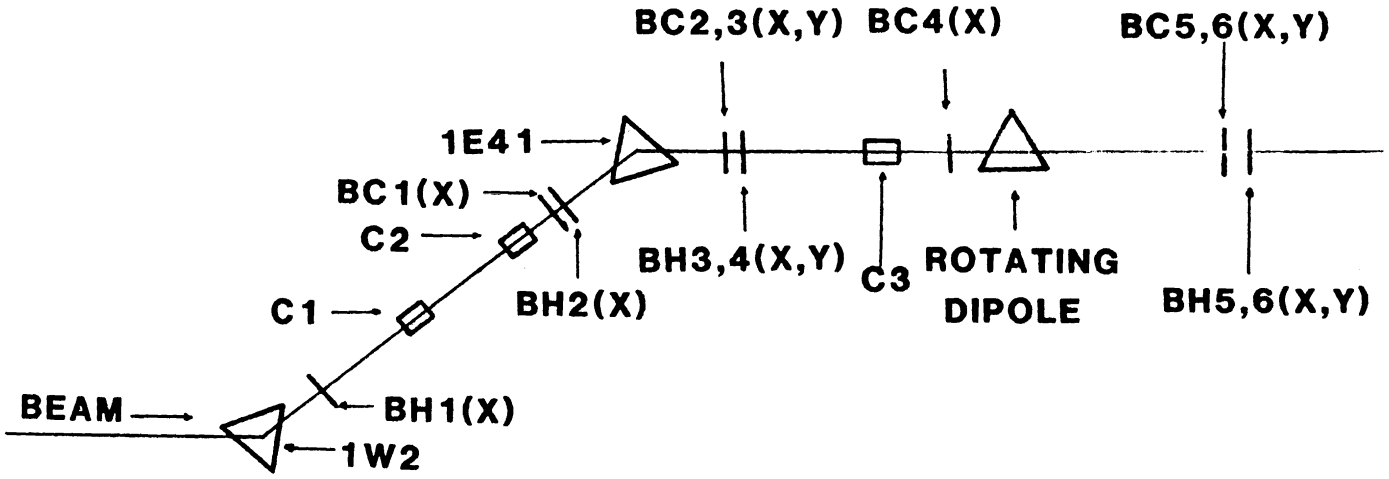

Figure 3.3

E673 beam line (not to scale)

shown in the figure. The beam hodoscopes and beam chambers were used to find beam particle tracks and to determine their momenta with the help of a bending magnet 1E41.

Three beam Cerencov counters c1, c2 and c3 were added to the beam line when we started to take proton data; they were used to differentiate pions from protons. The helium pressure in these counters was set at 4.62 psia for 200 GeV protons and at 2.96 psia for 250 GeV protons. These values were well above kaon threshold and 0.6 psia below proton threshold. In the analysis, a particle triggering two or more Cerencov counters was regarded as a meson, otherwise a proton.

The rotating dipole magnet was used only in the calibration of the lead glass system as a means to direct electron or position beams to various lead glass blocks.

Several veto counter sets were in the beam line to prevent triggering on bad beam events.

3.2 Target and trigger counters

The beryllium target was 13.18 cm wide, 7.62 cm high and 7.62 cm deep. It corresponded to 0.22 radiation length and 0.14 or 0.23 nuclear interaction lengths for pion or proton beams respectively.

Signals from three scintillation counters TØ, T1 and T2 were used to form an interaction trigger. The counters are shown in Figure 3.4 along with the target. TØ was 5 cm high and 7.6 cm wide, T1 and T2 were 12.7 cm by 12.7 cm; all of them were Ø.16 cm thick. These counters were set to be 1ØØ% efficient for minimum ionizing particles. Two logic signals ULO and UHI were formed from them. ULO was the logical and of the outputs of these counters, so every particle going through them produced a ULO signal. UHI was similar except that the outputs from T1 and T2 were attenuated before going into the discriminators, the ideal setup of the attenuations should be that UHI fired only when an interaction occured in the target (one particle passed TØ and more than one particle passed T1 and T2). Because the pulses from these counters have a Landau distribution, it was still possible to generate a UHI signal without an interaction in the target. We adjusted the attenuations such that the ratio of UHI/ULO was 7% when the target was not in place and 22% when the target was in place; the difference of 15% between the two cases corresponded to that expected due to the nuclear interaction length of the target. We required a signal from at least one H counter outside the beam area in the trigger logic to insure that there was an interaction in the target.

3.3 Multi-Wire Proportional Chambers (MWPC)

Five MWPC called the 8Ø cm chambers were placed downstream of the target. Each chamber had two perpendicular planes 12.6 cm apart, both having an 8Ø cm by 8Ø cm active area with Ø.16 cm wire spacing. Its

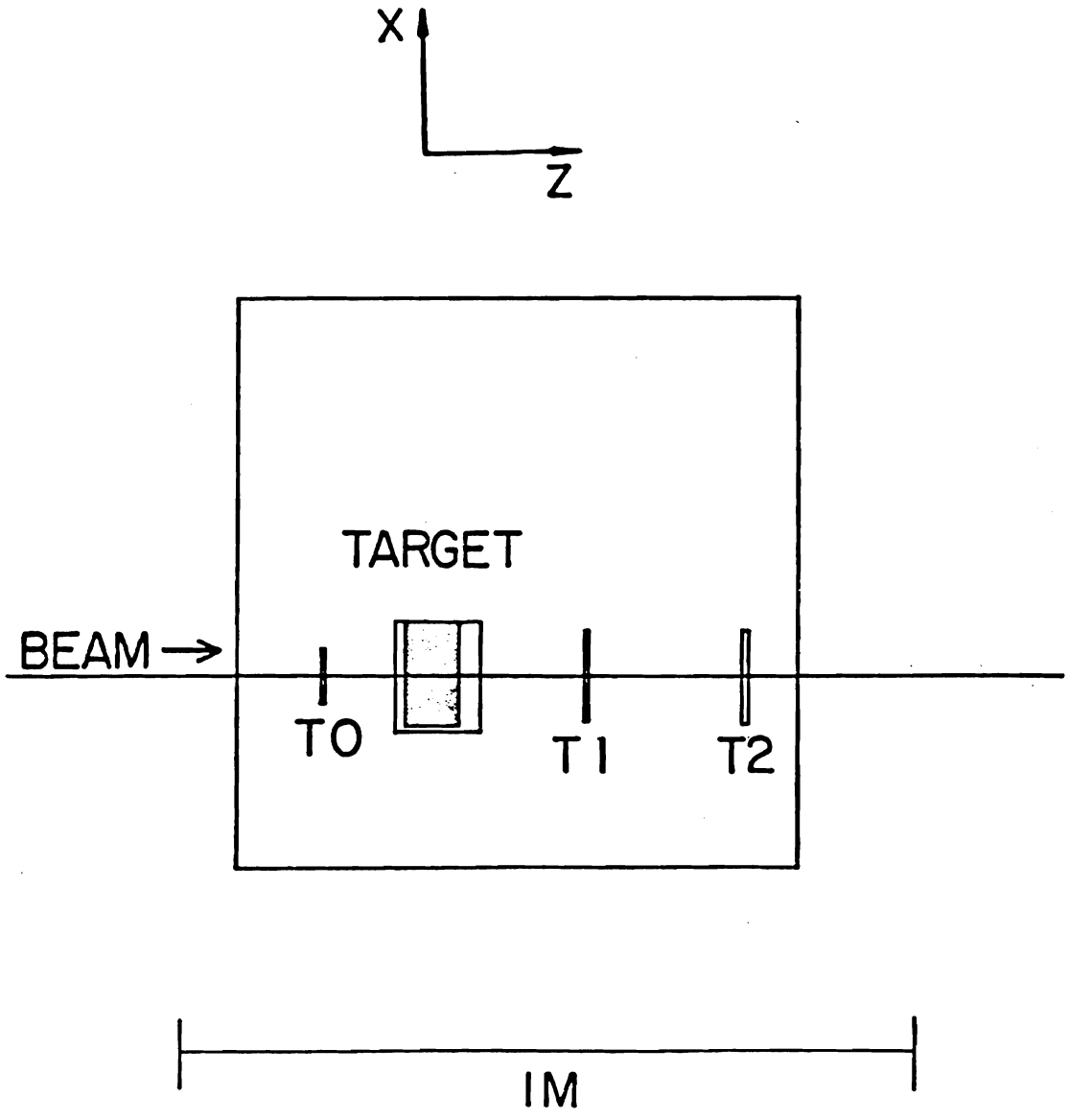

Figure 3.4

Target and target counters

construction and operation were described by Hicks[ref. 39]. The first four chambers were oriented such that the upstream plane measured y position and the other measured x. The fifth 80 cm chamber was tilted 45 degree from others to help matching x-view tracks with y-view tracks in pattern recognization. Tracks in these chambers should form straight lines because they were out of the magnetic field. In this experiment, these chambers were more than 90% efficient except that the y plane in the third chamber was turned off soon in the beginning because it sparked badly.

Another five so called UI chambers were put inside the magnet following the 80 cm chambers. Each chamber had three (u,y and v) planes (Figure 3.5). The y-measuring plane had an 106 cm by 96 cm active area with 0.2 cm wire spacing. The u and v planes were tilted about +/- 11 degrees from x-measuring position covering an area 126 cm wide and 96 cm high with 0.196 cm wire spacing. A detailed description of their construction was given in Budd's thesis[ref. 40]. In this experiment the UI chambers had an efficiency of about 90%.

3.4 Drift chambers

Four drift chambers were placed downstream of the magnet. Each chamber has 60 cells and each cell was 4 cm wide in x, so the active area was 240 cm in x and about 150 cm in y. These chambers were designed to measure y position as well as x position of a hit, the anode wire measured x and the delay line measured y. The drift chambers worked in a common start mode, the UHI signal from upstream

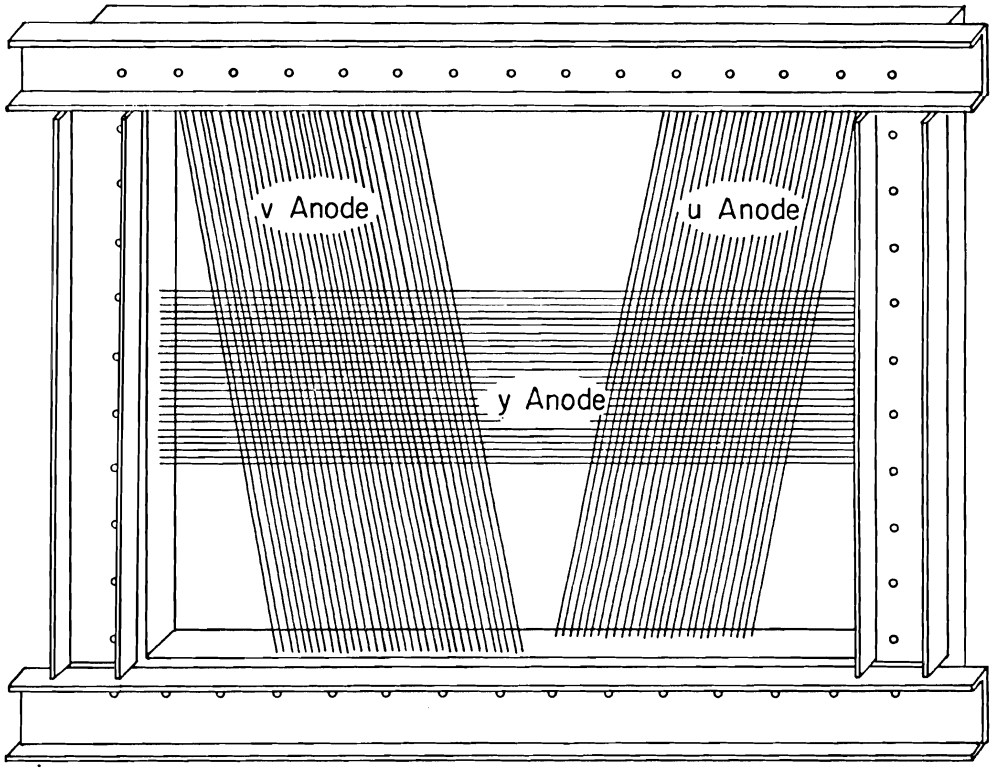

Figure 3.5

UI MWPC chamber viewed from downstream

logic served as a start signal. Figure 3.6 shows the cross section of a cell. Each cell had four signal outlets: anode left, anode right, delay line top and delay line bottom. These signals were registered in the TDC's as the time intervals between the moment when the start signal was created and the moments when these signals were generated. The x position was recorded as the time needed for the initial ionization to drift to the anode wire, the drift velocity was checked to be nearly constant in the field having the value of 0.0052 cm per nanosecond. The y position was recorded as times taken for the induced signal to reach top and bottom ends of the delay line. The resolution of the x position was about 0.03 cm and the anode efficiencies were about 0.8. Because the induced signals on the delay lines were quite weak, the delay line efficiencies were rather poor (0.6-0.7) and the y resolution was more than 1.5 cm. Due to the fact that we had better y information from the UI chambers, we did not use the y information from the drift chambers in the analysis.

3.5 Cerencov counters

Between second and third drift chambers there were 18 Cerencov cells. They were inclosed in a light tight plastic house filled with dry air (Figure 3.7). They were meant to separate kaons and protons from pions in the momentum region of 8-20 GeV/c. Because its bad performance during the experiment, they were not used in the data analysis. So we had to treat all the charged particles as pions in our analysis besides muons.

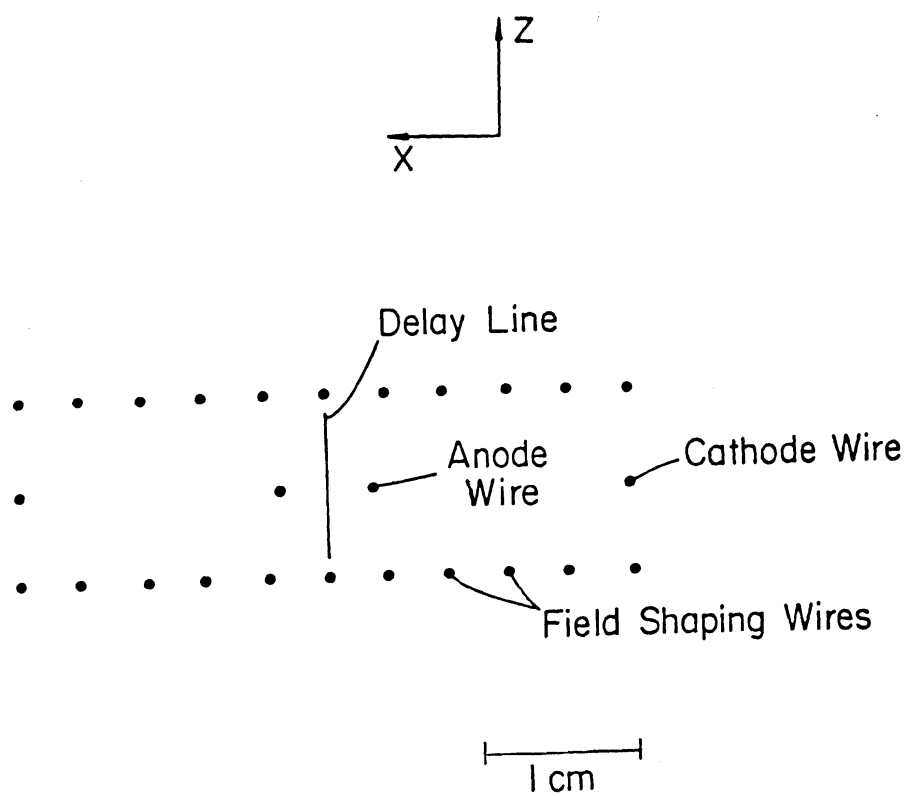

Figure 3.6

A drift chamber cell

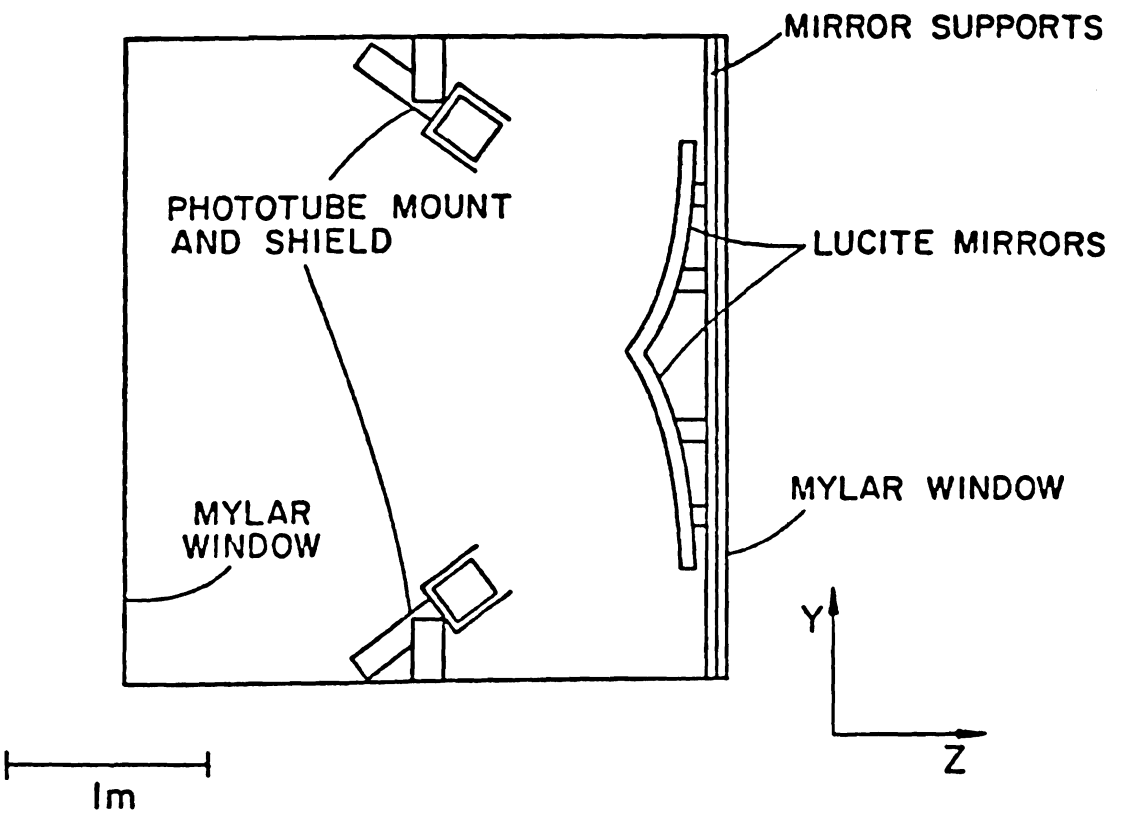

Figure 3.7

Side view of a Cerenkov cell

3.6 Hadron counters

An array of sixty scintillation counters was placed right behind the Cerencov house (Figure 3.8). Its preliminary use was to assist the Cerencov detector in particle identification. We tried to get y position of the tracks in these counters by feeding their pulses to TDC and ADC, but to our disappointment, the y resolution of a few cm was not much a help in pattern recognization so this information was not used.

3.7 Photon detector

The photon detector was essential in chi physics and a lot of effort was devoted to its construction and its performance. But because its data was not used in this paper, I will simply mention its characteristics and leave detailed information to be found in Hahn's and Lukens' theses[ref.38 and 41]. Its side view is shown in Figure 3.9. The overall detection efficiency of the photon detector including geometric acceptance was about 0.2. The energy resolution could be represented by delta(E)/E=0.0011+0.085/E (E is the photon energy). The position resolution was about 0.6 cm. Actually the efficiency, the energy resolution and the position resolution were complicated functions of photon energies, their positions and the photon numbers in each event. The given numbers above just roughly indicate where they are.

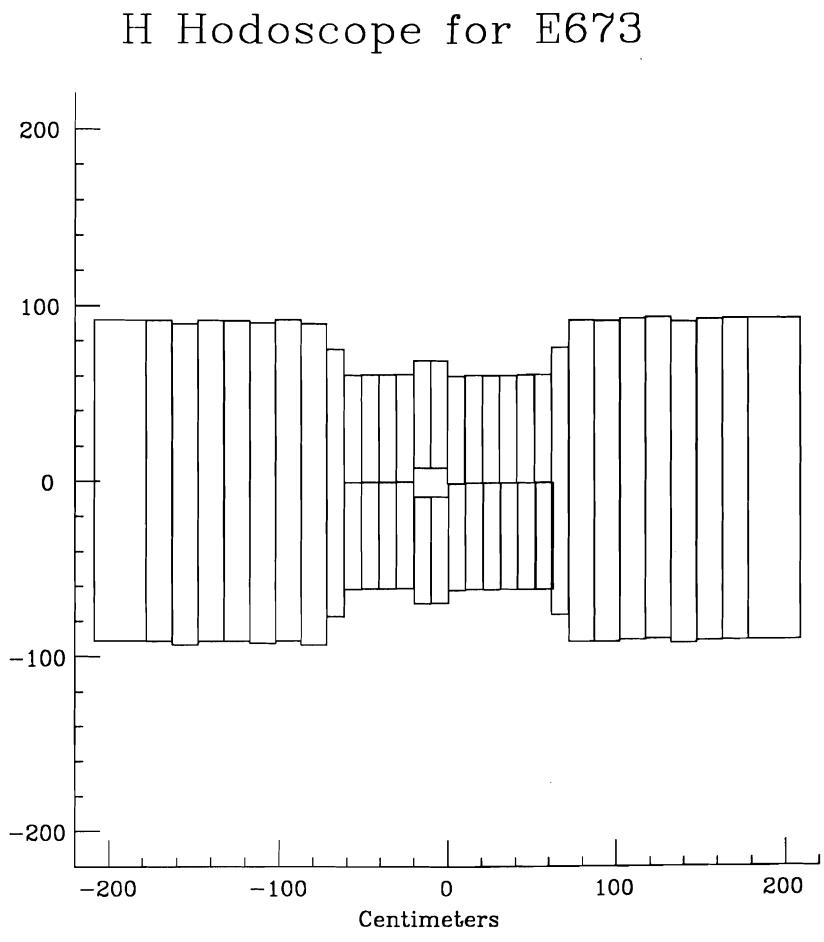

Figure 3.8

The H hodoscope array

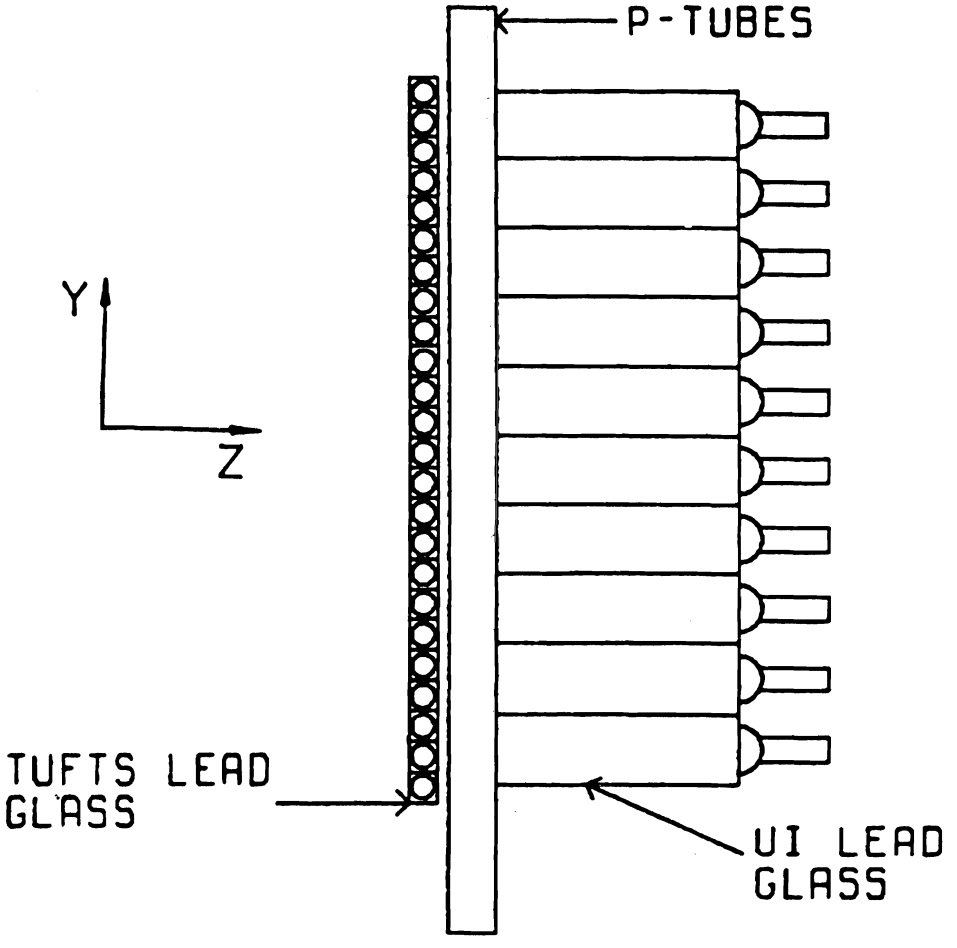

Figure 3.9

Side view of the photon detector

3.8 Muon counters

Behind the photon detector there was a 4.5 meter steel wall stopping most of the hadrons. Right after the steel, there were two scintillation counter arrays called M and N counters (Figure 3.10 and 3.11). The M counter array had a bow-tie shape to bias the trigger to higher mass of two oppositely charged muon pair. There was another scintillation counter array called P counters (Figure 3.12) about eight meters downstream of the N array; originally it was put up in the hope that it would help the muon pattern recognization, but its acceptance was too small to be included in the muon identification.

3.9 Logic and the data acquisition system

The trigger logic diagram is shown in Figures 3.13-3.15. All the logic signals were at standard NIM levels. The main trigger used in the entire experiment was so called dimuon trigger. The requirements of the trigger are following:

A. Clean beam - each beam hodoscope has at least one hit in it and no more than one hit in BH5 and BH6, also no veto counter should light.

B. Interaction in the target - the UHI logic signal is triggered and there is one or more H counters having particles going through. Further UHI signals are blocked after one UHI signal has sent to main logic until it is reset by the main logic again.

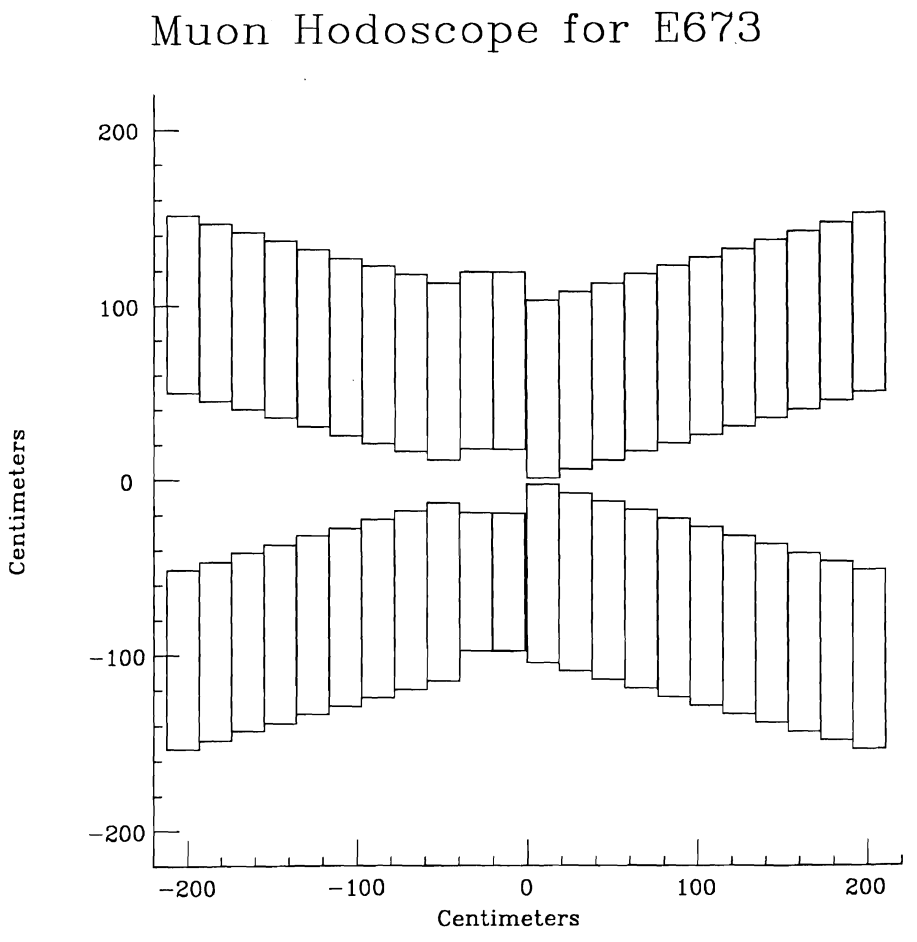

figure 3.1Ø

The M hodoscope array

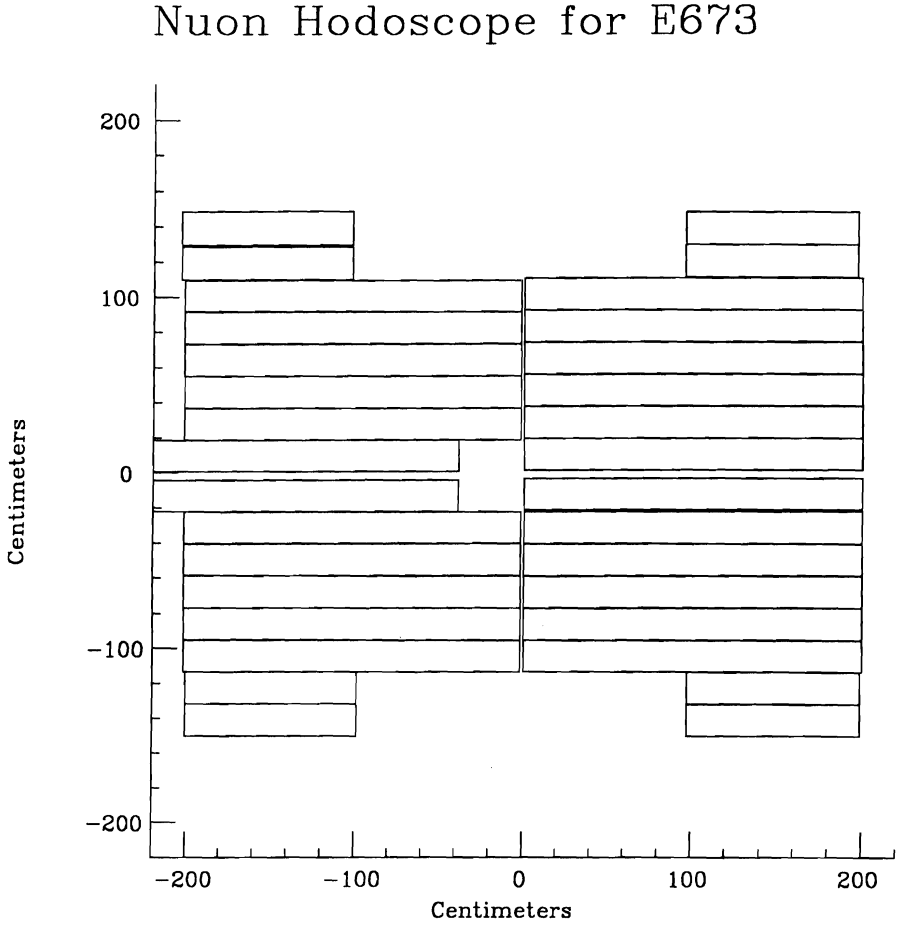

Figure 3.11

The N hodoscope array

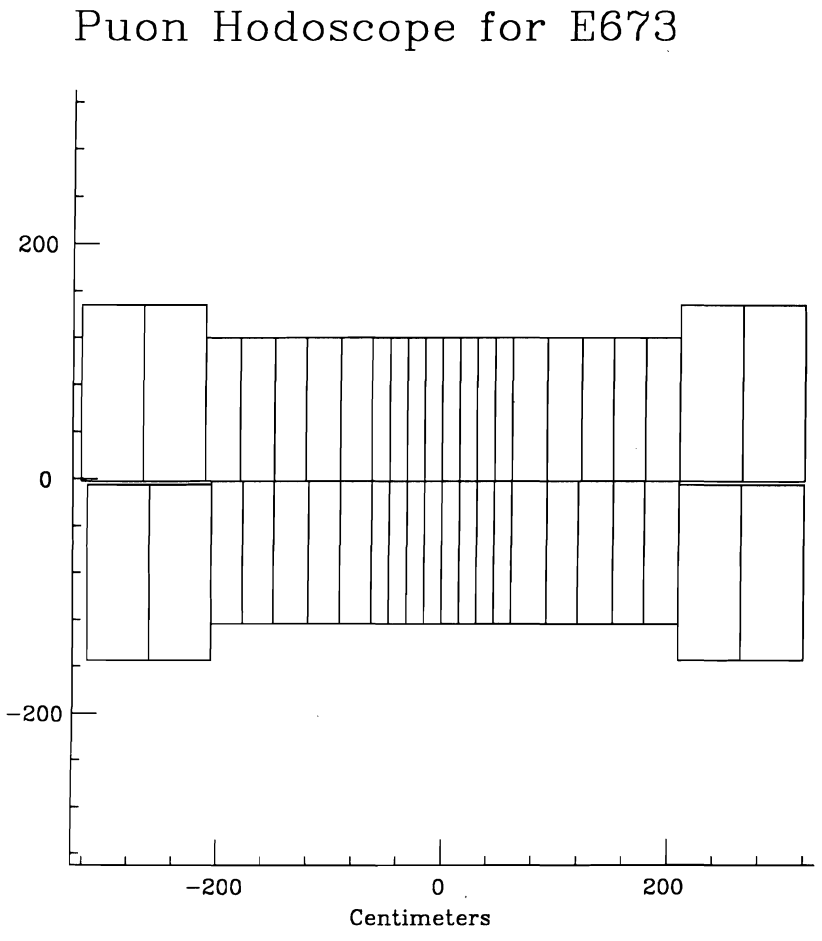

Figure 3.12

The P hodoscope array

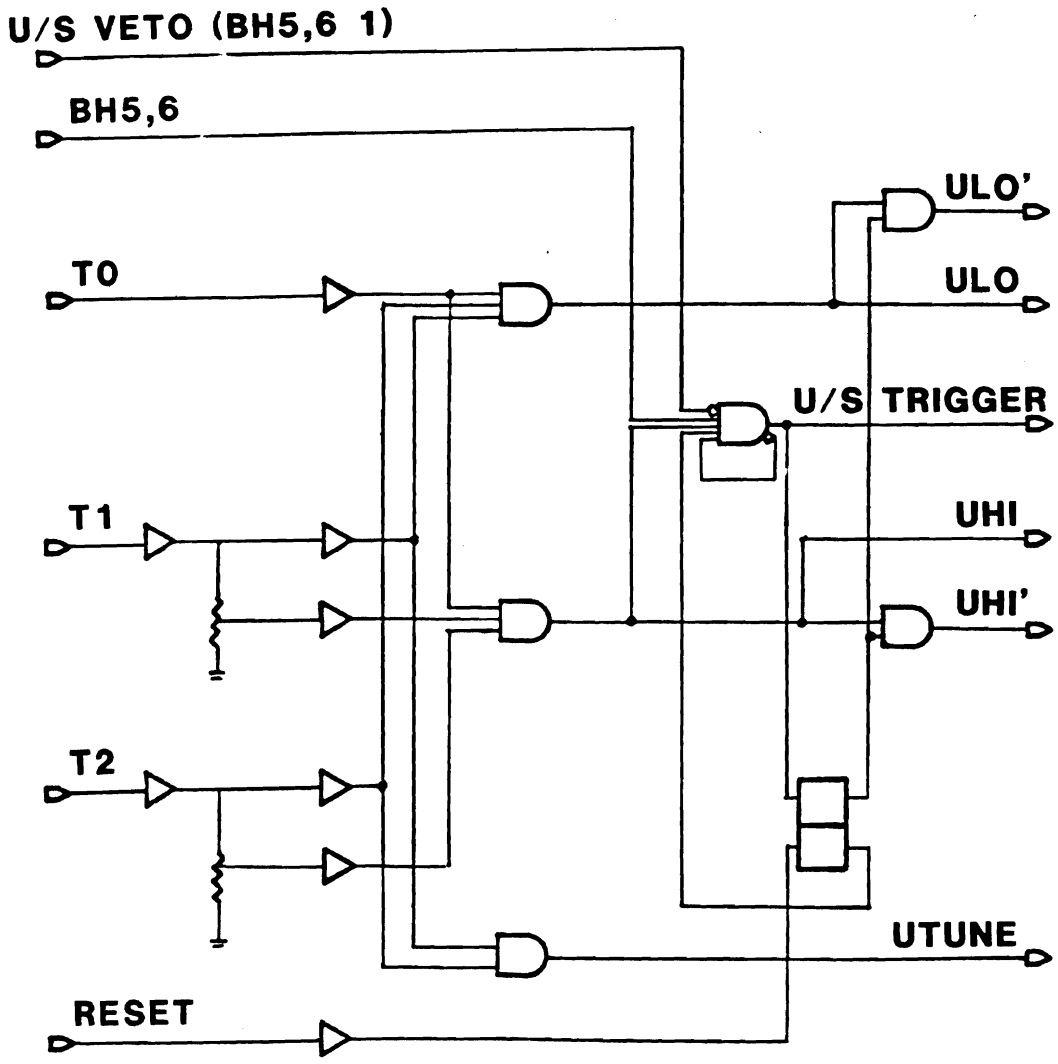

Figure 3.13

The upstream logic

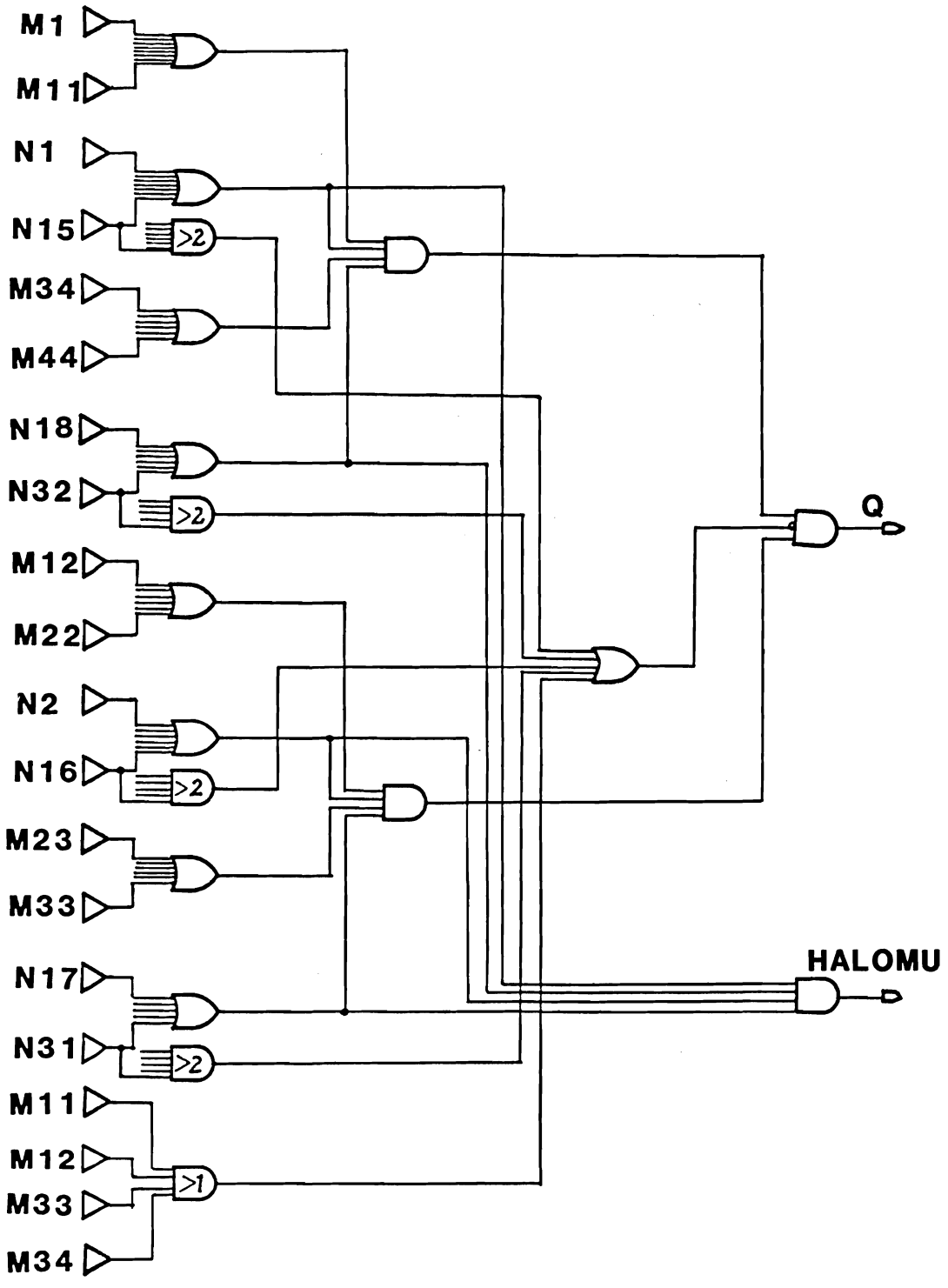

Figure 3.14

The downstream logic

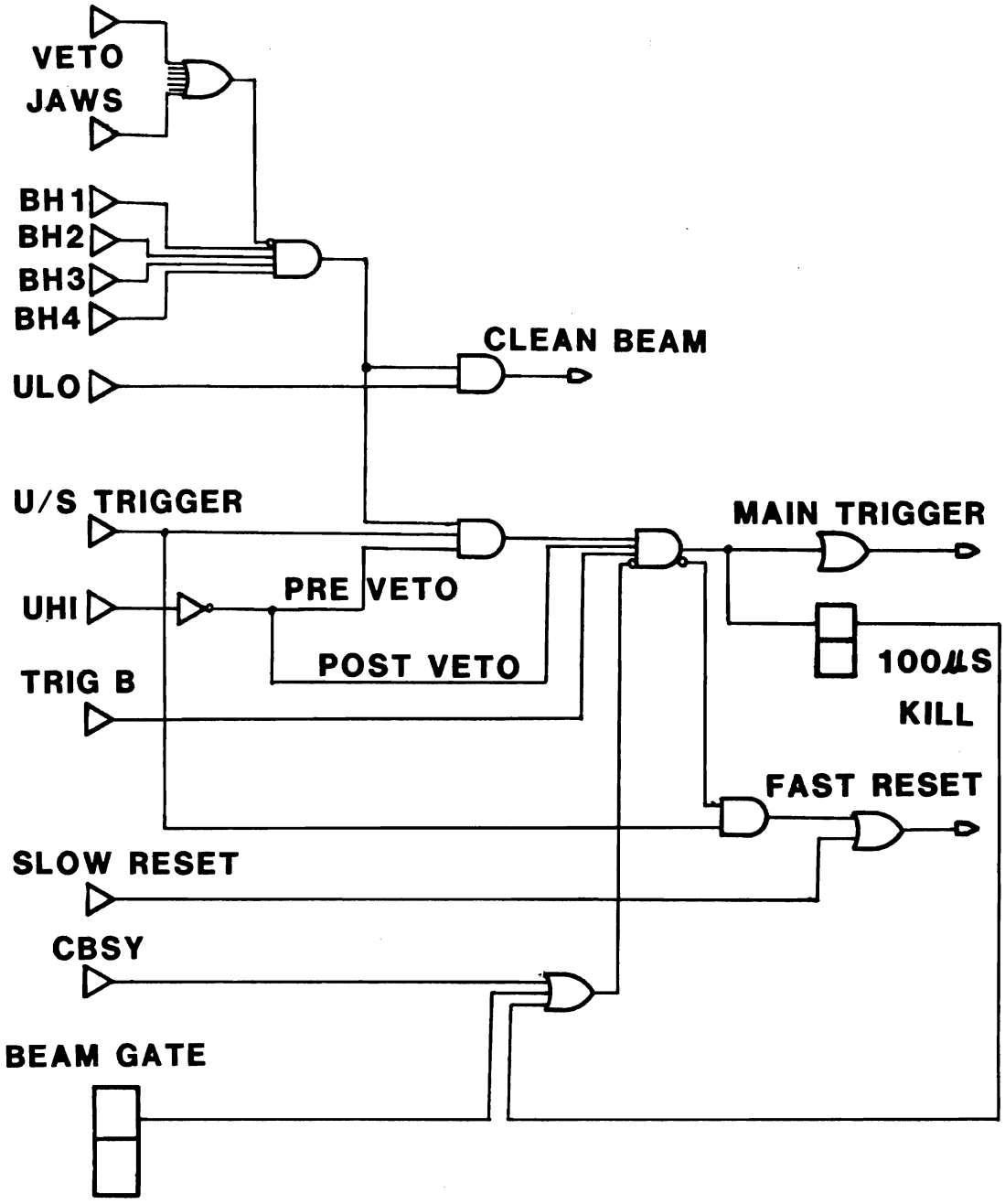

Figure 3.15

The main logic

C. Two oppositely charged muons - the M counters and N counters were divided into four quadrants geometrically, so there are two diagonally opposite quadrants pairs, if in one such pair, one or two (but not more than two) N counter in each quadrant is hit and there are hits in coresponding M counter quadrants, the trigger is satisfied. In order to avoid triggering on beam punch through, we vetoed the coincidence among four central M counters (M11, M12, M33 and M34).

Besides the above requirement, the trigger was disabled when the computer was logging data from the CAMAC system.

The data in all the detectors were locked in their readout electronics by the main trigger except that the UI chambers and the drift chambers were initiated by the upstream trigger signal.

Standard CAMAC system was used as the bridge between the detectors and the PDP11-45 computer. Every time the trigger condition was satisfied, the computer sent a signal to block any further triggering until it read in all the data and was ready for another event; meanwhile it issued a command to transfer all the data to the corresponding CAMAC modules. The data stored in CAMAC modules were read into the computer in sequence. These data were temporarily stored in the disk area up to 20 events, at the time the computer was not busy it wrote the events to a magnetic tape and made room for new events. The computer also had the ability to analyse the event on line, making one event display and collecting statistics; people on shift checked them to make sure the equipment was working properly.

CHAPTER 4 ANALYSIS

Over two millions pion induced triggers and about one million proton induced triggers were recorded on magnetic tapes. We had to process all the events to extract useful information, mainly the J/psi signal and the tracks of charged particles produced in J/psi events. To achieve this goal, several steps were taken. First, the positions of chambers and hodoscopes were determined with respect to each other and related to the magnetic field of CCM. Second, the J/psi signal was extracted from the data, that is, we had to find those events which had one or more oppositely charged muon pairs with the invariant mass of these muon pairs in the J/psi region. Third, all the tracks of charged particles in each event of the J/psi sample were found. The analysis will be discussed below step by step.

4.1 Alignment

All the equipment had to be aligned with respect to the Muon lab coordinate system accurately before anything could be done. Using the procedure described below, we achieved the alignment accuracy to the level such that: the positions of the wire planes in the direction they were measuring were known to a few hundred microns relative to each other, the relative position between the entire chamber system and the CCM was known to a few millimeters, and hodoscope positions were known to within a few millimeters.

For the purpose of alignment, three sets of data were taken during the experiment at low beam intensities with the CCM off, they were called ULO, UHI and HOLO. The ULO data was taken when the interaction target was out of beam line; only a single beam track went through the equipment. The HOLO data was triggered by a coincidence between one of the beam veto jaw counters and one of the N counters; one track parallel to the beam line but out of the beam area was present. The UHI data was triggered by the interaction in the target; several straight-line tracks from the interaction vertex in the target were registered in the equipment.

To start with, the positions of the chambers which were measured by tapes were used in the alignment program. The z position of each chamber was measured against the survey targets whose relative positions to the CCM were known, the x position was measured against the beam line marks on the lab floor, the y position was measured by survey instrument against the beam survey marks on the magnet. At this point, the nominal tilt angles (Ø degree for x planes and 9Ø degrees for y planes, etc) were used.

To determine the relative positions of the MWPC, the ULO data was used. In each event, one straight-line track was reconstructed using the hits in beam chambers 5 and 6, the 8Ø cm chamber planes and UI chamber planes. Because the planes had not been aligned properly, the straight-line track finding used very loose requirement on track quality. Both x and y views of the straight-line were found, then an

alignment program minimizing the following χ^2 for each wire plane was used.

$$\chi^2 = \sum_i [(UMi - Xi*\cos\theta - Yi*\sin\theta - D)/\sigma i]^2$$

where UMi is the hit position measured by the plane;

Xi and Yi are the x and y positions of the track at that plane;

θ is the angle of the wires in the x, y plane measured counter clockwise from the +y axis as seen from downstream;

D if the offset of the plane in the wire measuring direction;

σi is the resolution of the wire plane (wire spacing over $\sqrt{12}$).

The sum is over many tracks.

By plotting chi-squared as a function of D, we found the best value of D which minimized chi-squared, at this value of D the residual distribution of the plane should be peaked at 0, where the residual was defined as UMi-Xi*cosθ-Yi*sinθ-D. The angles were determined by the similar method but using the HOLO data because it covered larger region of the planes, so the χ^2 was more sensitive to the changes of the angles. The overall offset of the MWPC related to the lab coordinated system was determined by checking the positions of several hodoscope elements. By comparing their positions determined from tracks found in the MWPC system with the positions measured by survey instruments, the whole chamber system was aligned along the beam line. The overall tilt angle of the MWPC system related to the lab coordinated system was determined by using the data taken when the magnetic field of the CCM was turned on. If the y axis was not aligned to be parallel to the magnetic field, the tracks found in the y view would have a small x

momentum component in the field and subject some bending. The tilt angle was obtained when the y tracks had minimum chi-squared values as they were fitted to a straight line.

The relative positions of hodoscope elements in one array were determined to within Ø.1 cm with a tape measure. Only the positions of a few elements in each hodoscope array were determined related to the chamber system from the data. By finding the edges of these elements, the hodoscope positions were determined typically to the accuracy of a few millimeters relative to the beam line.

The drift chamber alignment was done by using UHI data, because the signal from counters TØ, T1 and T2 was needed as a start time to record the drift time. The alignment of the drift chambers was more complicated than other devices. For example, extracting a track position from an anode time in a drift cell involved the anode wire offset, the tilt angle of the anode wire, the anode time, the drift velocity and the start time of each cell. Deriving a delay line position involved start time in each signal channel, propagation time for the signal to reach the end of the delay line and the propagation velocity. A lot of effort was made by Tom Graff in aligning the drift chambers, the detailed description of the procedure could be found in appendix B in Tom Graff's thesis[ref. 41]. Two points are worth mentioning here:

A. In principle, the drift chamber had to be aligned cell by cell for the start times and the drift velocities, and the study showed that cell by cell alignment did improve the position resolution in x and y views. But in our data, because the relatively poorer x resolution of upstream track measurement, the cell by cell alignment could not improve the J/psi mass resolution much, so it was not used in the analysis. A common drift velocity was used for all the cells and the nominal start times were used.

B. By treating each drift chamber as a whole, the overall offset and the tilt angle were determined using the method similar to that for MWPC chambers. To adjust the drift velocity, a two dimensional plot was made. The x coordinate of each point in the plot was the anode time, the y coordinate was the difference of the anode time from a calculated time, which was the ratio of the predicted position of a hit in a cell over the drift velocity. A straight line was drawn through the points in this plot, the real drift velocity corresponded to zero slope of this line.

4.2 Upstream track finding

Particles coming out of the target in an interaction followed straight-line paths as they passed through the field free region upstream of the CCM. The goal of the upstream track finding program was to reconstruct these straight trajectories. The detailed description of the upstream track finding is in James Bellinger's thesis[ref. 42]. Below is its short description.

This program dealt with the tracks in x and y views separately. It began with a beam track finding routine, which found the energy of the beam particle and its hit position in the target using beam chamber and beam hodoscope informations. Based on this, a vertex finding routine was called to get a better vertex position. In this part of the program, The four x-measuring planes and the three working y-measuring planes of the 80 cm chambers and the y-measuring plane of the first UI chamber were used. In either view, the program found all the tracks having hit in each plane. From these tracks a more accurate vertex position was found by extrapolating the tracks back to a plane which was at the target center along z direction.

Linked with this new vertex position, a line was formed for each point in the chambers, the angle between this line and the beam line was recorded. In this stage, all eight y-measuring planes were used instead of four. Ideally all the points belong to a track should have the same angle. The program stored all the angles and compared them to find the tracks. It started from the smallest angle, this angle was compared with the angles in the other planes. If two angles from different x planes or three angles from different y planes were close to each other within certain limit, a line was formed using coresponding points. If these points fitted to a line reasonably well, a track was found and the angles used in this track were excluded from the remaining program. If no track was found, the smallest angle was excluded from the remaining program. The same process repeated with a new smallest angle until all the angles were tried. The found tracks

were projected into the target center plane in z direction, these projections and the previous vertex position were averaged to a new vertex x or y position. If the new vertex position was within Ø.4 cm of the previous one, it proved that the original vertex position was determined reasonably well, the program passed to the muon track finding. Otherwise the angle method had to go through again with the new vertex until the Ø.4 cm requirement was met or until this method repeated three times and finally gave up.

4.3 Muon track finding

The purpose of this program was to find only those tracks that pointed to the hit M and N counters, presumably they were muons, and to leave other tracks untouched. In this way we were able to run the program in a relatively short time and still find all the dimuon events.

The program started in the y view looking for the upstream y tracks pointing to the hit N counters. Due to some vertical focusing by the magnet, tracks in the y view were not exactly straight lines. Some low momentum tracks were bent more than 15 cm when they hit the M and N counters. For this reason, a window of 15 cm was set around each hit N counter. If the extrapolation of a y track was within this window, this y track was considered as a muon candidate. Now we had to find this muon candidate in the x view. There were two constraints in finding the track in x view: in the downstream, the M counters overlaped with that N counter under consideration were used; in the

upstream, the upstream x tracks that matched with the above y track were used.

The match of an upstream x track with a y track was determined by the following procedure. In the first four tilted MWPC planes (last two 80 cm planes and u and v planes of first UI chamber), the tracks experienced very little bending unless the track momentum was very low, in which case they could not reach the M and N counters to be identified as a muon. The hit positions in these four planes were predicted using the upstream x and y tracks, and if two or more hits were found in these planes, the x and y tracks were matched.

From one pair of such matched x and y tracks and one of the overlaped M counters, a road was formed in the x view as shown in the shadowed area in Figure 4.1. The muon track should be within this area. Here a momentum value was calculated using the upstream x slope and the x position at the middle of the M counter. With this estimated momentum the predicted hit position at the N counter was corrected for the vertical focusing. A some what narrower window around the N counter was set to see if the track still passed the N counter, this window depended on the value of the estimated momentum and it was 10 cm for 10 GeV tracks. The window around the M counter was also set to be quite wide. It was chosen as 5+75/ap, ap was the absolute value of the estimated momentum. The drift chamber hits in the shadowed area were used as seed points, starting from drift chamber four then drift chambers three, two and one. From the matched upstream x and y tracks

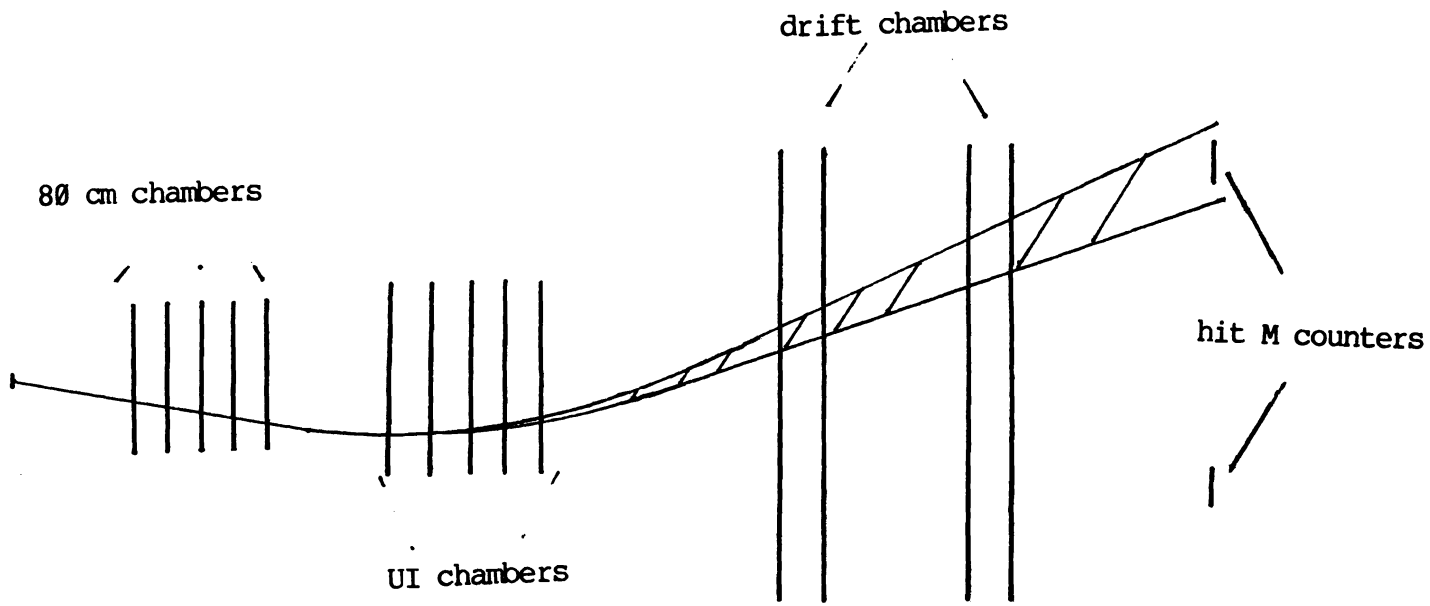

Figure 4.1

Illustration how the shadowed area in the drift chambers was determined from which the seed points were chosen.

and one of the seed point, an tentative track was formed and its cross points in the other chamber planes were predicted (the predicting scheme will be discussed later). Then the program searched through the planes to see if there were real hits near the predicted positions within a window (0.6 cm). After all the planes were searched, we counted the total number of planes in which hits were found and the total number of planes through which the tentative track passed. The maximum number of planes a track passed was 21, including two planes of the last 80 cm chamber, 15 UI chamber planes and 4 drift chambers. If the ratio of the first number over the second number was more than 60%, this track was considered as a muon in this stage of the analysis. The 60% requirement was a loose cut to insure that not too many useful events were thrown away.

Using this procedure, the upstream x slope of the track had to be found accurately, otherwise the predictions in drift chamber one and two would be off a little when the seed point was in drift chamber three or four. Some upstream track slopes were found with small errors, that degraded the predicting accuracy. In attempting to improve this, the upstream slope was adjusted slightly using the interaction vertex, the seed point and the hits found in drift chamber one and two, for three points could uniquely determine a track. The change of the upstream x slope was limited to 0.001. Some additional tracks were found in this way and the chi-squared of found tracks were reduced.

For each muon candidate in the y view, several upstream x tracks and more than one M counters could be used, and from each matched pair of x and y tracks several muon tracks could be found. A preliminary weeding was used to limit the total number of found muon tracks to six for a particular y-view muon candidate. Here the word "weeding" meant to get rid of the tracks that had the least chance to be real. If two found muon tracks shared a hit in the drift chambers or in u, v planes of UI chamber four and five, these two muon tracks were treated as one. Among them, the one which had more hits associated with it, or the one that had the least chi-squared when these two tracks had same number of hits, was saved. If more than six different muon tracks were found, only six of them were kept by the same criterion mentioned above using their associated hit numbers and the chi-squared.

After we had processed all the y-view muon candidates, muon pairs were formed. One positively charged muon and one negatively charged muon formed a dimuon pair. If there were one or more dimuon pairs in a event, this event was written to a dimuon tape (type 1), if the highest mass of the muon pairs was above 2.5 GeV, the event was written to a high mass tape (type 2). More complicated and time-consuming programs were applied to these reduced data samples.

Now going back to the predicting scheme, the basic ingredient was standard track technique, that is, the bending of the track from the straight line at each plane is proportional to the reciprocal of the track momentum. So from the bending of a standard track, we could

predict the bending of other tracks. But this simple idea was not good enough to be used directly, The magnetic field was not totally uniform and the tracks with different momenta and different incident angles passed different regions of the magnet, so the bending of these tracks were different. For example, if we predicted the hit position in drift chamber two from the seed point in drift chamber four, for certain tracks the predicted position was 2 cm away from the point where the track actually hit the chamber if the track was swum through the magnet. Here the word "swum" meant to trace the charged particles with known track parameters through the magnetic field according to the Maxwell's equations. The standard track method was not accurate enough to be used in the predicting program. It needed to be corrected.

In this analysis, a 15 GeV standard track parallel to the beam line was swum through the measured magnetic field, a set of bending at each plane was obtained as standard values, then tracks with a chosen set of different momenta and different incident angles were swum through the field, the differences of the bending between this method and the standard track method were obtained. These differences were fitted as polynomial functions of the momenta, the upstream x slopes and upstream y slopes of the tracks. The parameters in the fitting were used in the predicting scheme described below.

A modified predicting scheme could be expressed in the following formula:

```
P=-PMSTK(IDC)*XCO(IDC,PREC,SLX,SLY)*YFAC(SLY)/DEF(IDC)
```

Here P is the predicted track momentum;

IDC runs from 1 to 4 indicating which drift chamber is involved;

PMSTK is the deviation of standard track at drift chamber IDC;

PREC is the reciprocal of the absolute track momentum, it is calculated by standard track method;

SLX and SLY are the upstream x and y slopes;

DEF is the deviation of the predicted track at drift chamber IDC;

XCO and YFAC are correcting factors.

XCO and YFAC can be expressed as below:

```
YFAC=A(1)+A(2)*AY+A(3)*AY*AY+A(4)*AY*AY*AY+1
XCO(IDC)=1+P(1)+P(2)*XI+P(3)*XI*XI+P(4)*XI*XI*XI
P(J)=B(1)+B(2)*PREC+B(3)*PREC*PREC+B(4)*PREC*PREC*PREC
B(I,J,IDC)=F(I,J,IDC)
```

Here F(I,J,K) are fitting parameters mentioned above, I, J, IDC are from 1 to 4;

A(1) TO A(4) are fitting parameters also;

AY is the absolute value of SLY;

XI is SLX*Q, Q is the charge of the track;

From the sign of the track deviation at the seed point, we got the charge of the track. Using the standard track method, an estimated momentum was derived, PREC used in the above formula was the reciprocal of it. It was straight forward to calculate the positions of predicted hits in other drift chambers using the formulas above. For the predicting of hit positions in the UI chamber planes the standard track

method was used. At these chambers, the bending of the tracks was not as big as at the drift chambers, the deviation of the track position from the standard track prediction was not big enough to be corrected in the program.

Several things were checked to make sure that this predicting scheme was correct:

1. The tracks with momenta and slopes which were different from these used in determinating the polynomial parameters were swum through the magnetic field, their hit positions in the planes were compared with the positions predicted by the above scheme. The differences were typically less than 0.1 cm, the maximum values were about 0.3 cm. The prediction scheme worked quite well for tracks with either charges.

2. We applied this prediction scheme to the real data, the deviations of the positions of found hits from the predicted positions in each plane were histogramed, the peak value of the deviations was near 0 and the half width of the peak was typically 0.2 cm, no obvious difference was detected between positively charged track and negatively charged track. That was a reassurance that the magnetic field was measured quite well (except that the scale of the magnetic field could not be checked by this), also the result meant that the alignment program did the right thing. The deviation distributions were used to determine the window in each plane. the window was chosen to be 0.6 cm for all the UI planes and drift chambers. If a hit was found within 0.6 cm from the predicted position, the hit for a tentative track in

this plane was regarded as found.

4.4 Muon track fitting and weeding

When we wrote out the high mass dimuon tape, we made very loose cuts in the program. In this sample, the signal to background ratio in J/psi region was not very good. In order to get rid of some faked muons and therefore to enhance the J/psi signal, muon tracks were fitted and a weeding was applied to the muon tracks in these events.

A brief description is given below about the fitting and weeding program, a more detailed version is presented in the appendix.

A track was uniquely determined by five track parameters. They were the upstream x and y slopes, the intercepts of these two upstream tracks at z=Ø plane and the track momentum. Using all the hits associated with this track, these track parameters could be adjusted to values closer to the actual ones. A track with certain five parameters was swum through the magnetic field, at each plane the position at which the swum track passed was compared with the position of the associated hit of the track in this plane, a chi-squared was formed from these differences. The fitting minimized this chi-squared by adjusting five track parameters.

After the fitting, we were more sure about where the track passed in the apparatus. Based on this, several cuts were made to weed out the bogus muon tracks and as a result, the J/psi signal was enhanced. One cut was to tighten the window around the M and N counters to 2.5

cm. Another was to require more hits in each tracks. More than 70% of the predicted hits in the planes should be found. Now for most events only one pair of two oppositely charged muons existed. In the final dimuon mass plot, only one positively charged muon track and one negatively charged muon track of the best qualities were used to form the dimuon pair. The result will be shown in the next chapter.

To study the forward charge of the J/psi events, a program finding all the tracks of charged particles was developed (Appendix A). It was applied to all the events in which the dimuon mass was above 2.5 GeV. If the invariant mass of the dimuon pair was between 3.0 GeV and 3.2 GeV, this event was considered as a J/psi event. The events having the dimuon mass out of the J/psi region were treated as the background. Low momentum tracks were swept out of the chamber regions earlier than high momentum tracks, less planes could be used to find these tracks. That made the program less efficient for them. To correct the inefficiency of this trackfinding, a monte carlo program was run to find the trackfinding efficiencies for tracks with different momenta and different upstream incident angles (Appendix B). Figure 4.2 shows the efficiency of finding a track as a function of the rapidity and the transverse momentum of the track. These efficiency values were kept in a lookup table to be used in the forward charge calculation. The related results will be given in the next chapter also.

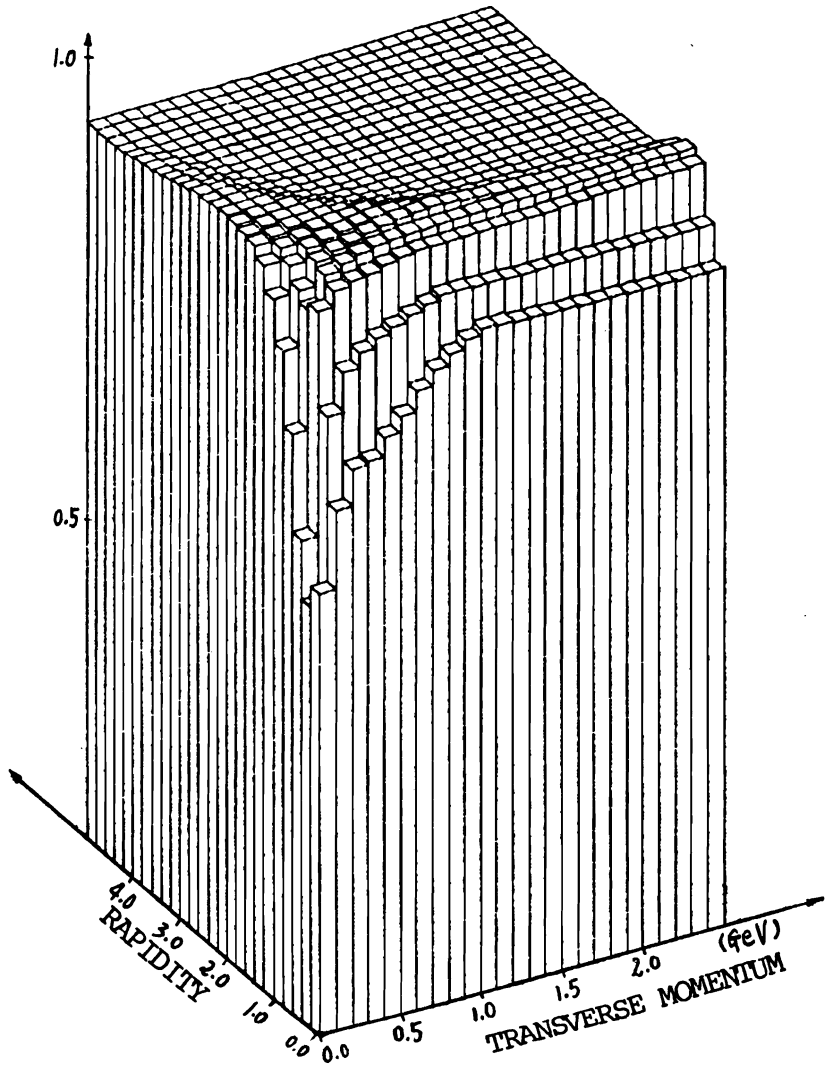

Figure 4.2

The track finding efficiency as a function of track rapidity and transverse momentum

CHAPTER 5 RESULTS AND DISCUSSION

The purpose of this analysis is to try to understand the hadronic production of the J/psi through the study of the associated forward charge flow. In this chapter, first the J/psi signals from π^-N and pN interactions will be presented. Then the following properties of the associated charged particles will be discussed: their rapidity distributions, the dependence of the forward charge on the Xf of J/psi particles, the charged multiplicity and the forward charge as functions of the effective energy of the forward hadron system.

The J/psi events will be compared with the events in inclusive hadronic interactions and with the events in the control region of the dimuon mass spectrum. The control region contained those events having the dimuon mass near the mass of J/psi but excluding the J/psi events. The omega signal and the properties of the associated forward charged particles will also be discussed. The forward charge properties of omega production will be compared with those of the inclusive interactions and of the J/psi production. Lastly I will discuss how this study could tell us about the mechanism of J/psi and omega production.

5.1 The J/psi signal

Figure 5.1 and Figure 5.2 show the resulting dimuon mass spectra for π^- and proton data respectively. We fitted each dimuon spectrum in the region of the dimuon mass above 2.5 GeV with a gaussian J/psi peak

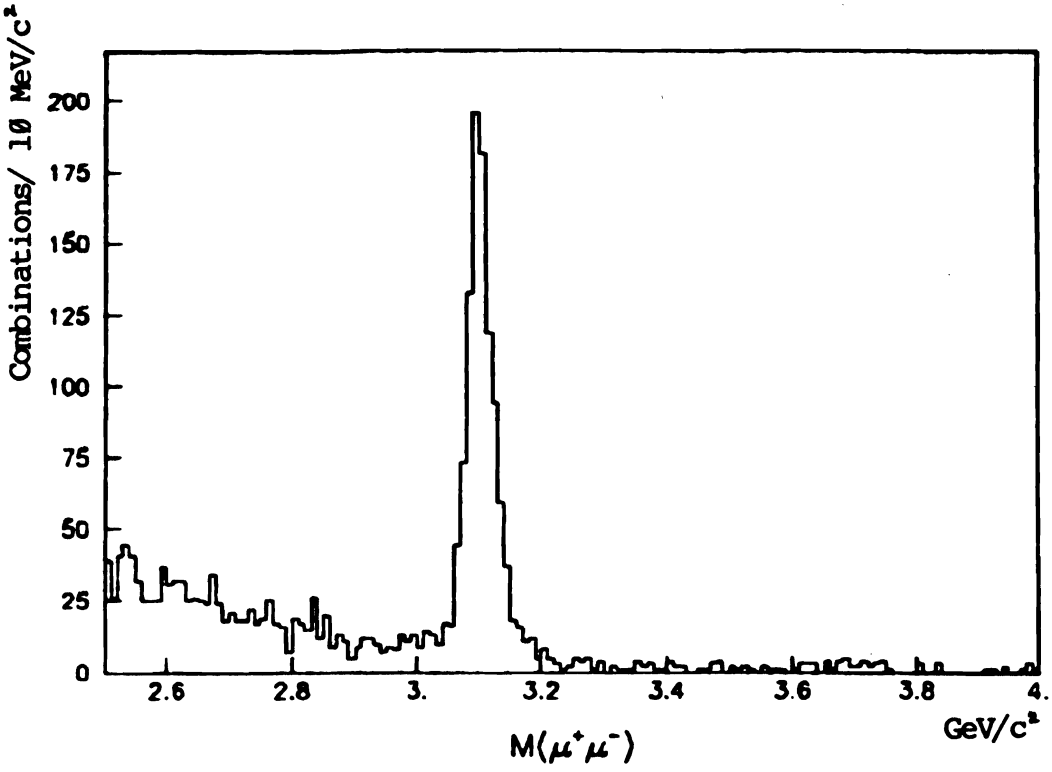

Figure 5.1

The dimuon mass spectrum for pion data

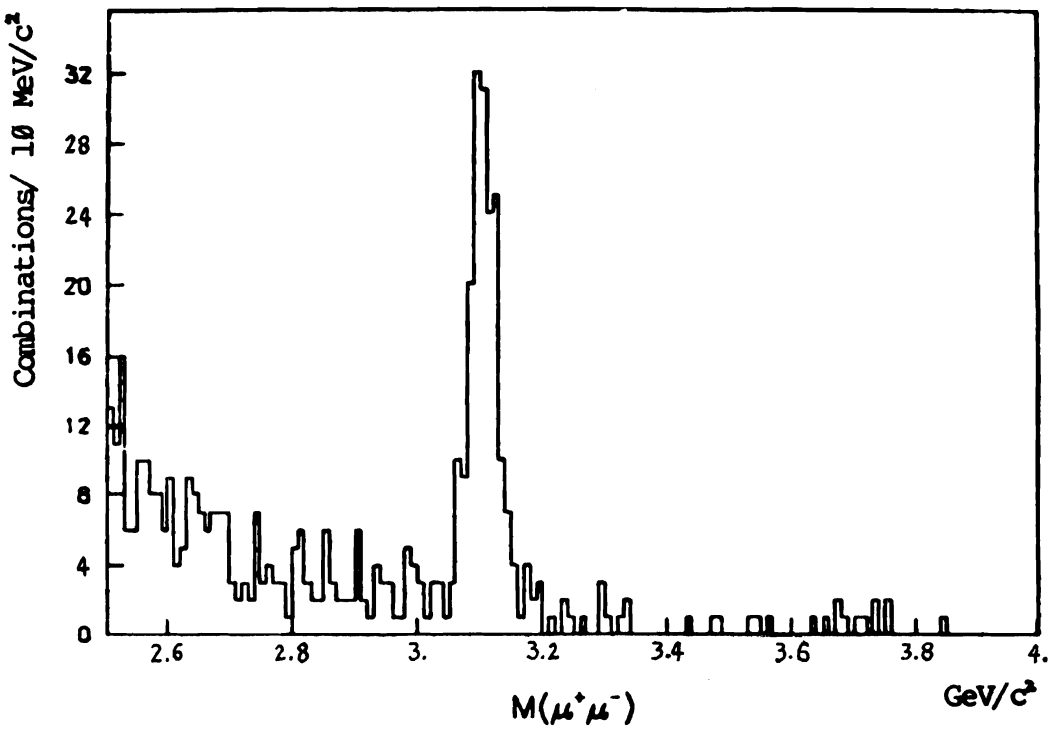

Figure 5.2

The dimuon mass spectrum for proton data

and an exponentially dropping background. The fitted parameters are as follows: the masses of the J/psi peak are 3.102+/-0.001 and 3.105+/-0.002 GeV/c^2, the standard deviations of the mass value (sigma) are 22.3+/-0.7 and 21.0+/-1.6 MeV/c^2, and the event numbers in the peak are 901+/-41 and 153+/-17. The background is mostly composed of the events having faked muons, which are the results of hadron punching through the absorbing steel, and of the events in which the muons are decay products of pions and kaons. Because there are more events in pion data, in the following we will mainly discuss the π^-N interactions and mention the pN interactions briefly.

Figure 5.3 is the Xf distribution of the J/psi signal in the CM system. Most of the J/psi were in the Xf region from 0.2 to 0.7, the drop of the signal at higher Xf was due to the small production cross-section, and the drop at low Xf was due to the small acceptance of our apparatus in this region. A monte-carlo study showed that our acceptance was very small near Xf=0.0, it rose to about 0.3 at Xf= 0.4, then slowly leveled off(Figure 5.4). If we assumed that the J/psi were produced by the fusion of one parton from the beam and one parton from the target, then we could calculate the Xf's of these two partons. As shown in Figure 5.5, the beam partons had large Xf values and the target partons had a very soft Xf distribution.

In the dimuon spectrum, we chose the events with the mass between 3.0 GeV/c^2 and 3.2 GeV/c^2 as the J/psi, and the other events with the mass above 2.6 GeV/c^2 as the control region. When the track finding

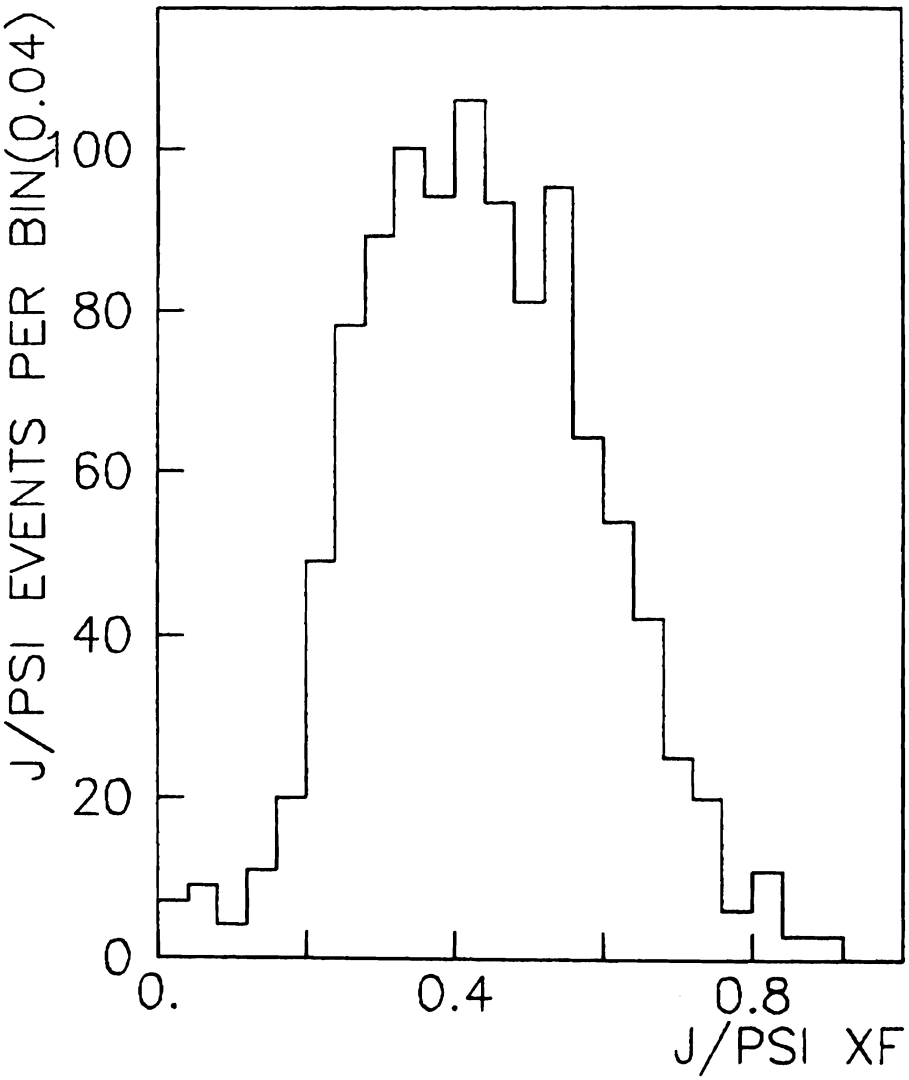

Figure 5.3

The Xf distribution of J/psi events in the raw data

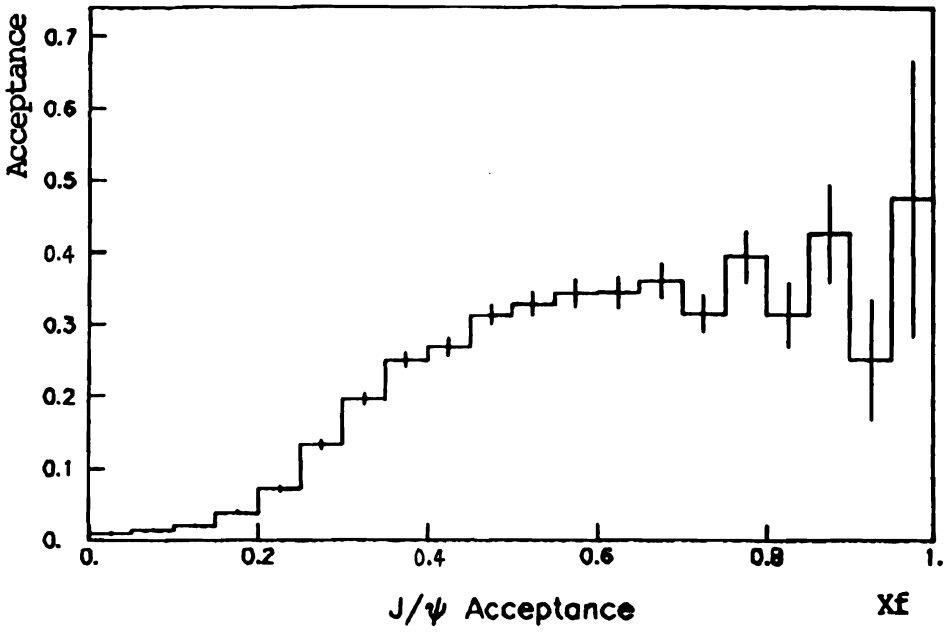

Figure 5.4

J/psi acceptance as a function of Xf

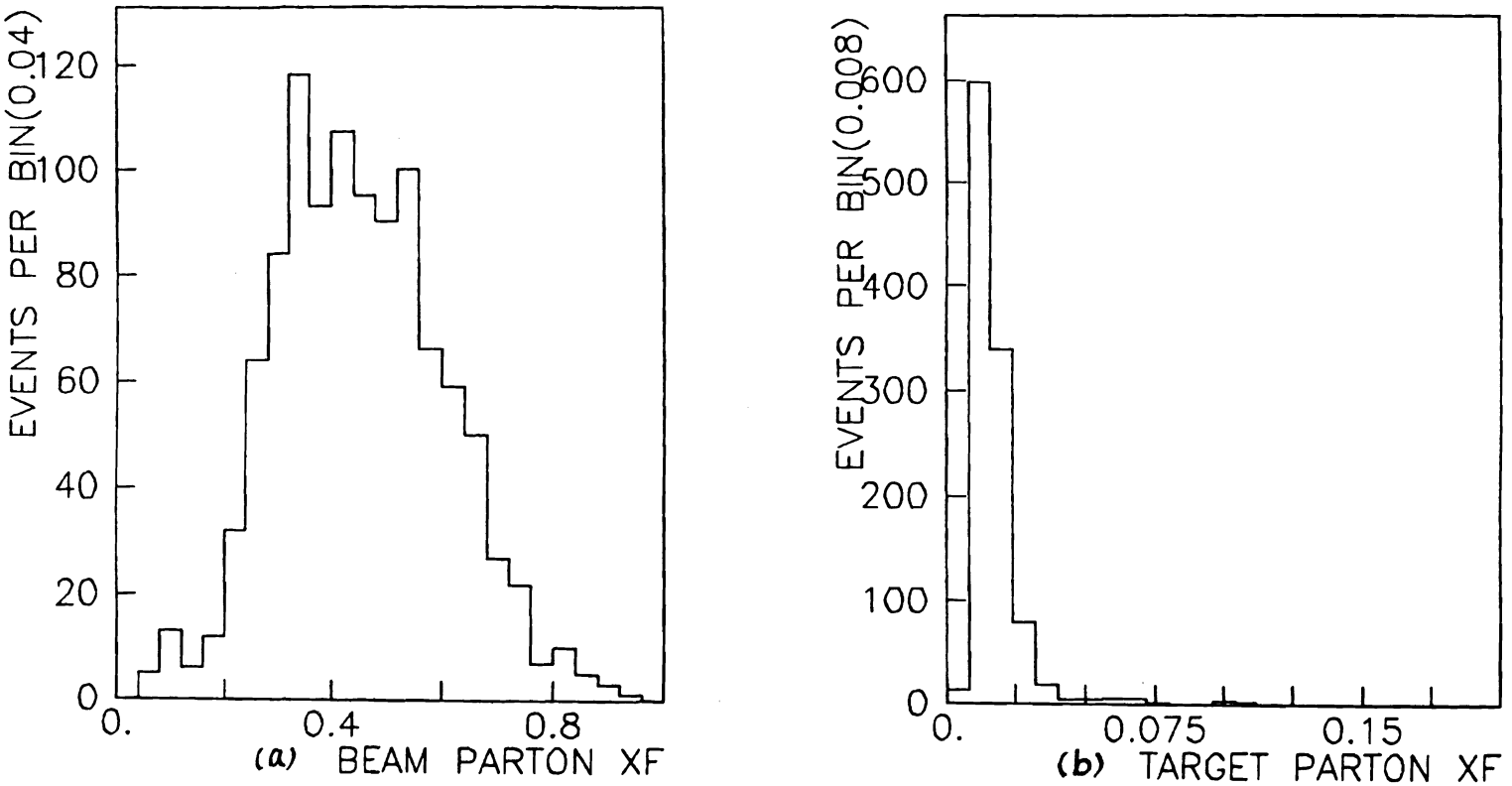

Figure 5.5

(a) Beam parton Xf distribution

(b) Target parton Xf distribution

program for all the charged tracks was developed, I found by looking at the graphics that certain events were very messy. The track finding program was not reliable for these messy events, it either missed some tracks or found false tracks. I excluded those events from the forward charge calculation if their total number of upstream x and y tracks exceeded 40. I also excluded those events in which apparently not all upstream x tracks were found. In the program, the number of upstream tracks found in x view was compared with the minimum number of hits in one plane out of four x-measuring planes. If the found track number was less than this minimum minus 2, the event was excluded from further analysis. I lost about 20% of the events by applying these cuts, but I felt that the result would be more believable. The same cuts were used in the monte-carlo program for deriving the trackfinding efficiency.

5.2 The rapidity distribution of the forward charge

To each remaining event, the program for finding all the tracks was applied, a detailed description of the program is in Appendix A. The forward charged multiplicity in each event was defined as the number of charged particles found in the forward hemisphere in the CM system, the two muons forming the J/psi or the background were not included. The average charged multiplicity was found to be about 3.4. This number was not corrected for the track finding efficiency.

Using the efficiency values in the lookup table in Appendix C, the finding efficiency for each track was determined by a extrapolation method after the track momentum and its upstream slopes were found. The efficiency values in the lookup table of those tracks, whose track parameters were neighbors of the ones of the track under study, were used in the extrapolation. Each track was assigned a weight factor, which was the reciprocal of the efficiency for this track. A weighted charge was defined as the multiplication of the track charge and this weight factor, the weighted charge had the charge sign of the track. This weighted charge was used in the forward charge calculation. It was not very meaningful for individual event to have a fractional charge, but for many events it could be used to correct the track finding efficiency statistically. Below the word 'charge' will always refer to this weighted charge unless its meaning is pointed out explicitly.

The quantity we were interested in was the forward charge sum of all the particles in the forward hemisphere in the CM. The particles were in the forward hemisphere if their rapidities in the CM were larger than Ø. To calculate the rapidities in the CM, the particle masses were needed. In our experiment, we did not have good particle identification besides muons. Instead all the charged particles were treated as pions except the two muons in each event. This simplification would shift the rapidity of a particle to a higher value if it was actually a kaon or a baryon. Some particles actually in the backward hemisphere would appear as in the forward hemisphere. The

forward charged multiplicity would be higher. On the other hand, most particles in the small rapidity region were pions[ref. 42], the systematic error of treating all the charged particles as pions should not be very big. In addition, when the forward charge flows in different processes were compared, this systematic error would be canceled out at some level.

The distribution of the forward charge sum for J/psi sample is shown in Figure 5.6. In this picture, the average forward charge is -Ø.46+/-Ø.Ø5. The error is statistical only, it equals to the standard deviation of the distribution over the square root of the event number in this picture. For the J/psi sample here, the standard deviation of the distribution is 1.34, the number of events is 8Ø6, so the error of the forward charge is about Ø.Ø5. The value of the forward charge in each event varies a lot from one event to the other. So there is no hope that we can learn much from the forward charge in each event. I tried to find out why for some events the absolute value of the forward charge could exceed four, but no sure answer. It is more meaningful to deal with the average forward charge for many events.

The rapidities of charged particles in all events were put into two histograms according to the charge sign. Figure 5.7 (a) and (b) show the normalized rapidity distributions of positively charged particles and negatively charged particles. The drop of the distributions in the negative rapidity region was due to the poor acceptance of our apparatus. Looking at these pictures, the associated

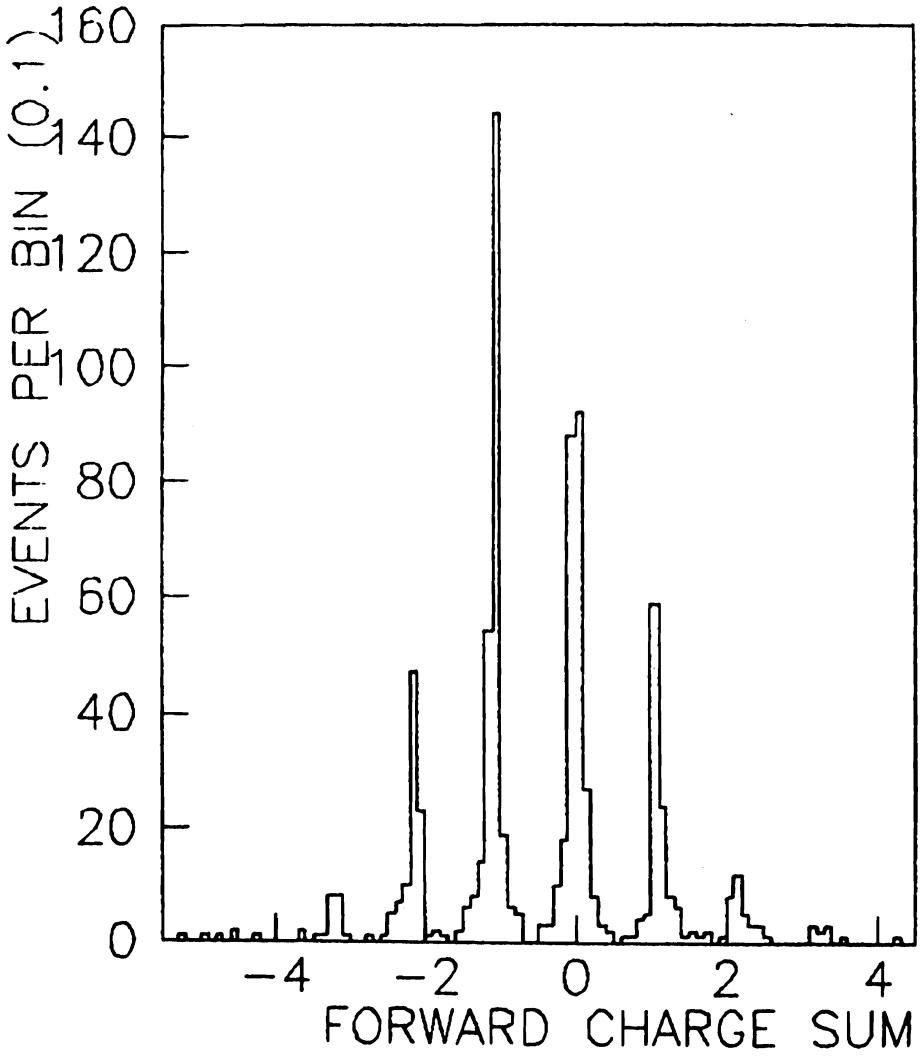

Figure 5.6

The distribution of forward charge sum in each event

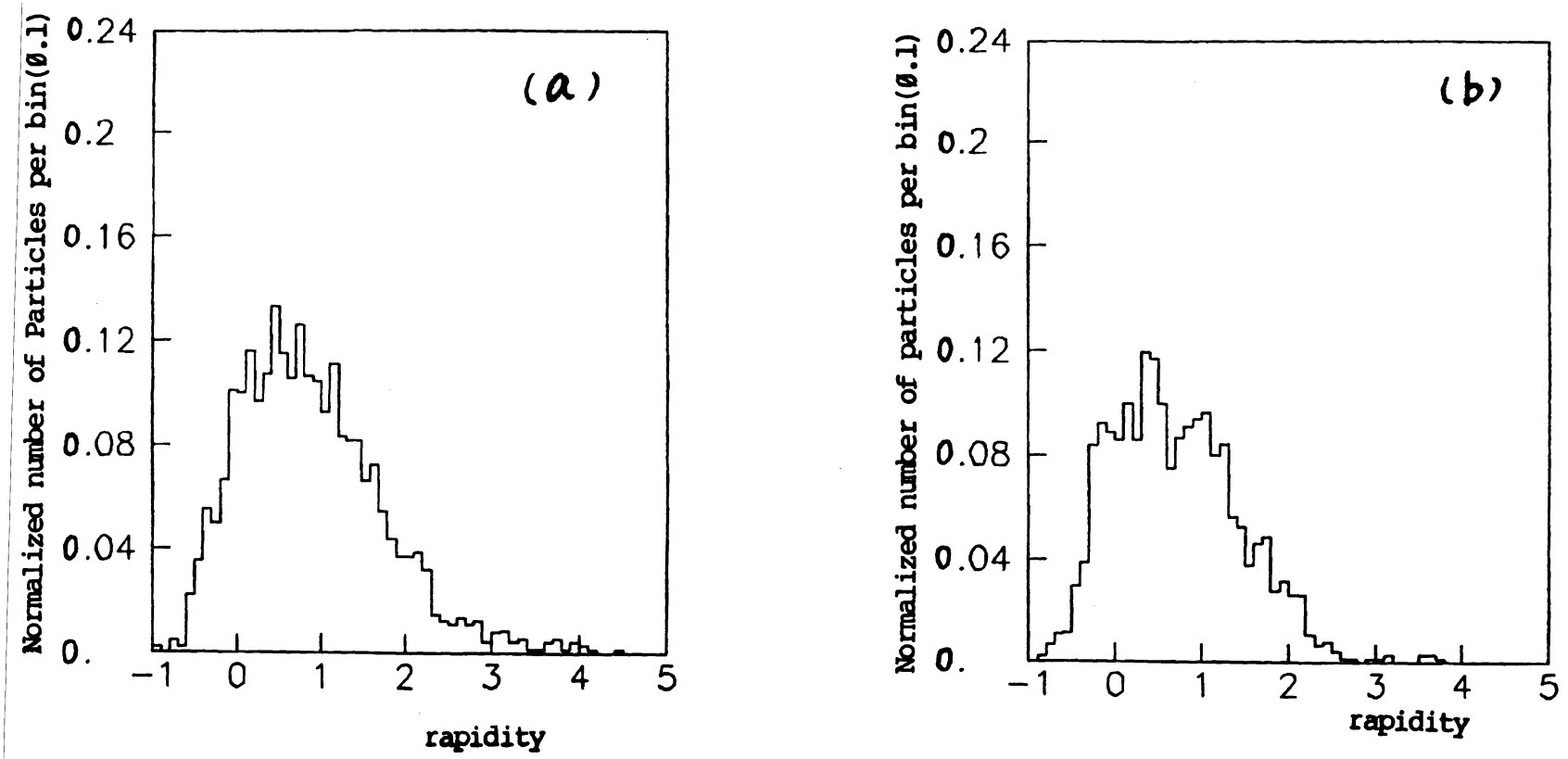

Figure 5.7

(a) Rapidity distribution of negatively charged particles of J/psi

(b) Rapidity distribution of positively charged particles of J/psi

charged particles were populated in the small rapidity region (y<3). The charge density near y=Ø was quite flat. The net charge rapidity distribution is shown in Figure 5.8, it is the subtraction of the two distributions in Figure 5.7. Figure 5.9 shows the integrated charge rapidity distribution starting from y=Ø. The total forward charge per event was about -Ø.46 as obtained before.

The same process was applied to the events in control region and to the events in inclusive interactions. Figure 5.1Ø and Figure 5.11 are the integrated charge rapidity distributions for these two kinds of data. The total forward charges for them were -Ø.6Ø+/-Ø.Ø5 and -Ø.654+/-Ø.Ø23 respectively. The statistic error was calculated as in the J/psi case. If we compare these distributions closely, we can see that the slopes of the last two distributions are almost the same, but the slope for J/psi events is not as steep as the other two. This means that the absolute value of the net charge density in J/psi events is smaller than those in the other two processes.

We did not have clean Drell-Yan events so we could not find out what was the forward charge of Drell-Yan production. We had to rely on other experiments for this information. WAll experiment found that the integrated forward charge was -.36+/-Ø.Ø5, -Ø.6Ø+/-Ø.Ø8 and -Ø.76+/-Ø.1 for the Drell-Yan process, the J/psi production and in the inclusive interactions. They assumed that the charge leakage between the forward and backward hemispheres was proportional to the forward charge, after they normalized the forward charge for π^-Be interactions to -1.Ø, the

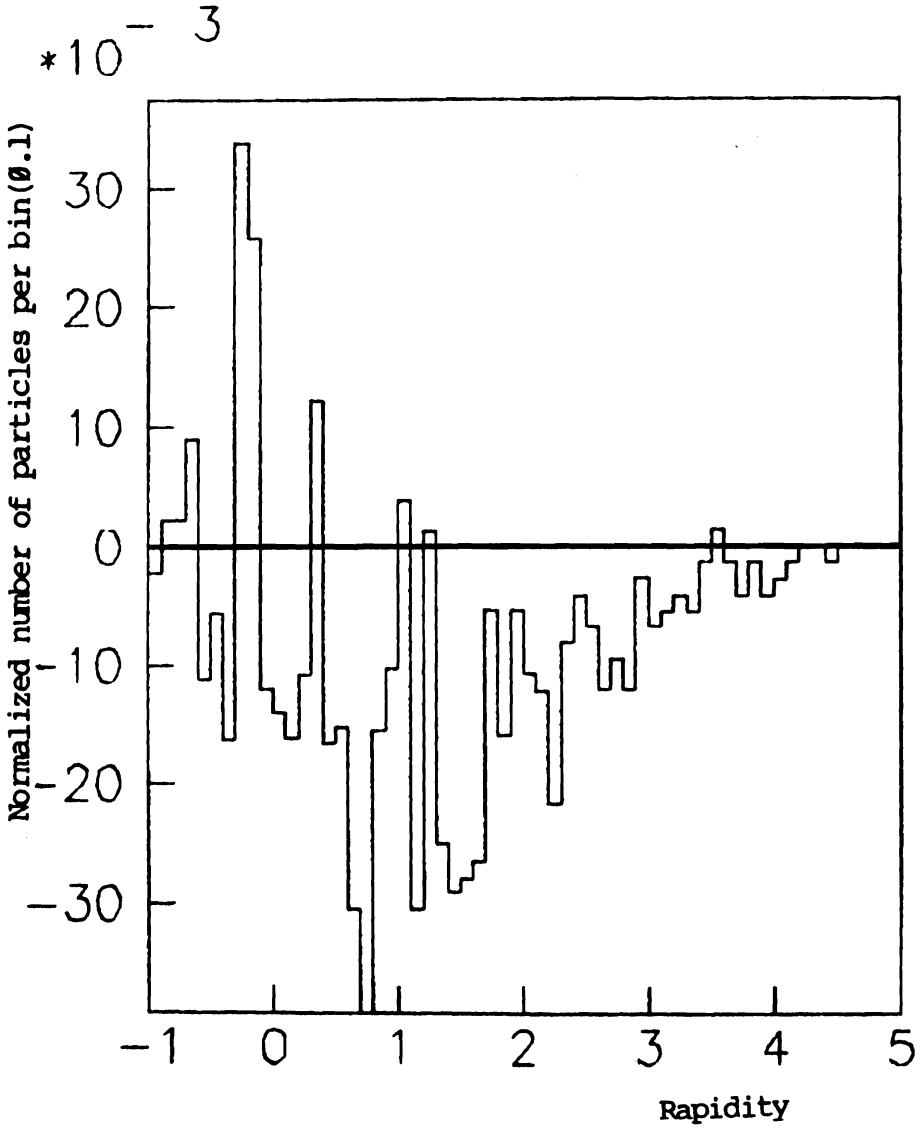

Figure 5.8

Rapidity distribution of forward charge of J/psi

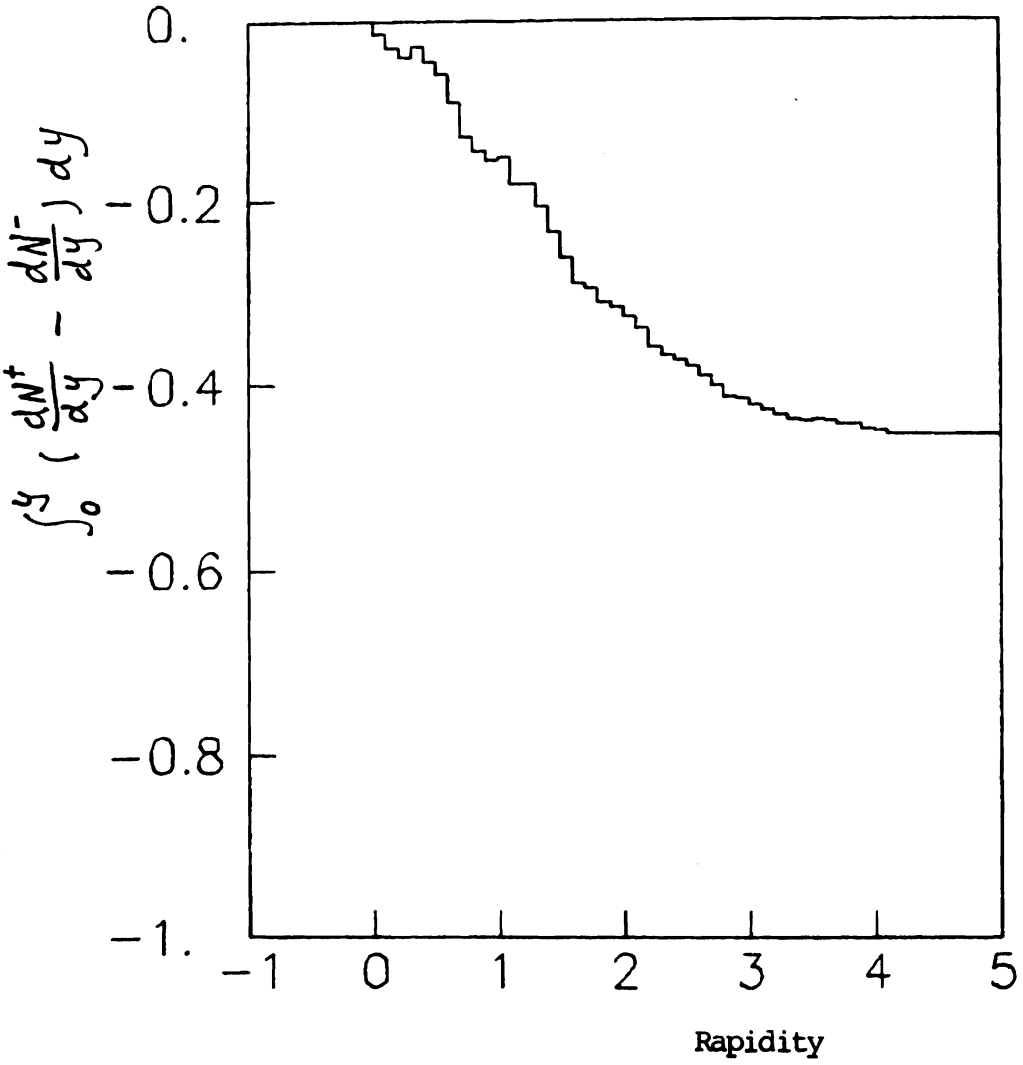

Figure 5.9

Rapidity distribution of integrated forward charge of J/psi

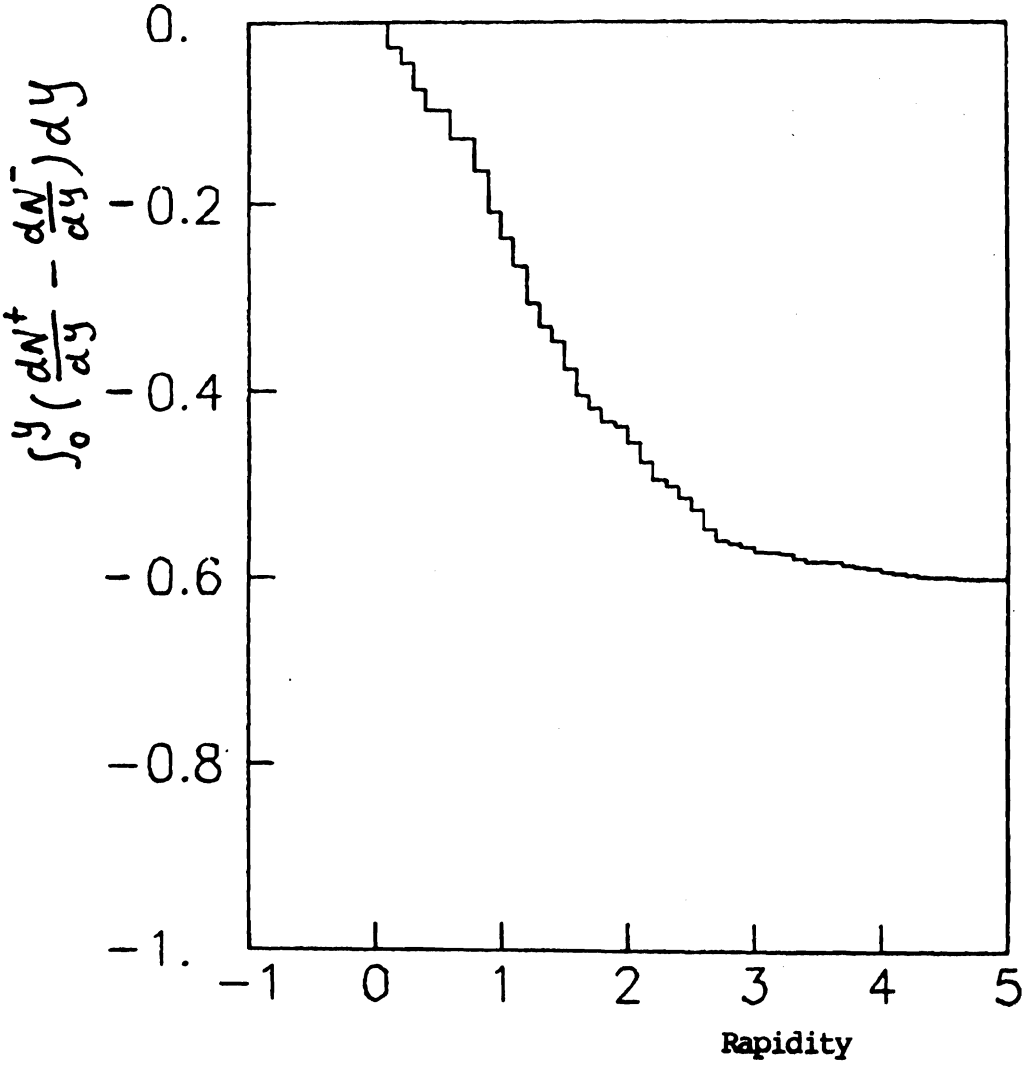

Figure 5.10

Rapidity distribution of integrated forward charge of background events

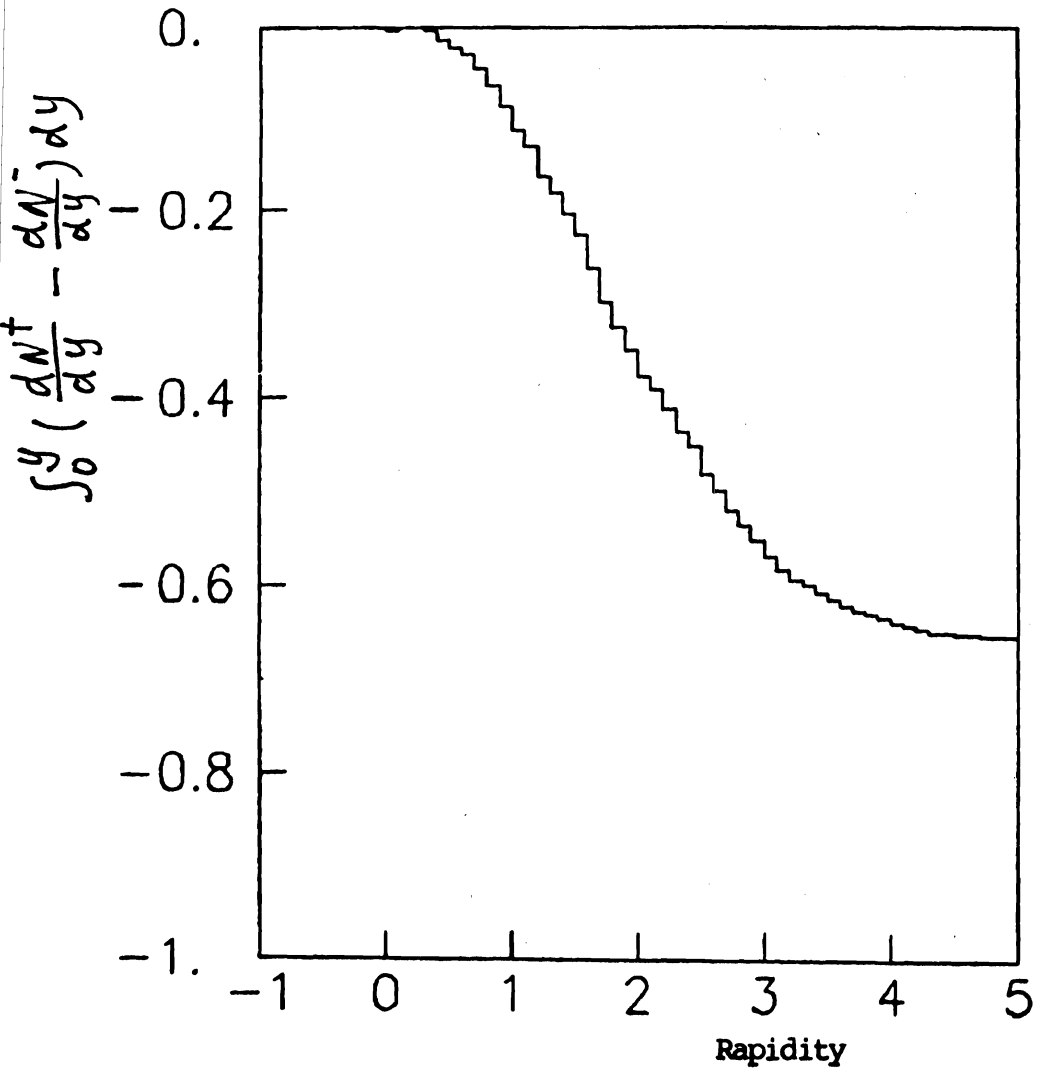

Figure 5.11

Rapidity distribution of integrated forward charge

in inclusive interaction

forward charge was -Ø.47+/-Ø.Ø5 and -Ø.79+/-Ø.Ø8 for Drell-Yan and J/psi production. By assuming a simple model that J/psi was produced by quark fusion and gluon fusion, and that the forward charge in quark fusion was the same as in the Drell-Yan process and the forward charge in gluon fusion was the same as in inclusive interactions, they concluded that the fraction of J/psi produced through quark fusion was about 4Ø% in their data. If we follow their assumptions, after we have normalized the forward charge in the inclusive interactions to -1.Ø, the forward charge for J/psi production is -Ø.71+/-Ø.Ø8. If we assume that the forward charge for Drell-Yan production is -Ø.4 as the Field-Feynman fragmentation model predicted, the fraction of the J/psi production through quark fusion would be about 48%. This conclusion may be too naive, but the forward charge is somewhat different between the J/psi production events and the events in the inclusive interations.

5.3 forward charge as a function of J/psi Xf

The above discussion treated the forward charge on a global basis. As argued in Chapter 2, the forward charge as a function of J/psi Xf may tell us more about the production mechanism.

The Xf distribution of the J/psi in our data was shown in Figure 5.1, we divided the whole sample into four subsets according to the Xf value. The means of Xf and the forward charge for the events in each subset were calculated. Figure 5.12 shows the forward charge as a function of Xf of J/psi particles. It is different from a similar plot

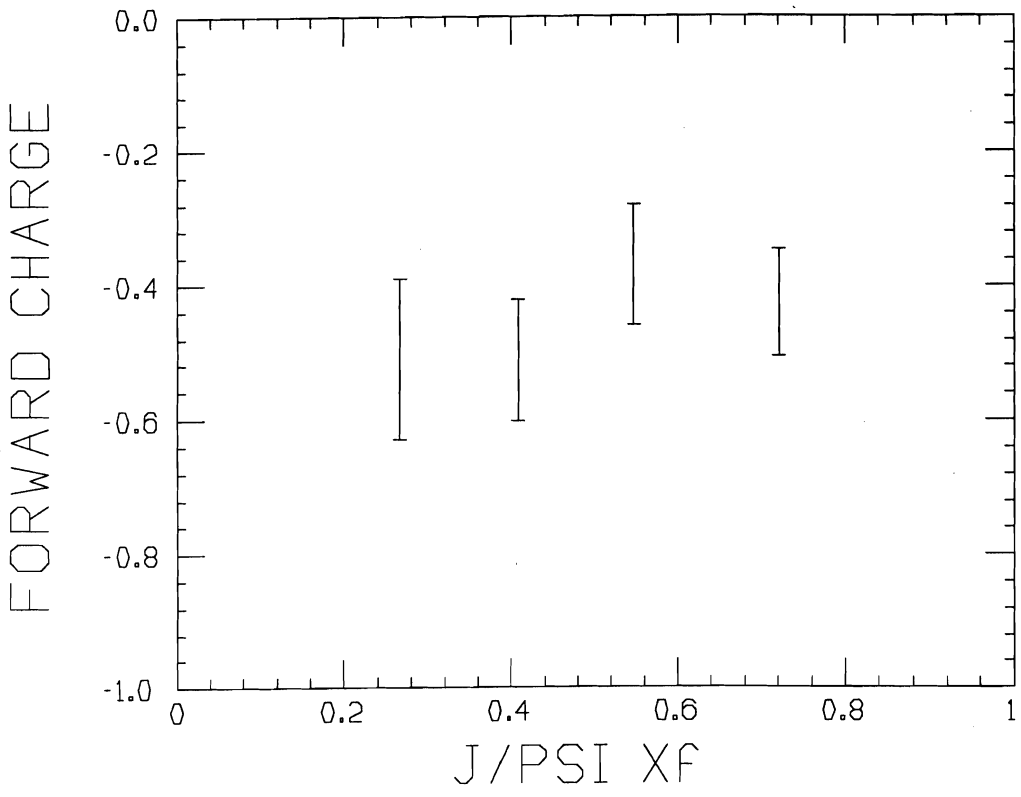

Figure 5.12

Forward charge as a function of Xf of J/psi

for the events in the control region as shown in Figure 5.13. That is the evidence that the curve in Figure 5.12 is not just due to kinematic effects. In these two and the similar figures that will be shown later, the statistical error of the forward charge for each point is calculated in the same way as the one for calculating the forward charge error in Figure 5.6. Basically the larger error of a point means there are fewer events included in this point. This Xf distribution is consistent with the prediction of the simple parton fusion model to some degree. The prediction of the model was that the forward charge would become less negative as the Xf value of the J/psi increased. Our data is more or less consistent with the prediction except that the third point from the left in the plot is a little above the fourth point. Because of our poor statistics, we could not make the conclusion that our data agrees with the simple model very well.

One motivation for this forward charge study came from H. Budd's result[ref. 30] in the study of associated forward charge of J/psi production. He claimed that the forward charge as a function of Xf was not consistent with the parton fusion model. We quote his result in Figure 5.14 along with the data points of this analysis. The shadowed area in the plot represents the region in which the predicted forward charge from naive fusion model should be. Three curves in the plot correspond to his three different assumptions for the forward charge in the pion valence quark fusion. Two of his data points at low Xf differed from the prediction by about two standard deviations. The difference between the data points of this analysis and the prediction

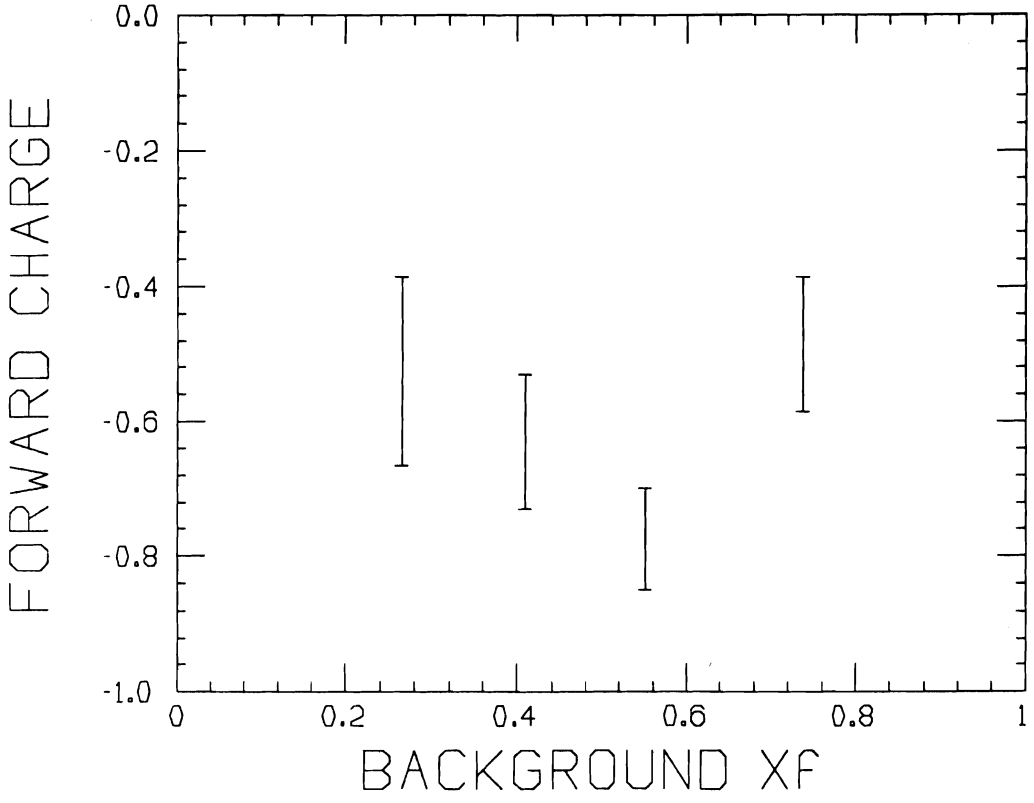

Figure 5.13

Forward charge as a function of Xf of the events in the control region

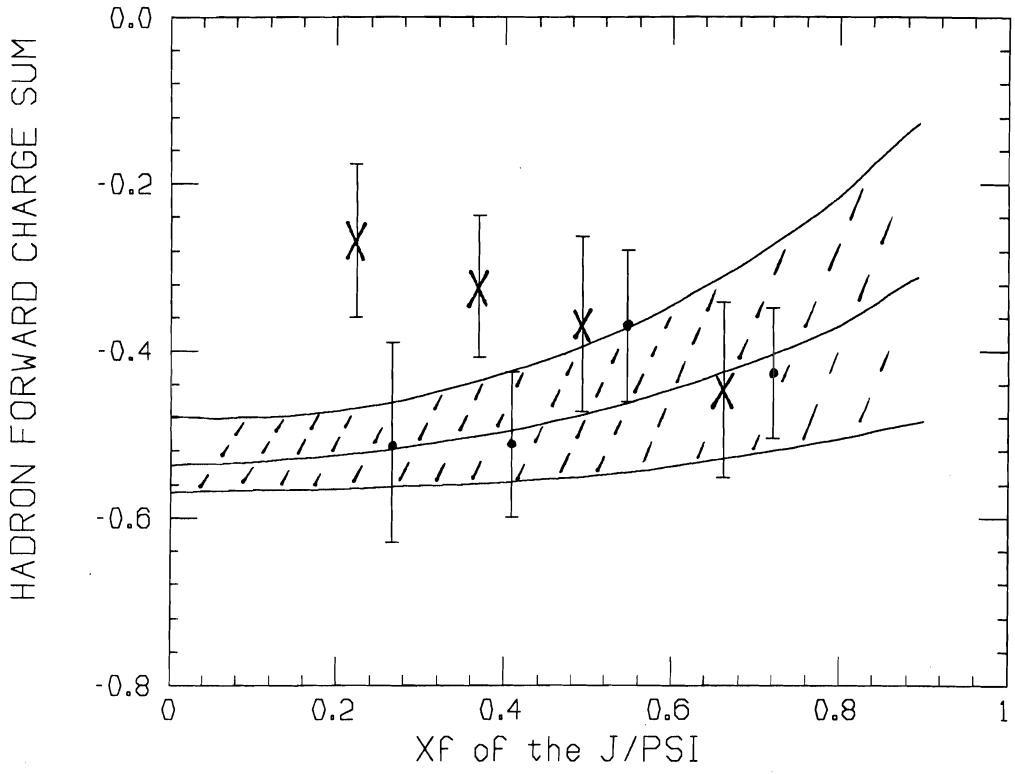

Figure 5.14
Comparison of forward charge as a function of Xf of the J/psi
the shadowed region is predicted using the model in reference 30
the x's are data points from reference 30
the dots are data points in this analysis

is much smaller. Our result is consistent with his naive model. Because both data had large statistic errors, it is hard to judge if the difference between these two data sets was just statistical fluctuation or was because that some systematic error in one data analysis was not taken into account.

5.4 Dependence of fragmentation on effective energy

Now we discuss how the fragmentation of the forward hadron system depends on its effective energy. Here we focuss our attention on the forward charged multiplicity and the forward charge as functions of the effective energy of the forward hadron system. The effective energy was defined as $\sqrt{s}/2-E_\psi$, here $\sqrt{s}$ is the total energy in the CM of the interactions. In 185 GeV/c π^-N interactions, $\sqrt{s}$ is 18.65 GeV. E_ψ is the energy of produced J/psi or background dimuon pair. It may make more sense if we define the effective energy as $\sqrt{s}(1-x1)/2$, which equals to the energy carried by the beam parton spectator. This spectator fragments into the forward hadron system if the interacting parton and the spectating partons are acting independently in the interactions. But the difference between the above two definitions is not very big because most of the J/psi energy comes from the beam parton.

The data were divided into several subsets according to the effective energy. For the events in each subset, we calculated the means of the charged multiplicity and the effective energy. Figure 5.15 shows the charged multiplicity as a function of the effective

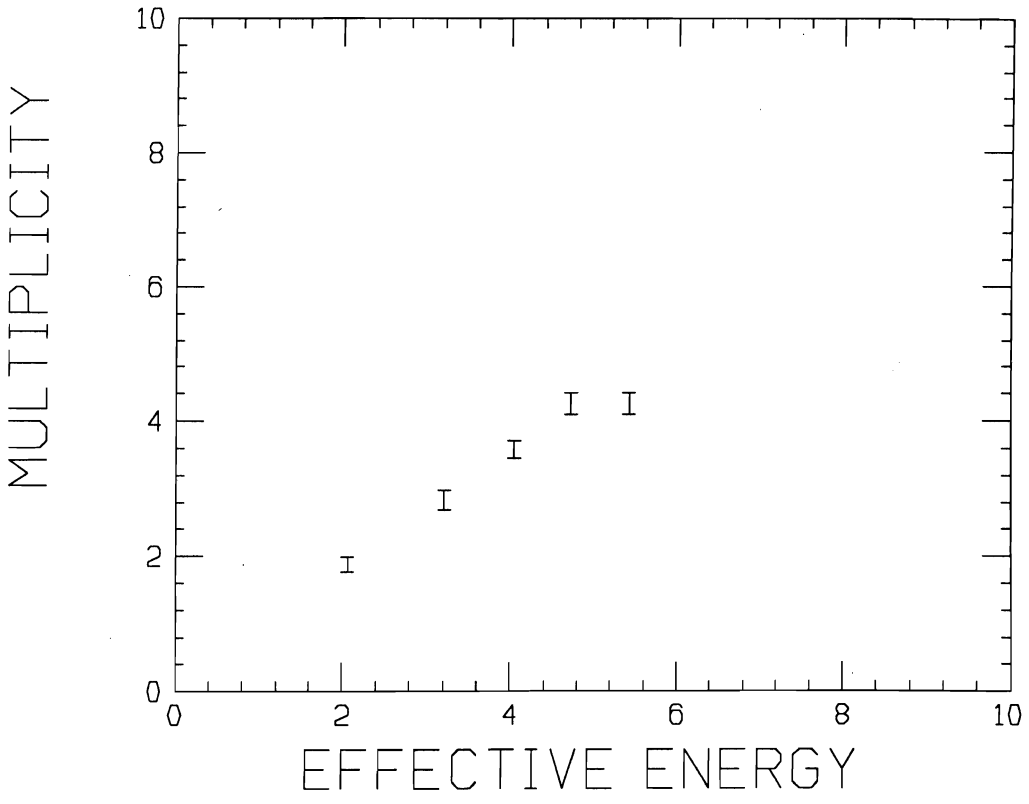

Figure 5.15

Multiplicity as a function of effective energy of associated forward hadrons in J/psi events

energy for J/psi events. If we draw a curve through the data points in the picture, the shape of this curve agrees with the shape of the curve in Figure 2.8. For forward charged multiplicity, the curve in figure 2.8 should divided by two. This supports our assumption that the fragmentation of forward quark or diquark depends on the effective energy of that system. Most of the points in Figure 5.15 are above the curve in Figure 2.8 divided by 2, this may be mostly because our trigger was slightly biased toward accepting high multiplicity events. Figure 5.16 shows the ratio of the dispersion of the multiplicity distribution over the average number of charged particles in each subset, or D/N as used in some papers, as a function of the effective energy. Looking at this picture, we can say that at high effective energy the D/N values agree with that in inclusive hadronic interactions, i.e, about Ø.5, but at low effective energy the dispersion is somewhat larger than that in inclusive hadronic interactions. This may hint that the fragmentation is a little different at low effective energy than at higher effective energy, because not enough energy is available for fragmentation when the effective energy is small. When we look at the forward charge as a function of effective energy, the points at small effective energy may not be very meaningful. Figure 5.17 shows the forward charge as a function of the effective energy, most of the points are above the curve for inclusive interactions, including the points having large effective energy. Large effective energy corresponds to small CM energy of the J/psi particles, or small value of Xf. Most simple

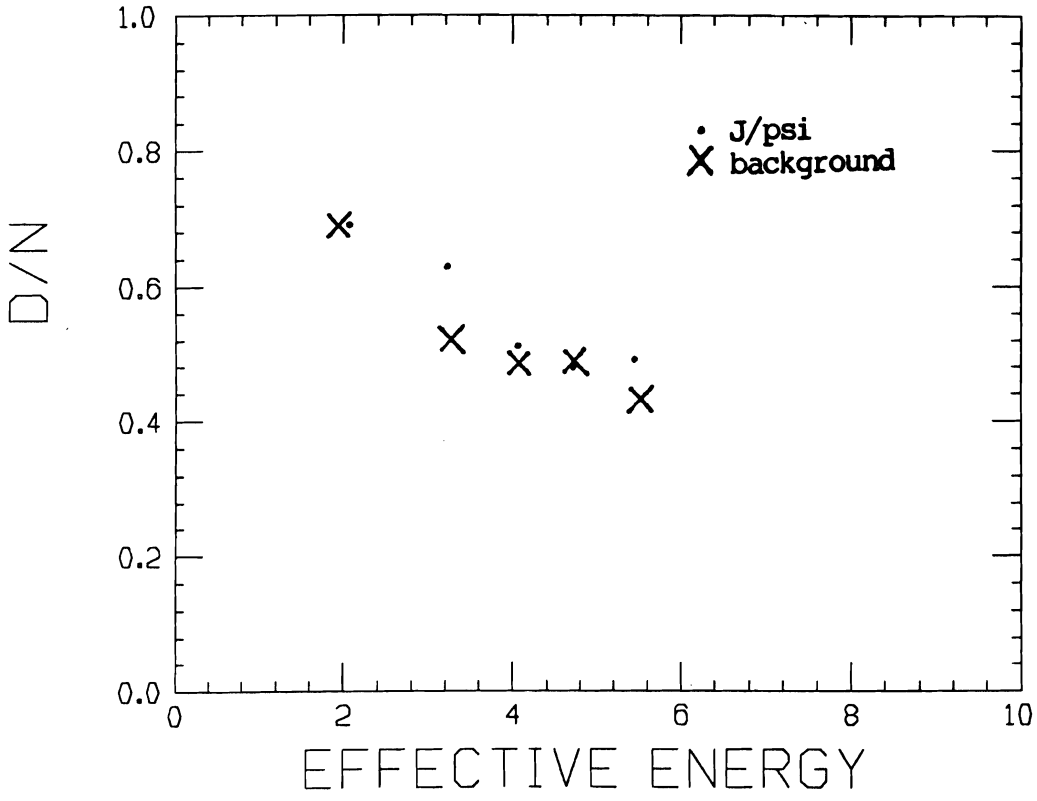

Figure 5.16

Ratio of dispersion over multiplicity as

a function of effective energy of associated hadrons

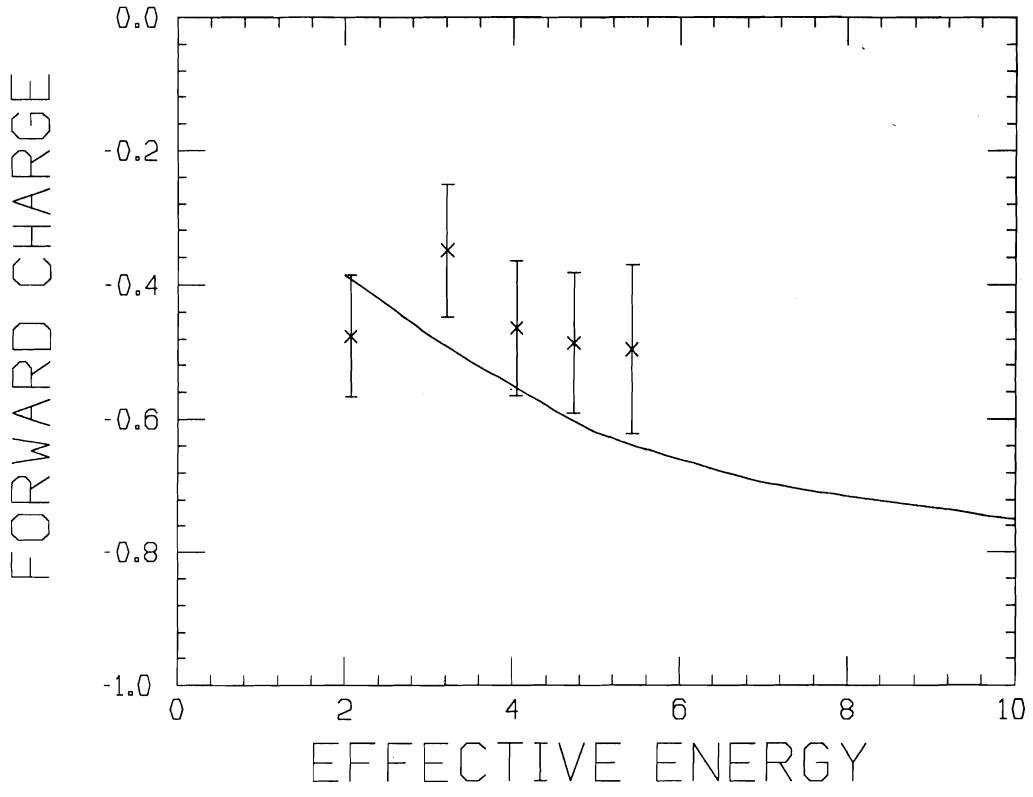

Figure 5.17

Forward charge as a function of effective energy of associated forward hadron system in J/psi events. The curve is converted from Figure 2.7

fusion models predict that gluon fusion would dominate the production, here from our data the quark fusion seems to contribute more than expected at high effective energy. Unfortunately we did not have large number of events especially we did not have enough events at high effective energy, otherwise we might be able to tell if the difference persists at higher effective energy and to assess the difference in a more quantitatively manner.

We have a good sample of omega events, it is worth while to see what is the result if we apply the same analysis to this omega data sample.

5.5 Forward charge analysis for omegas

James Bellinger worked on the Xf and Pt distribution of omega particles. His analysis concluded that a range of 0.60 to 0.80 of omegas were produced through gluon fusion depending on different parton distribution functions used as input and the rest of omegas through quark fusion in the simple parton fusion model[ref. 43]. I used his data sample with the dimuon mass below 1 GeV, which was subtracted from about two thirds of the π^-N dimuon data. The spectrum of the dimuon mass below 1 GeV is shown in Figure 5.18. A clear omega signal could be seen. I applied the same analysis to this data sample as to the J/psi data. Some complications arose for the omega data, the ratio of the signal to the background is less than 1:1 which is much smaller than the ratio for J/psi events. A broader rho peak is below the omega peak, that makes the background subtraction more difficult. We had to

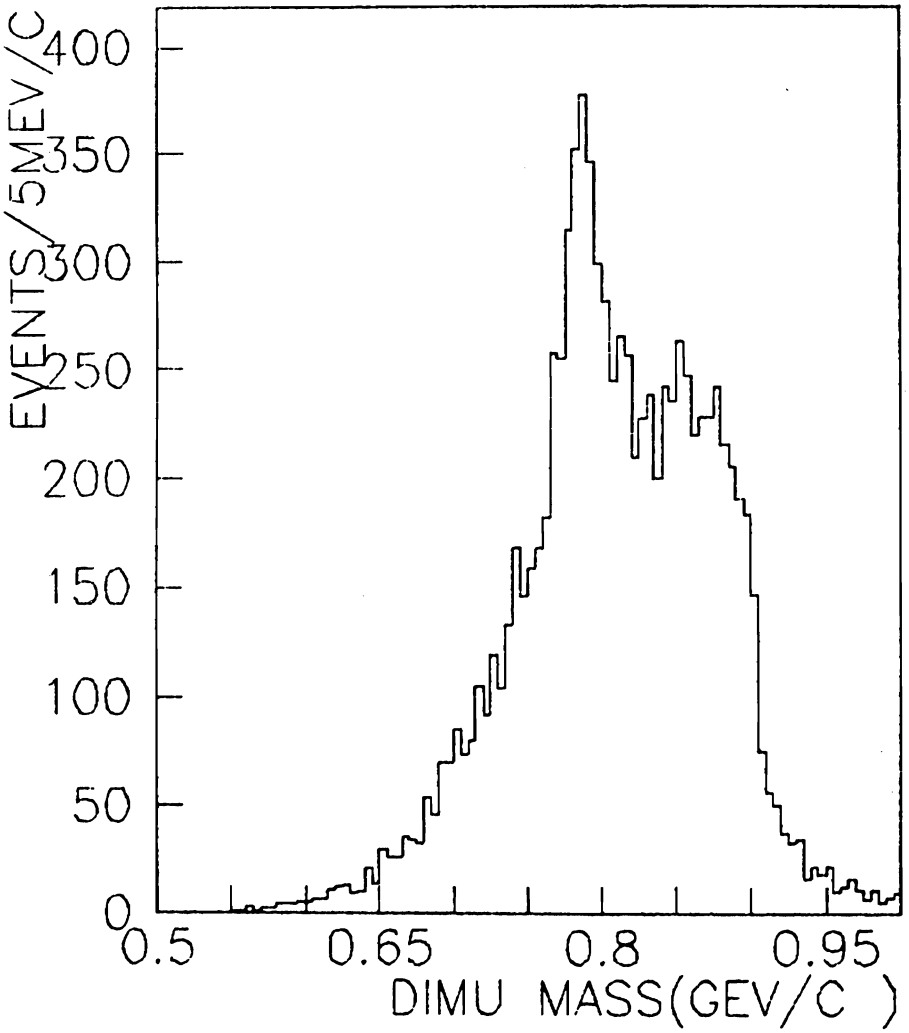

Figure 5.18

Dimuon mass spectrum from Ø.5 GeV/c to 1 GeV/c

treat the background with care. Because the full width of the rho peak is more than 150 MeV, we chose a narrow mass window as the omega signal to minimize the rho contribution. Here we define the region of the dimuon mass between 0.765 to 0.805 GeV as omega bin. In this omega region, we assume the background linear. By counting the events in the omega bin and the events in the neighboring mass regions, we derived the number of omega as 1040, the number of background events under omega peak was 1439. The error of these two numbers is estimated to be less than 100. The events above 0.6 GeV and below 0.9 GeV in the spectrum except the omega region were chosen as background sample.

To subtract the background contribution, a physical quantity for omega is calculated using the following formula.

$$A(\omega)=(A(\omega B)*NUM(\omega B)-A(BACK)*NUM(BACK))/(NUM(\omega B)-NUM(BACK))$$

Here NUM(ωB) is the total number of events in the omega bin(2479).

NUM(BACK) is the estimated number of background events in the omega bin(1439).

A(ω), A(ωB) and A(BACK) are the same physical quantities for omega, omega bin and background events.

The following are the results of the forward charge study for the omega data. Figure 5.19 shows the integrated forward charge as a function of the rapidity. The total forward charge equals to -0.66+/-0.04, and is quite close to the forward charge -0.654 in the inclusive interactions. The slope of the curve is almost equal to that

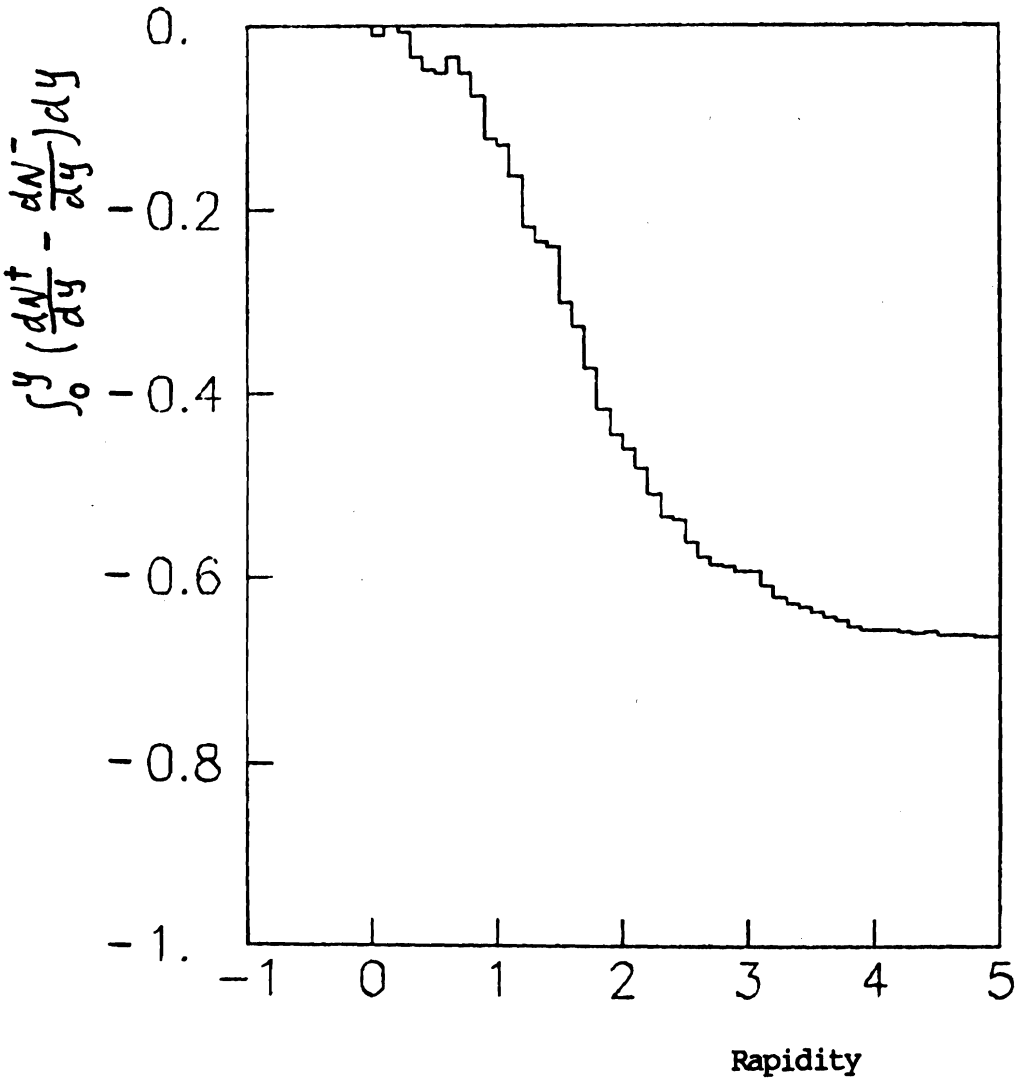

Figure 5.19

Rapidity distribution of integrated forward charge of omega

in the inclusive interactions. Some conclusions could be drawn from this. The mechanism for the omega production may be different from that for the J/psi production. It is consistent with most of the omegas being produced through gluon fusion in the simple parton fusion model.

Figure 5.20 shows the forward charge as a function of the omega Xf. The forward charge becomes less negative as the Xf of omega increases, as the simple fusion model predicted. It is not quite the same as the one for the J/psi events. The points of omega production are more negative than the ones of the J/psi production.

Figure 5.21 and Figure 5.22 show the multiplicity and the forward charge as functions of the effective energy of the forward hadron system in omega production. The curve of the forward charge as a function of the effective energy is consistent with the one for interaction events.

5.6 Proton data

Because the limited number of J/psi events in the pBe interactions, we will show the integrated forward charge distribution only. Figure 5.23 is this distribution for J/psi events. As a comparison, Figure 5.24 is the integrated forward charge in inclusive pBe interactions. The forward charge for these two cases is 0.73+/-0.03 and 0.71+/-0.11 respectively. The slopes of the curves in these two distributions are consistent with being equal. The naive

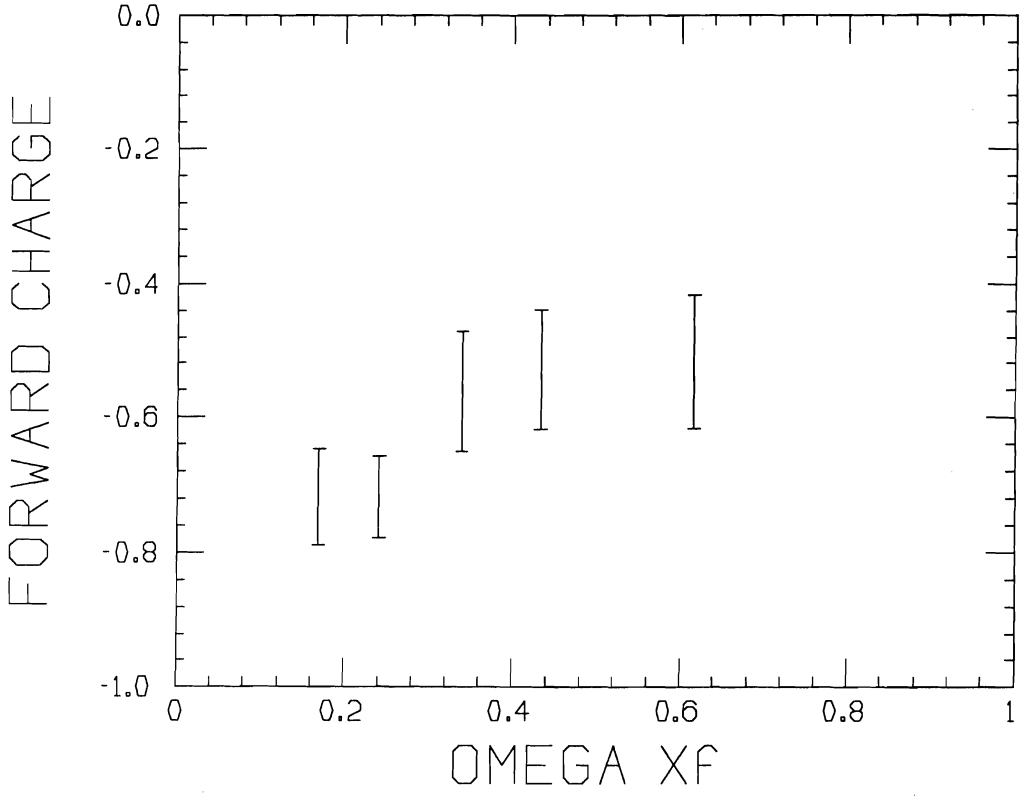

Figure 5.20

Forward charge as a function of Xf of omega

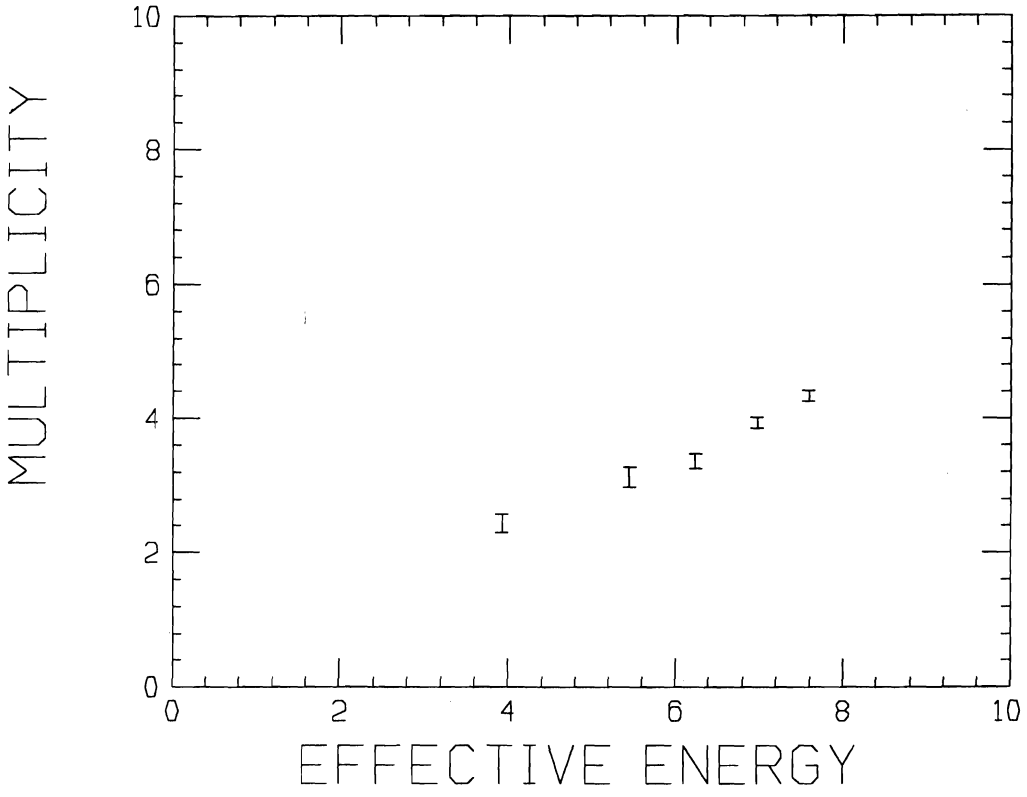

Figure 5.21

Multiplicity as a function of effective energy of associated forward hadron system in omega events

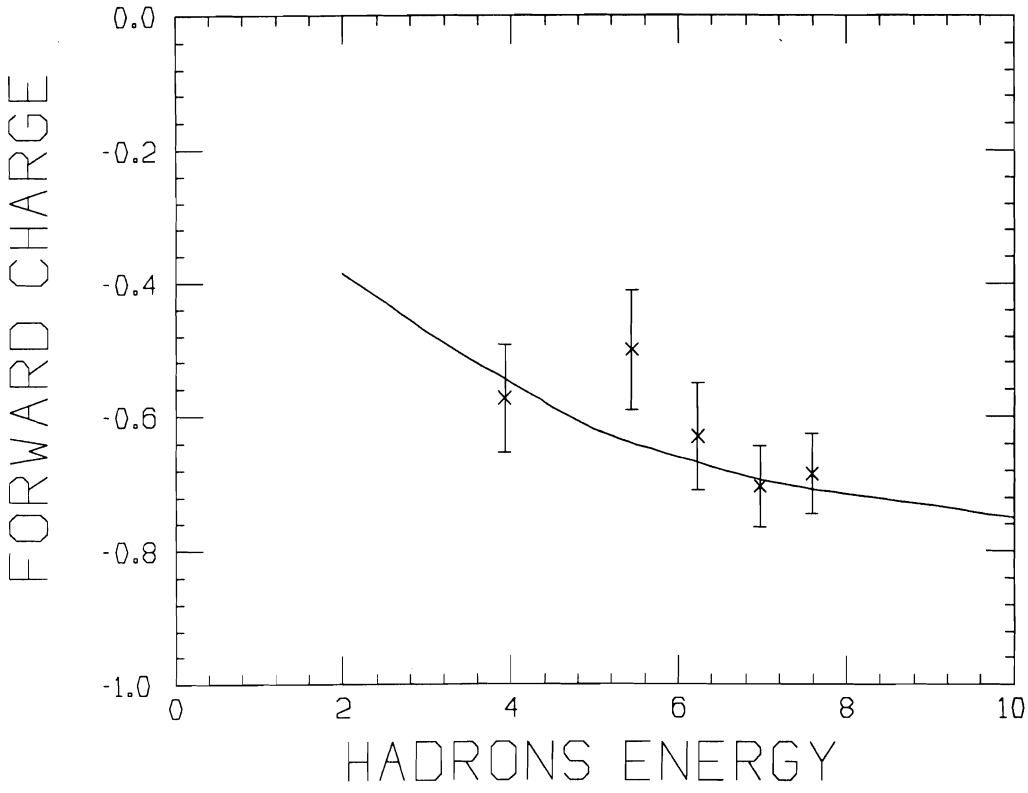

Figure 5.22

Forward charge as a function of effective energy of associated forward hadron system in omega events.

The curve is converted from Figure 2.7

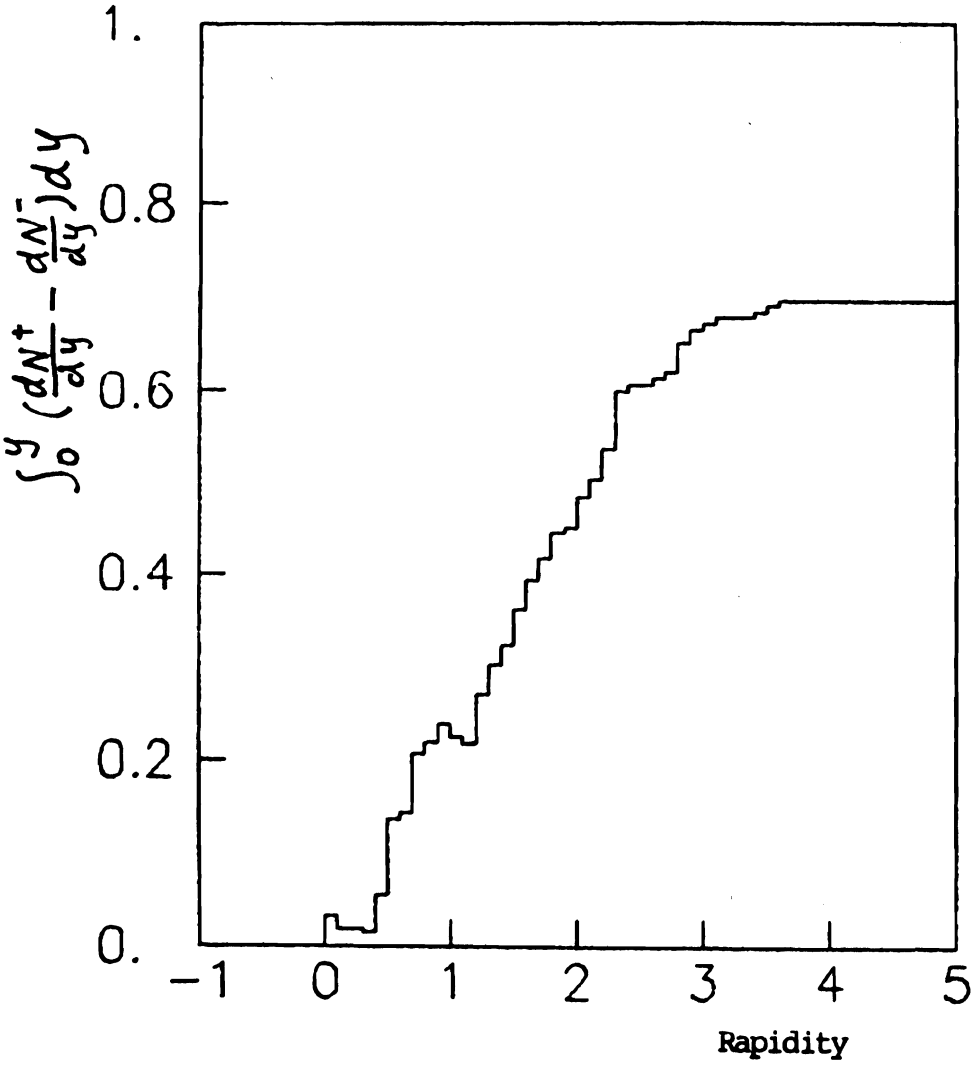

Figure 5.23

Rapidity distribution of integrated forward charge of J/psi in proton interactions

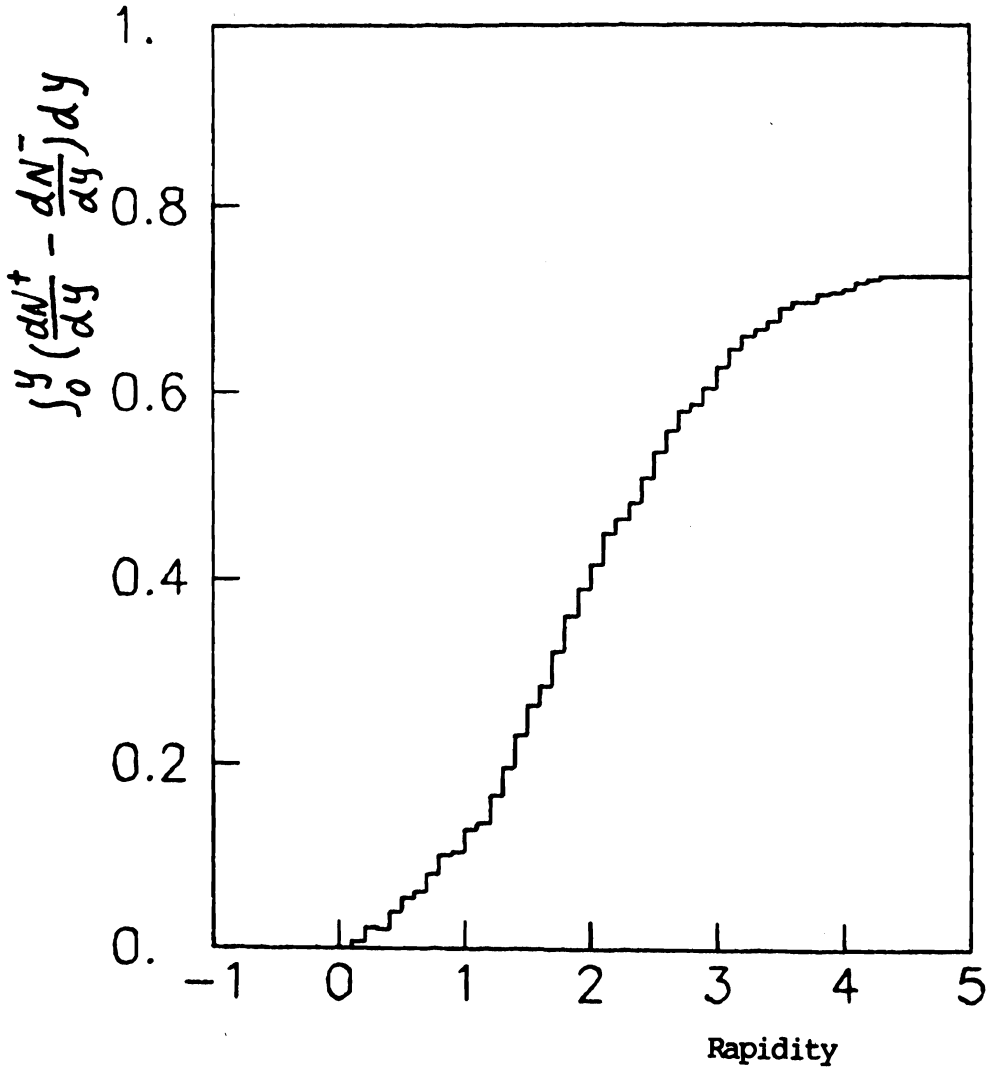

Figure 5.24

Rapidity distribution of integrated forward charge in inclusive interactions

interpretation of these results is that the J/psi production in pBe interactions is consistent with being produced by gluon fusion.

5.7 Discussion of the results

There are a lot things that could affect our results of forward charge study. Here I am going to discuss some of the effects qualitatively or quantitatively.

First of all, we consider the target effect. Because ours was a beryllium target, it was composed of 50% proton and 50% neutron. The forward charge was different in π^-n from that in π^-p interactions. In the π^-n inclusive interactions, the n fragmentation in the backward hemisphere would not dilute the charge in the forward hemisphere as in the π^-p interactions, this would increase the absolute value of the forward charge. On the other hand, the hadrons coming out of an interaction could have secondary interactions in the target, especially for the pions in the central rapidity region, their momenta were quite low in the lab system. This would reduce the absolute value of the forward charge. According to the curve in figure 2.7 (note that the data points in the curve had quite large errors too), the forward charge would be about -0.72 at our energy. Instead we found -0.654 for the forward charge in our inclusive interaction data. My explanation for this difference between -0.654 and -0.72 is that it is caused mostly by the target effect. In the case of pp interactions, because the forward backward symmetry the forward charge should be one; in the case of pn interactions, the forward charge would be diluted by the

leakage of the charge from forward hemisphere to backward hemisphere. So in the pBe interactions the forward charge would be less than one. Here the effect of secondary interactions in the target was more severe because there were more low-momentum particles in the central rapidity region. The target effect could partially account for the reason why the forward charge in pBe inclusive interactions was only 0.73 instead of one. Another effect making the forward charge small in pBe interactions was that the track finding efficiency used in the program was too high for pBe interactions, so the efficiency effect was under-corrected. The multiplicity was higher in pBe interactions than in π^-Be, the program was more difficult to find the tracks correctly in our pBe data.

An attempt was made to estimate the contributions from quark fusion and gluon fusion for J/psi and omega production using the forward charge as a function of Xf, in the assumption that the J/psi or omega were produced by simple quark fusion plus gluon fusion. At certain Xf, the forward charge could be expressed by the following formula.

$$F_c = \frac{\sigma_0 (F_{cq} \cdot \xi \cdot F_{q\bar{q}}(x_f) + F_{cg} \cdot F_{gg}(x_f))}{\sigma_0 (\xi \cdot F_{q\bar{q}}(x_f) + F_{gg}(x_f))} = \frac{F_{cq} \cdot \xi \cdot F_{q\bar{q}}(x_f) + F_{cg} \cdot F_{gg}(x_f)}{\xi \cdot F_{q\bar{q}}(x_f) + F_{gg}(x_f)} \quad (5.1)$$

Here F_{cq} or F_{cg} is forward charge in qq or gg fusion.

$\sigma_0 = 4\pi^2 G_{gg}/M^2$ is the elementary cross section of the process gg→A,

M is the mass of A.

$\xi = G_{q\bar{q}}/G_{gg}$

$$F_{q\bar{q}}(Xf) = \sum_{f=u,s,d} [Bq(x1) * Tq(x2) + Bq(x1) * Tq(x2)]/(x1+x2)$$

$F_{gg}(Xf) = [Bg(x1) * Tg(x2)] / (x1+x2)$

$x1, x2 = 0.5 * [\sqrt{Xf + 4M^2/s} +/- Xf]$

Bq and Bg are the structure functions of quarks and gluons in the beam particle.

Tq and Tg are the same as above but for the target particle.

We chose the structure functions for J/psi production as these used by NA3 group [ref. 14] for $Q^2 = M^2_{J/\psi}$. In the omega case, we chose the structure function used by ACCMOR group [ref. 44] for $Q^2 = M^2_{\phi}$. These structure functions are listed in Table 5.1. To have some idea how the structure function of the parton will affect the relative contributions from quark fusion and gluon fusion, we define a quantity called product structure function for each fusion process. In quark fusion, it equals $Bq(x1)Tq(x2) + Bq(x1) * Tq(x2)$. In gluon fusion, it equals $Bg(x1) * Tg(x2)$. In Figure 5.25 product structure functions are plotted as a function of Xf of J/psi. For quark fusion the $u\bar{u}$, $d\bar{d}$, $s\bar{s}$ and the total of these three are plotted separately. The $s\bar{s}$ curve is too low to be seen. The absolute scale is arbitrarily defined. The gluon product structure function is much bigger than that for quark fusion at low Xf region, but it falls faster than that for quark fusion as the Xf of J/psi increases.

We tried to get ζ, the ratio of effective coupling of quark fusion over gluon fusion to J/psi or omega production, by fitting the above formula to our forward charge as a function of Xf as in Figure 5.12 and 5.20. Here the Xf acceptance of our apparatus appears both in the

Table 5.1 parton structure functions

particle	parton	structure function	
		NA3	ACCMOR
pion	xu(x)=	0.52 x**0.4 (1-x)**0.78	0.55 x**0.4 (1-x)**0.9
valence	xd(x)		
pion	xS(x)	0.238 (1-x)**8.7	0.09 (1-x)**4.4
sea			
pion	xg(x)	1.66 (1-x)**2.38	2.0 (1-x)**3.0
proton	xu(x)	2.48 x**0.56 (1-x)**2.61	2.18 x**0.5 (1-x)**3.0
valence	xd(x)	1.43 x**0.56 (1-x)**3.61	1.23 x**0.5 (1-x)**4.0
proton	xS(x)	0.2 (1-x)**8.7	0.17 (1-x)**6.0
sea			
proton	xg(x)	3.22 (1-x)**5.16	2.5 (1-x)**4.0

a. the sea quark structure functions have su(3) symmetry

b. the sea quark structure functions are S(x)=u(x)=d(x)=2s(x)

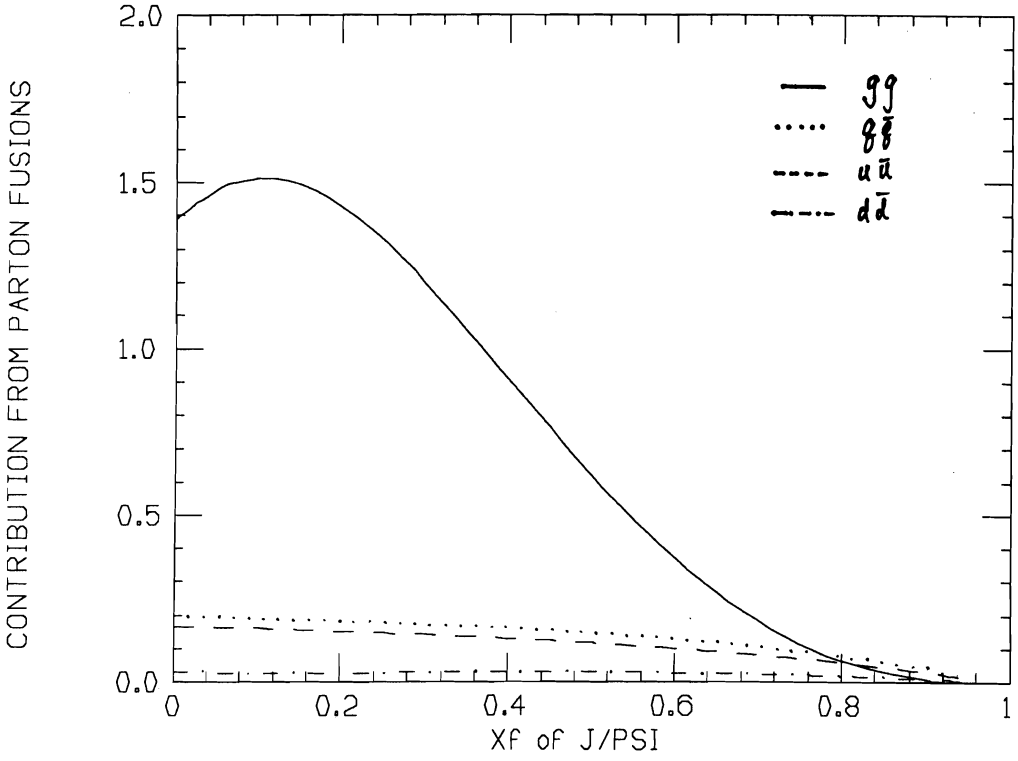

Figure 5.25
Product structure function as a function of Xf of J/psi
solid line gluon fusion; dotted line quark fusion;
dashed line up quark fusion;dot-dash line d quark fusion.
s quark fusion is too small to be seen.

numerator and denominator in equation 5.1, so the acceptance is not needed in the fit. A few assumptions were necessary before fitting.

First, the forward charge for gluon fusion and quark fusion was assumed to be -1.0 and -0.4 in π^-p interactions if the forward and backward fragmentations were separated from each other perfectly.

Second, the target effect was assumed to be proportional to the forward charge, this included the effect caused by the existence of neutrons in the target and the effect of second interactions.

Third, the dependence of forward charge on the effective energy was assumed to follow the one in Figure 2.7. Because the forward charge in our inclusive interactions was -0.654 instead of -0.72 in Figure 2.7, we scaled the curve in figure 2.7 by the ratio of -0.654/-0.72 to be used in the fitting.

In quark fusion, besides the main contribution from valence $\bar{u}$ quark in π^-, the d quark had smaller contribution. If d quark from π^- annihilated with $\bar{d}$ sea quark in proton, the forward $\bar{u}$ quark would fragment into hadrons whose average forward charge would be -0.6. In the following calculation, three values of forward charge r, -0.4, -0.45 and -0.5, were used for quark fusion in an ideal situation. Then the target effect and the effective energy dependences were scaled accordingly. By allowing the forward charge in quark fusion to vary, the uncertainty in assumptions one and two might be compensated. The third assumption could be the one that deviates from the physical

reality most. To really understand the energy dependence of forward charge in different processes, we need to know the dynamics of the fragmentation pretty well.

The fitting was done by plotting the chi-squared as a function of the parameter ζ. Three different forward charge values for quark fusion were used. Figure 5.26 is the plot of chi-squared as a function of ζ for J/psi. Figure 5.27 is a similar plot for omega. The minimum chi-squared is at different ζ for J/psi and omega. In J/psi case, the ζ is between 0.7 to 1.05 for different r values. In omega case, it is 0. Unfortunately the chi-squared is not very sensitive to the ζ. The uncertainty for ζ is big. The ζ value for minimum chi-squared varies when the ratio of -0.654/-0.72 changes. So this is not a best way to determine ζ. Very accurate data and better understanding of the fragmentation are needed to do so. Figure 5.28 plots the forward charge of J/psi production for five different ζ values. Because our poor statistics, it is hard to determine the value ζ. But from Figure 5.26 and 5.27 we could say that there is more gluon contribution in omega production than in J/psi production.

One point is worth mentioning here. D. W. Duke and M. J. Teper pointed out [ref. 45] that the Drell-Yan mechanism fails if the following relation is true.

$$M^2 \leq MIN\{x(S<\mu_\perp^2>^{1/2}, 100x\}$$

Here M is the mass of produced particle.

$\mu_\perp$ is the transverse mass of partons in the interaction,

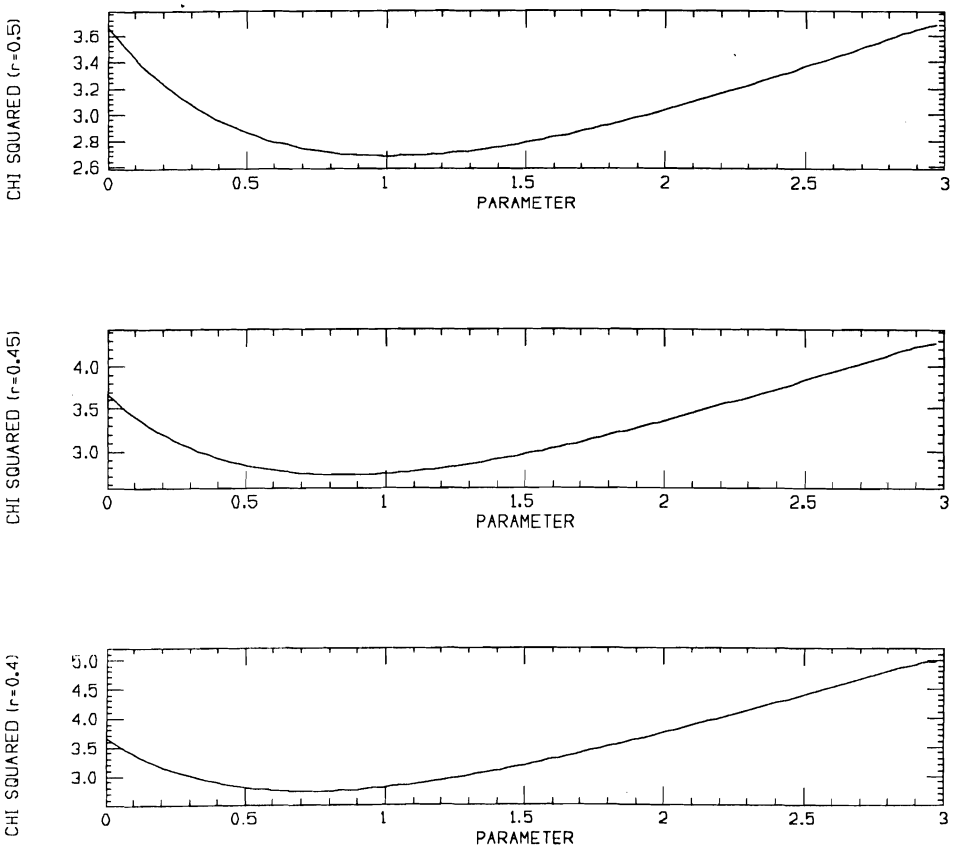

Figure 5.26
Chi-squared as a function of parameter for J/psi production the ratio of forward charges in quark fusion over gluon fusion (a) 0.4 (b) 0.45 (c) 0.5

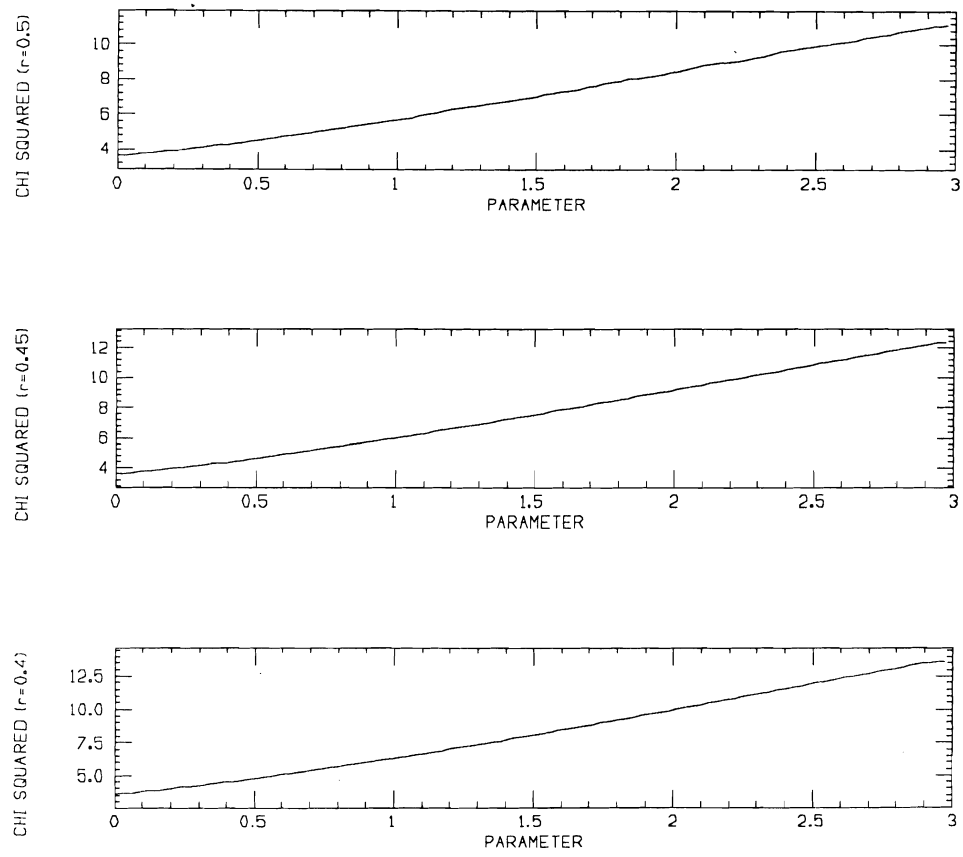

figure 5.27
Chi-squared as a function of parameter for omega production the ratio of forward charges in quark fusion over gluon fusion
(a) 0.4 (b) 0.45 (c) 0.5

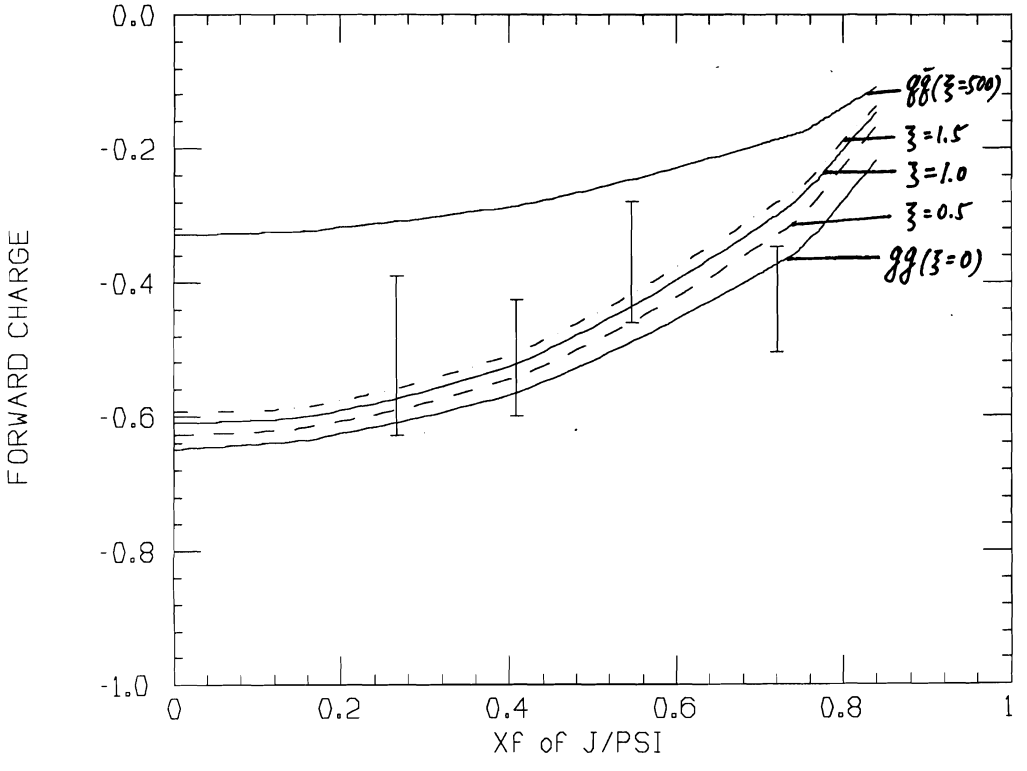

Figure 5.28
Forward charge as a function of Xf of J/psi assuming parameter
(a) ξ =0 (lowest solid line); (b) ξ =0.5 (dashed line);
(c) ξ =1.0 (middle solid line); (d) ξ =1.5 (dot-dashed line);
(e) ξ =500 (upper solid line) and the data points

it was chosen to be 1 GeV/c in reference 44.

From the above formula, for J/psi production this condition was satisfied above Xf=Ø.5. If a smaller value for parton transverse mass was chosen, the Drell-Yan mechanism should not fail at our energy for J/psi production. In our experiment the above condition was easily satisfied for omega production, the Drell-Yan mechanism should fail badly. According to D. W. Duke and M. J. Teper in reference 44, the omega should mostly be produced by fusion of two partons within the beam particle at our energy region. If their argument is correct, the above fitting for omega is not valid. The forward going hadron system will be the beam fragmentation most of the time.

5.8 Summary and conclusions

In this chapter, we have mainly discussed the resulting forward charge flow of the J/psi and omega productions in π^-N interactions. If we make the assumptions that in different processes the charge leakage through the y=Ø plane is proportional to the forward charge, and that for Drell-Yan production (d fragmentation) the forward charge is -Ø.4, then when we normalize the forward charge in inclusive π^-N interactions to be -1.Ø, the forward charge for J/psi and omega production is -Ø.71+/-Ø.Ø8 and -1.Ø1+/-Ø.Ø5 respectively. If the simple quark fusion plus gluon fusion model is true, very naively, the J/psi production is through quark fusion 48+/-14% of the time and the omega is through gluon fusion almost all of the time.

As the study showed, the dependence of the forward charge as a function of the effective energy must be included in the forward charge study. Because on the average the effective energy in omega events is larger than that in J/psi events, the difference between their average associated forward charge is less dramatic. The large difference which appeared in the energy independent analysis discussed in the first paragraph is partially due to a kinematical effect. This is evident when the data points for omega and J/psi production and the curve for inclusive interactions are put into the same plot of Figure 5.29. We can now see that the forward charge of omega production is consistent with that of inclusive interactions and that the forward charge of the J/psi production is somewhat less negative than those in the above two processes. The difference for most data points is one standard deviation. A certain fraction of the J/psi is produced through quark fusion, but not as large a fraction as appeared in the first paragraph. Much more data and better experimental design are needed to really assess the difference.

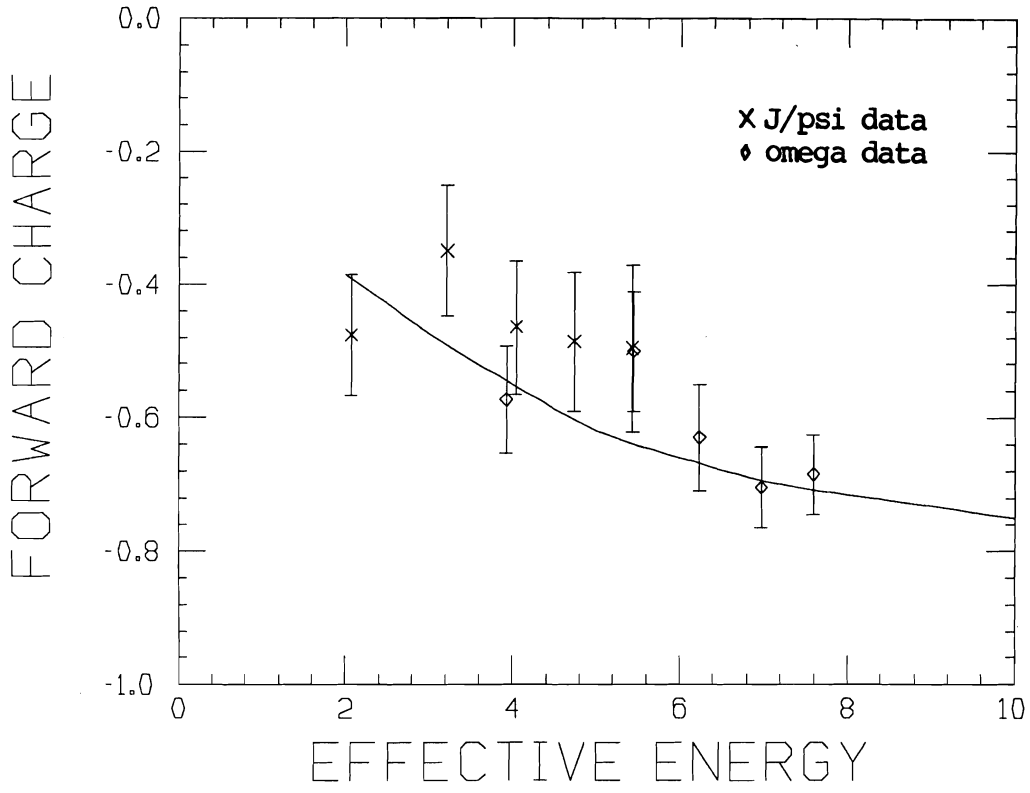

Figure 5.29

Forward charge as a function of effective energy

The curve is for inclusive interaction from Figure 2.7

APPENDIX A TRACK FINDING FOR CHARGED PARTICLES

This is the program used to find all tracks of charged particles, not just muon tracks. The muon trackfinding has been described in chapter 3. The beam trackfinding, vertex finding and upstream trackfinding are the same for both programs. This program was applied to the final J/psi sample only. For this relatively small sample, the consideration of saving computing time was not a big concern, a more complicated predicting scheme and trackfinding algorithm than muon trackfinding were developed.

1. Predicting scheme

In the analysis, we calculated the forward going charge using all tracks in the forward hemisphere in the CM (center of mass system). A pion at rest in the CM has a momentum of about 1.5 GeV/c in the lab. The program should be able to find the tracks with momenta down to 1.5 GeV/c.

The predicting scheme was based on swimming a lot of standard tracks through the magnetic field and getting the corresponding deviations of these tracks from straight lines at each plane. A very large number of tracks was needed to cover the whole acceptance range and to get the desired accuracy. Because the magnetic field was highly symmetric, the number of standard tracks needed could be reduced dramatically by the following reason: two tracks with same momentum but opposite charges and opposite upstream x, y slopes would have

trajectories symmetric to the z-axis, the deviations of these two tracks at each plane were the same except that they had opposite signs in both x and y directions; two tracks with same momentum, charge and upstream x slope but opposite upstream y slopes have trajectories which are mirror images to each other against the y=0 plane, the deviations of these two tracks at each plane in x direction were the same and the deviations in y direction had the same magnitude and opposite signs. For the above reasons, only the positively charged tracks with upstream y slope equal to or larger than zero were chosen as standard tracks. In the convention of this analysis, tracks bending towards the direction opposite to the x-axis were positively charged particles. With such considerations in mind that the position predictions of the tracks passing through the planes should be accurate to the level of wire spacing, about 0.2 cm, and that as less standard tracks as possible should be used, a following sets of momenta, upstream x slopes and upstream y slopes were chosen:

1/p=k, k=1, 2, 3,,, 50. p is the track momentum

slx=0.01, 0.04, 0.07, 0.1. slx is the upstream slope in the x view

sly=0., 0.03, 0.06. sly is the upstream slope in the y view

Every combination of each momentum, upstream x slope and upstream y slope values was used, the total number of standard tracks was 600. For each standard track, the deviations in x and y views at each plane from straight line were obtained by swimming the track through the magnetic field. The deviations of all these tracks were written to a file and were used in the track finding program.

The procedure of finding tracks is almost the same as muon trackfinding. After the upstream x and y tracks were found, they were matched to form pairs, this time only one hit was required among the first four tilted planes. The hits in four drift chambers and the hits in u and v planes of third, fourth and fifth UI chambers were used as seed points.

From a matched pair of upstream x and y tracks with x slope slxØ and y slope slyØ and a seed point in one of the planes, the x-view deviation xseedØ of the point from the straight line was calculated, the particle charge q of this track was determined by the value of this deviation. If the xseedØ was positive, the charge q was negative; if the xseedØ was negative, the charge q was positive. Because the predicting scheme was for positively charged particles with upstream y slopes larger or equal to zero, if the charge or upstream y slope of a track under consideration did not satisfy the above conditions, we made the predictions for a positively charged track with slx=slxØ*q, sly=|slyØ| and xseed=-|xseedØ|, then got the predictions for the origin track using the symmetry property mentioned above. For example, a matched x and y upstream tracks had x slope -Ø.44 and y slope -Ø.15, for one seed point the x-view deviation xseedØ was larger than Ø, then the particle charge of this track would be negative. In this case, first we made the predictions for a positively charged particle with slx=Ø.44, sly=Ø.15 and the xseed=-xseedØ, if the x-view and y-view deviations were dx and dy, the corresponding deviations for the origin track were -dx and -dy. Now the problem is how to get dx and dy.

For tracks that passed through enough planes to be hopefully found, the slx could have any value between -Ø.1 and Ø.1, the sly could have any value between -Ø.Ø8 to Ø.Ø8, the predictions for a particular pair of slx and sly values were made by extrapolating one parameter at a time. In the x view, for tracks of positively charged particles with upstream x slopes less than Ø.Ø1, the deviations at all the planes were not very big, the tracks with large momenta had small bending and the tracks with small momenta went out of the active areas of the planes early in its trajectory so the visible deviations are still small. If slx was less than Ø.Ø1, we used the standard tracks with slx = Ø.Ø1 to make predictions, if slx was between two fixed slx values that were used as x slopes of standard tracks, the deviations for this slx was derived by treating the deviations between these two fixed slx values as lying on a line draw through the two boundary points. We got the deviations at points A, B, C, D, E and F as shown in Figure A.1. In the y view, we had three standard sly values(Ø., Ø.Ø3, Ø.Ø6), we fit the deviations at these three points as a curve of second order polynomial and assumed that the deviations of the tracks with sly other than these three values were very close to the values determined by this curve. We got the deviations at points G and H in Figure A.1.

From the method mentioned above, the program searched the x-view deviations of the standard tracks with this pair of slx and sly values at the plane where the seed point came from, it could be found that the deviation of the seed point was between the deviations of two standard tracks, both had the same slx and sly and their momenta had the values

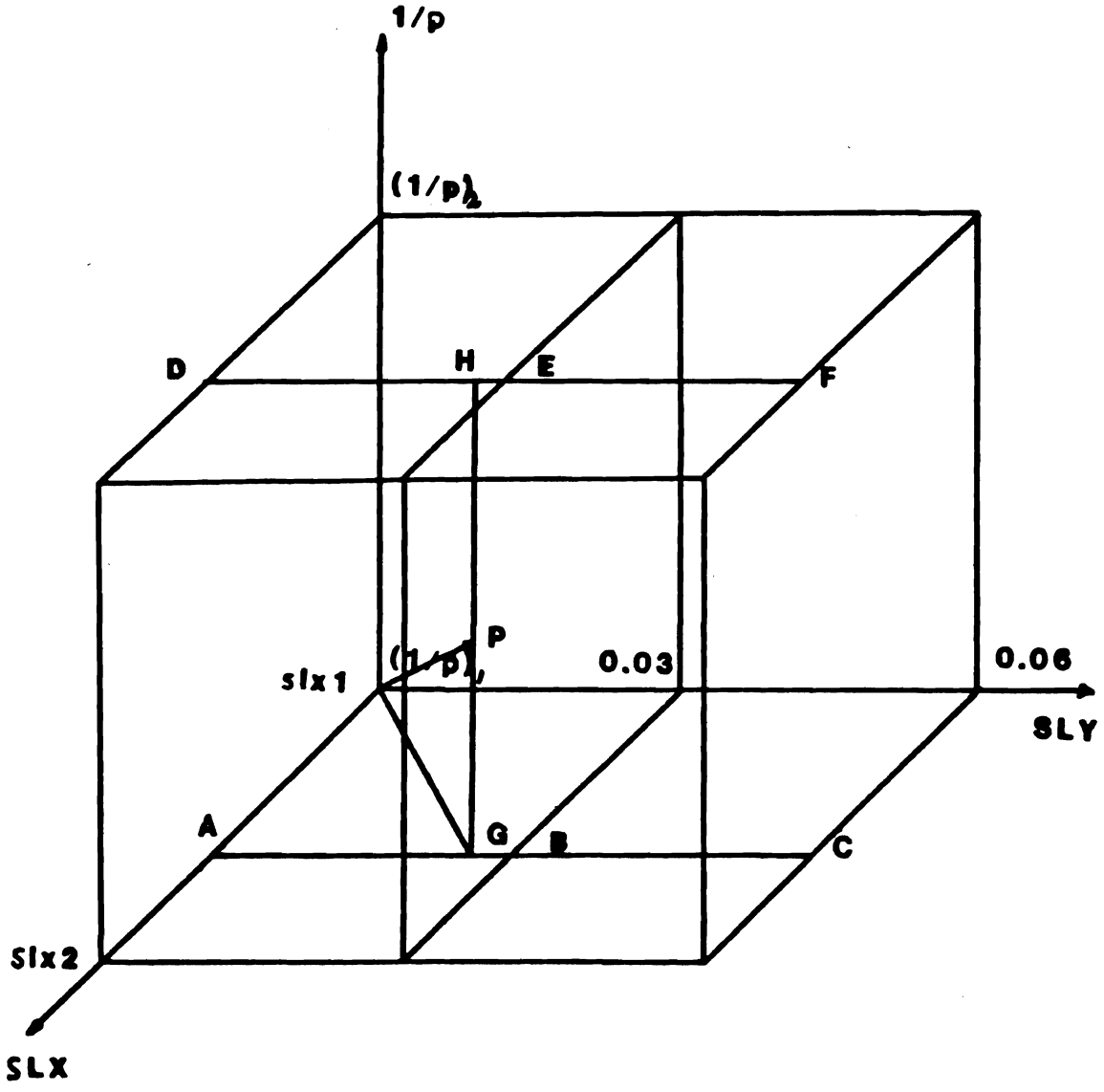

Figure A.1

Illustration of the extrapolation method

used for predicting tracks

of two neighboring standard tracks. The momentum of this track was determined by straight-line extrapolation from these two standard track momenta by knowing all the three deviation values.

After the momentum of the track was determined, the deviations of the track at all other planes were calculated by extrapolation method using the deviations of several standard tracks, the momenta, upstream x slopes and y slopes values of these tracks were closest neighbors to the corresponding parameters of the track under study in three dimension grid of momentum, upstream x slope and y slope.

Two tests were made to see how the predicting scheme worked. The first one was to compare the deviations of tracks at each plane derived by two different methods, one method got the deviations by swimming the tracks through the magnetic field, the other one got the deviations by using the predicting scheme. The track parameters used here were randomly chosen in certain ranges. The upstream x slopes of the tracks were between -Ø.1 to Ø.1, the upstream y slopes of the tracks were between -.Ø8 and Ø.Ø8 and the momenta of the tracks had the magnitudes between 1.5 GeV/c and 2ØØ GeV/c. Both charge signs of the tracks were tested. Most of the time the differences between these two deviations were very close to zero. A few percent of them were a little more than Ø.2 cm. This result was good enough for predicting tracks if the tracks in the real data followed the same paths as the ones when the tracks were swum through the magnetic field.

The second test was to histogram the differences of the real hit positions in each plane from the predicting ones for the real data, the entries to the histogram were chosen for the tracks with high quality, or these tracks, for which in more than 80 percent of the planes they passed a hit was found. The differences were somewhat larger than these in the first test, the typical sigma value was about 0.2 cm. From this a window of 0.6 cm was chosen to determine if a predicted hit was found or not in each plane for a track under study.

2. Trackfinding

Except for the predicting scheme described in part 1, the trackfinding program was not much different from the muon trackfinding described in chapter 3. For each upstream x track, all the upstream y tracks were tried to match it. Here one upstream x track and one upstream y track were matched when in at least one of the first four tilted planes a hit predicted from these two tracks was found. For the seed points, the program started from the most downstream plane (fourth drift chamber), each hit in this plane was tried as the seed point to predict a track trajectory. The hits in the plane upstream next to the above plane were used as seed points afterwards. The program worked all the way upstream till the u and v planes of the third UI chamber.

From a pair of matched x and y tracks and one seed point, an imaginary track was formed. By checking if this track went out of the plane bounds, we got the total number of planes through which the track passed. By searching through the planes for hits near the predicted

points in the planes, we got the total number of planes in which hits were found. The above two numbers were obtained from the planes from the first tilted 80 cm plane downstream to the plane having seed point in it. If the predicted track went out of half or more plane bounds, the program gave up to find it. The ratio of the second number over the first number was called the hit percentage of the track, if this ratio was equal or above 60%, this track was saved for later consideration.

It was possible that a lot of tracks would be saved from a single upstream x track by passing the requirements mentioned above. Most of these tracks were the same track but seeded from different planes. To make the weeding simpler later on, a preliminary weeding procedure was applied in this stage. From one upstream x track, these predicted tracks were considered as the same track if they shared one or more hit in drift chambers or two or more hits in u and v planes of the third, fourth and fifth UI chambers. We only saved the track that hit most planes among these tracks or the one that had least chi-squared if some of the tracks had same number of hit planes. The other tracks were omitted. If two predicted tracks from the same upstream x track did not meet the above conditions, they were possibly different tracks. The program limited the maximum number of saved tracks from the same upstream x track to be three. This was done by comparing the tracks from the same upstream x track and picking up the most qualified tracks. The comparison was as follows: Tracks which had most found hits were saved, if two tracks had same number of hits, the one which

had least chi-squared value was saved.

The tracks predicted from all the upstream x tracks were saved and were compared later to weed out the duplicated tracks and those bogus tracks that shared too many hits with the other tracks.

3. Weeding

By looking at the graphics displays of the events with the hits of the planes and the trajectories of the tracks saved so far, the trackfinding had found almost every track seen by the eye but there were some bogus tracks and duplicated tracks. To clear it up, the following weeding program was applied.

The program lined the tracks in the order of the number of hits found for each track and the chi-squared of each track, from the track with most number of hits to the track with least number of hits, and from minimum chi-squared to maximum chi-squared if the tracks had same number of hits. The first track was automatically accepted, from the second track on, every track was compared with the tracks already accepted before. If the track under study shared hits in u and v planes of UI third, fourth and fifth chambers with one of the accepted tracks, the shared hits were subtracted from the total number of hits of the track, if the new hit percentage of the track was less than 65%, this track was considered as a false track. Also the total number of shared hits with all the tracks having better qualities in all the chambers was subtracted from the total number of hits found, if the new

ratio of the number of hit planes over the number of passed planes was less than 60%, this track was not saved.

At last each track was compared with all other accepted tracks, if there were more than three hits not shared with other tracks in u and v planes of the third, fourth and fifth UI chambers and in the drift chambers, and if the hit percentage after subtracting the shared hits was more than 50%, this track was considered as a real track. This procedure was repeated twice because some tracks were changed from real track to false track or vise verse in the first iteration.

Two hundred events were examined graphically by eye in the process of developing the weeding program, all the cuts were finely tuned, the result was quite good in the sense that most of the tracks seen by eye were found and there were not many duplicated tracks and bogus tracks. The trackfinding efficiency was obtained by the monte carlo method discussed in Appendix B.

APPENDIX B TRACKFINDING EFFICIENCY

To calculate the average forward charge of the particles produced in J/psi events besides the two muons from J/psi decay, the result had to be corrected by the trackfinding efficiencies including the geometric acceptances. The efficiencies were found by using monte carlo method.

To cover the whole acceptance region of the apparatus, a two dimensional array of track momenta and incident angles was chosen. For each track with a momentum and an angle of chosen values, about 200 tracks were embedded into 200 events in the J/psi sample, one track in each event. The upstream parts of These 200 tracks were evenly distributed on a cone surface, the cone axis was on the beam line and the half angle of the cone was the angle chosen above. The track was swum through the equipment in the magnetic field and the predicted hit in each plane was embedded into the real hits of that plane, the chance of embedding the hit into the real data for each plane was determined randomly according to the efficiency of that plane (the method used to find the plane efficiencies will be described in Appendix D). In the MWPC planes, the position of the wire nearest to the predicted point was embedded into the data. For the drift chamber planes, the predicted position was converted to the drift time, and this time was digitized according to the resolution of drift time TDC. The H hodoscope elements were treated the same way, because of the high efficiencies of the H hodoscope, the element would be turned on almost

every time if a track passed through it. The embedded track was forced to pass the interaction vertex in the target, the vertex was found by the vertex finding program before the monte-carlo track was embedded.

Then the trackfinding program was applied to this monte carlo embedded data. The tracks found were compared with the embedded track, most of the time a track was found that its momentum and upstream slopes were very close to these of the embedded track. The differences between the upstream x and y slopes of the found tracks with these of embedded tracks were less than 0.001, the momentum differences were less than one percent. In these cases, we can certainly say that the monte carlo embedded tracks were found. But for some of the events, a track found had upstream x and y slopes very close to these of the embedded track, but the momentum was a few percent off. For the physics we are concerned with, the small differences of found momenta from the embedded momenta would not affect the forward charge calculation, so we made the requirement of finding the embedded track quite loose, the allowed difference of upstream x slopes or y slopes was 0.002, the allowed momentum difference was set at 10%.

The resulting trackfinding efficiencies are in the table at the end of this appendix, the statistical error and the systematic error were at the level of a few percent. We chose the grid size in the two dimension grid of momentum and incident angle such that the efficiency extrapolation for any found track of other momentum and angle values would have error less than the statistical and systematic errors.

It was checked that the efficiency of a positively charged track was the same as a negatively charged track with the same momentum magnitude and incident angle within the statistical error. This feature that the equipment was not biased to one charge than the other was also verified by histograming the muon momenta of the J/psi events according to the charge of the muons, the average of the muon momenta of both charges were very close to each other.

In the efficiency table, the drops of the efficiencies in the region of zero incident angle were due mostly to that the implanted upstream tracks were not found by the upstream trackfinding or the found track parameters were not accurate enough, because there were a lot of hits in this region; the drops of the efficiencies for the tracks with large incident angles and tracks with small momenta were due to the fact that these tracks went out of the plane bounds early so not many planes hits could be used to find these tracks.

To follow the convention, in Figure 4.2, the efficiency was converted to as a function of the rapidity of a track in the CM and its transverse momentum.

TABLE TRACKFINDING EFFICIENCIES

momentum (Gev)	100	50	20	10	5	3.33	2.5	2	1.67	1.43
angle (radian)	efficiencies (%)									
0.	92.0	93.0	95.0	95.6	94.5	87.5	73.6	59.0	53.0	56.2
0.015	92.5	93.2	95.7	95.8	94.5	89.0	78.0	70.0	67.0	72.0
0.0225	92.7	93.3	96.0	95.9	94.5	89.5	82.0	75.5	73.0	65.0
0.03	93.0	93.5	96.5	96.0	94.5	90.0	86.0	82.0	79.0	61.0
0.0375	94.0	94.5	97.0	96.0	94.3	92.0	90.5	84.0	73.0	58.0
0.045	95.0	96.0	97.5	96.0	94.3	92.5	91.0	77.0	68.0	55.5
0.0525	96.0	96.5	96.5	96.0	94.0	92.5	88.5	73.0	67.0	56.0
0.06	97.0	97.0	96.0	95.5	94.0	93.0	83.0	70.0	66.0	56.0
0.0675	96.0	96.0	95.0	95.0	92.0	86.0	79.0	68.0	65.0	57.0
0.075	88.0	94.0	93.5	93.0	88.0	82.0	75.5	67.0	64.0	58.0
0.0825	82.0	88.0	89.0	89.0	83.0	77.0	72.5	65.5	63.0	57.5
0.09	73.0	83.0	84.0	85.0	76.0	72.0	69.0	64.0	62.0	56.8

APPENDIX C TRACK FITTING

For high mass dimuon events, in order to narrow down the width of J/psi signal, the track parameters of the muon particles had to be adjusted by fitting the tracks using the hits associated with them. The five track parameters are the upstream x and y slopes, the intercepts of these upstream tracks at z=Ø and the track momentum.

The fitting started by swimming the track with the parameters found in the muon trackfinding program through the equipment. The exact location of the swum track at each plane was compared with the associated hit of the track at that plane, if one plane did not have a hit associated with that track, that plane was not used in the fitting. For the simplicity of the language, we define several terms as below:

Zi's are the z positions of the planes;

SLX and SLY are slopes of upstream x and y tracks;

XINT and YINT are intercepts of upstream x and y tracks at z=Ø;

PRE = 1/P with the charge sign in it, P is the momentum of the track;

PST is the momentum of a standard track;

UXi's and UYi's are cosin's and sin's of plane angles;

i's are relative weights of the planes;

DSTi are deviations from straight line at each plane by swimming a 15 GeV standard track of zero incident angle through the magnetic field.

The fitting was actually to minimize the chi-squared defined in the following formula:

$$\chi^2=\sum_i[(UPi-UHi)^2/\sigma i^2]$$

UPi=USX*UXi+USY*UYi

USX=Fix(SLX,XINT,SLY,YINT,P)

USY=Fiy(SLX,XINT,SLY,YINT,P)

The expansions of these two term were:

USX=XINT+SLX*Zi+DSTi*PST/P+DXi(SLX,SLY,P)

USY=YINT+SLY*Zi+DYi(SLX,SLY,P)

Here DXi and DYi were second order terms, they could be neglected when we made differentiations of $\delta\chi^2/\delta$SLX, $\delta\chi^2/\delta$XINT and so on. By differentiating χ^2 to SLX, XINT, SLY, YINT and PRE, we get five equations:

$$\frac{1}{2}\delta\chi^2/\delta SLX=\sum_i(UPi-UHi)*\delta UPi/\delta SLX/\sigma i^2=\sum_i UXi*Zi*(UPi-UHi)/\sigma i^2=0$$

$$\frac{1}{2}\delta\chi^2/\delta XINT=\sum_i(UPi-UHi)*\delta UPi/\delta XINT/\sigma i^2=\sum_i UXi*(UPi-UHi)/\sigma i^2=0$$

$$\frac{1}{2}\delta\chi^2/\delta SLY=\sum_i(UPi-UHi)*\delta UPi/\delta SLY/\sigma i^2=\sum_i UYi*Zi*(UPi-UHi)/\sigma i^2=0$$

$$\frac{1}{2}\delta\chi^2/\delta YINT=\sum_i(UPi-UHi)*\delta UPi/\delta YINT/\sigma i^2=\sum_i UYi*(UPi-UHi)/\sigma i^2=0$$

$$\frac{1}{2}\delta\chi^2/\delta PRE=\sum_i(UPi-UHi)*\delta UPi/\delta PRE/\sigma i^2=\sum_i UXi(UPi-UHi)*DSTi*PST/\sigma i^2=0$$

and

UPi-UHi=UPio-UHi+UXi(DXINT+Zi*DSLX+DSTI*PST*DPRE)+UYi*(DYINT+Zi*DSLY)

Here UPio-UHi is the zero order deviation and UPio is the predicted point by swimming the track (SLX, XINT ,SLY, YINT, P) through the magnetic field. from the above five equations we could obtain five unknown values of DSLX, DXINT, DSLY, DYINT, DPRE by solving matrix

equations.

The five new track parameters were SLX+DSLX, SLY=SLY+DSLY and so on. Compared with the previous track parameters, these values were closer to the final ones. In the second iteration, the procedure was similar but the track with the new parameters was swum through the equipment. This time the program searched the hits near the places where the swum track went through. In some planes, new hits were found, increasing the number of hits associated with the track; in some planes, the hits originally associated with the track were too far from the new track trajectory that they were no longer regarded as belonging to this track. But most of the hits were not changed. Using this new set of hits, another five new track parameters were calculated using the same procedure as in the first iteration. The resulting track parameters after the second iteration were quite close to these after first iteration, no more iteration was executed. As mentioned in chapter 4, after fitting the muon tracks, several cuts were applied to the data. One cut was to tighten the windows around M and N counters, another cut was that more than 70% of the predicted hits in the related chambers should be found for each track. These cuts were determined by the consideration to keep the balance between obtaining the best signal to background ratio and getting the most number of J/psi events.

Another fitting was done for J/psi events in searching for the chi signal. In obtaining the chi states, we treated the dimuon pair with its invariant mass between 3.05 GeV and 3.15 GeV as J/psi. When the

J/psi was combined with each gamma found in the same event, the dimuon mass was forced to be the exact mass of J/psi (3.Ø97 GeV). This was done by constraint-fitting the track parameters of the two muons, the two constraints were that the invariant dimuon mass of the J/psi events was fixed at 3.Ø97 GeV and these two muon tracks came from the same vertex. The ten parameters of two muon tracks were adjusted to make the chi-squared minimum. The procedure was similar to that in the muon track fitting. Ten equations were obtained by differentiating the chi-squared to each track parameter, these equations and the two constraint equations were used in the matrix conversion to get the first order corrections for these parameters. Because the chi-squared was not the linear function of some of the track parameters, the approximation of first order expansion of Taylor series was used. After the first iteration of the fitting, the dimuon mass of the new muon tracks was very close to the 3.Ø97 GeV value, most of them were within 1 MeV, the maximum deviation was about 6 MeV. This result was good enough for chi physics.

APPENDIX D MWPC AND DRIFT CHAMBER EFFICIENCIES

In order to know how well the MWPC and drift chambers performed during the experiment, we derived the efficiencies for the MWPC and drift chambers. These efficiencies were used in the monte carlo program to calculate the trackfinding efficiency described in Appendix B.

Basically we used high quality tracks to derive the efficiencies of these chambers. For MWPC planes, we found these tracks by seeding in drift chamber three, a good track was found if drift chamber one, two and three and more than five of ten u v planes of UI chambers had hits in them within cuts (0.6 cm). The tracks should have chi-squared less than some limit. A subset of tracks were used in determining the efficiency for each plane. The tracks used for determining the efficiency for one u or v plane of UI chambers were those that had hits in more than five planes among other nine u and v UI chamber planes; the tracks used for determining the efficiency for one x-measuring plane of 80 cm chambers were those that had hits in all three other x-measuring 80 cm planes; the tracks used for determining the efficiency for one y-measuring plane were those that had hits in more than 4 planes among other 7 y-measuring planes. The efficiency for each plane was the percentage of these tracks that had hits in this plane too.

Some hits found in the plane under study were belonging to other tracks but accidently fell into the window around the predicted point, this made the found efficiency higher than it should be. To correct this background effect, the program looked for hits 2 cm away from the predicted point, the total window width for both sides was the same as the window around the predicted point. The real efficiency was obtained by subtracting from the efficiency derived in the last paragraph the rate of finding such hits. The correction was at one percent level. The program was applied to several different kinds of data, one was the low intensity interaction data, another one was the electron calibration data and the third one was the dimuon data. The efficiencies of the planes were lower in dimuon data than in the other two, I thought this was due to the intensity effect, the chamber efficiencies droped as the beam intensity went up.

In studying the drift chamber efficiencies, the good tracks were found by seeding in one drift chamber which was not under current study and requiring that all tilted planes of UI chambers had hits in them. The drift chamber efficiency was the percentage of the time that these tracks had a hit in this drift chamber also. We first got the anode (or x view) efficiencies, and looked for delay line efficiencies when the anode signal was found for the track in the x view. A y hit was found if it was within the window of the predicted hit, the windows in x and y views were 0.6 cm and 7.5 cm respectively.

REFERENCES

1. D. A. Bauer et al., Phys. Rev. Lett. 54 753(1985)

2. S. N. Gupta et al., Phys. Rev. D26, 3305(1982)

3. W. Buchmuller, Preprint CERN-TH 3938(1984)

4. M.Bander and D. Silverman, Phys. Lett. 134B, 258(1984)

5. S. D. Drell and T. M. Yan, Annals of Physics 66, 578(1971)

6. D. Sivers, Nucl. Phys. B106 95(1976)

7. K. J. Anderson et al, Phys. Rev. D21 3075(1980)

8. M. Binkley et al., Phys. Rev. Lett. 37, 578(1976)

9. S. Zaninotte et al., Proc. 15th Conf. Moriond (1980)

10. I. R. Kenyon, Rep. Prog. Phys. 45, 1261(1982)

11. W. Aithenhead et al., Phys. Rev. Lett. 45 157(1980)

12. K. W. Lai and R. L. Thews, Phys. Rev. Lett. 44, 1731(1980)

13. T. Weiler, Phys. Rev. Lett. 44, 304(1980)

14. J. Badier et al., Z. Phys. C20 101(1983)

15. H. Abramowicz et al., Z Phys. C12, 289(1982)

16. J. N. Phillips, Proc. 20th int. Conf. Madison, 1470(1980)

17. C. E. Carlson and R. Suaya, Phys. Rev. D14 3115(1976)

18. C. E. Carlson and R. Suaya, Phys. Rev. D15 1416(1977)

19. C. E. Carlson and R. Suaya, Phys. Rev. D18 760(1978)

20. L. M. Jones and H. W. Wyld, Phys. Rev. D17 1782(1978)

21. M. Gluck, J. F. Owens and E. Reya, Phys. Rev. D17 2324(1978)

22. J. H. Kuhn, Phys. Lett. 113B 509(1980)

23. F. Halzen, Proc. 21th Int. Conf. Paris, J. de Phys. c3-381(1982)

24. R. Baier and R. Ruckl, Phys. Lett. 102B, 364(1981)

25. L. Clavelli et al., Phys. Rev. D29, 57(1984)

26. L. Clavelli et al., Preprint IUHET 93(Indiana University)

27. Y. Lemoigne et al., Phys. Lett. 113B 509(1982)

28. S. R. Hahn et al., Phys. Rev. D30 671(1984)

29 B. Pietrzyk et al., Phys. Lett. 113B 105(1982)

30. H. S. Budd et al., Phys. Rev. D31 1132(1985)

31. M. Faessler, Ann. Phys. 137 44(1981)

32. P. Soding, Preprint DESY 83-104

33. S. Barlag et al., Z Phys. C11 283(1982)

34. E. A. De Wolf, Z. Phys. C22 87(1984)

35. R. Gottgens et al., Z. Phys. c9 17(1981)

36. M. Basile et al., Preprint CERN-EP/84-94

37. K. Fialkowski, Preprint TPJU-2/84

38. P. Lukens, thesis, University of Illinois, 1984

39. H. Budd, thesis, University of Illinois, 1983

39. R. Hicks, thesis, University of Illinois, 1978

40. H. Budd, thesis, University of Illinois, 1983

41. T. Graff, thesis, University of Illinois, 1984

42. V. V. Anisovich et al., Sov. J. Nucl. Phys. 38(2) 254(1983)

43. J. Bellinger, thesis, University of Illinois, 1985.

44. C. Daum et al., Nucl. Phys. B186 205(1981)

45. D. W. Duke and M. J. Teper, Nucl. Phys. B166 84(1980)

VITA

Weiguo Li [redacted]. He graduated from China's University of Science and Technology in 1968. He was a worker in an oxygen gas factory in the Northeast of China in the following years. In 1973 he went back to the University to be a teaching assistant until 1978. He came to the United States in 1979, since then he has been a graduate student in the Physics Department at the University of Illinois at Urbana-Champaign. He was a research assistant from 1980 to 1985.